Universität Stuttgart

Institut für Wasser- und Umweltsystemmodellierung

Mitteilungen

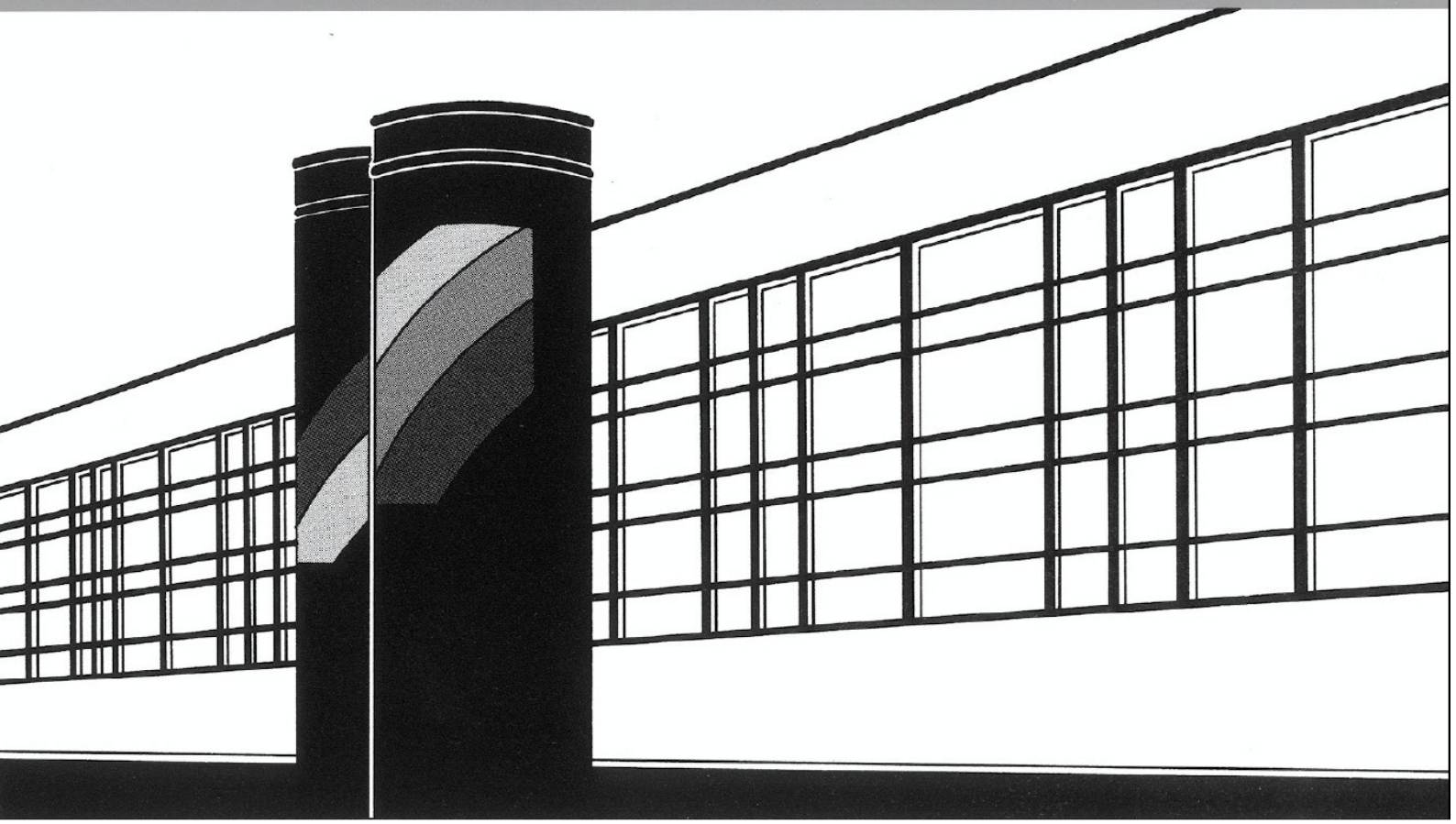

Heft 284 Beatrix Becker

Development of efficient multiscale multiphysics models accounting for reversible flow at various subsurface energy storage sites

Efficient multiscale multiphysics models accounting for reversible flow at various subsurface energy storage sites

von der Fakultät Bau- und Umweltingenieurwissenschaften der
Universität Stuttgart und dem Stuttgart Center for Simulation Science
zur Erlangung der Würde einer Doktor-Ingenieurin (Dr.-Ing.)
genehmigte Abhandlung

vorgelegt von

Beatrix Becker
aus Stuttgart, Deutschland

Hauptberichter:	Prof. Dr.-Ing. Rainer Helmig
Mitberichter:	apl. Prof. Dr. rer. nat. Bernd Flemisch
	Prof. Dr. rer. nat. Christian Rohde
	Prof. Michael A. Celia, Ph.D.

Tag der mündlichen Prüfung: 22.06.2021

Institut für Wasser- und Umweltsystemmodellierung
der Universität Stuttgart
2021

Heft 284

Efficient multiscale multiphysics models accounting for reversible flow at various subsurface energy storage sites

von
Dr.-Ing.
Beatrix Becker

Eigenverlag des Instituts für Wasser- und Umweltsystemmodellierung
der Universität Stuttgart

D93 Efficient multiscale multiphysics models accounting for reversible flow at various subsurface energy storage sites

Bibliografische Information der Deutschen Nationalbibliothek
Die Deutsche Nationalbibliothek verzeichnet diese Publikation in der Deutschen Nationalbibliografie; detaillierte bibliografische Daten sind im Internet über http://www.d-nb.de abrufbar

Becker, Beatrix:
Efficient multiscale multiphysics models accounting for reversible flow at various subsurface energy storage sites, Universität Stuttgart. - Stuttgart: Institut für Wasser- und Umweltsystemmodellierung, 2021

(Mitteilungen Institut für Wasser- und Umweltsystemmodellierung, Universität Stuttgart: H. 284)
Zugl.: Stuttgart, Univ., Diss., 2021
ISBN 978-3-942036-88-7

NE: Institut für Wasser- und Umweltsystemmodellierung <Stuttgart>: Mitteilungen

Gegen Vervielfältigung und Übersetzung bestehen keine Einwände, es wird lediglich um Quellenangabe gebeten.

Herausgegeben 2021 vom Eigenverlag des Instituts für Wasser- und Umweltsystem-modellierung

Druck: DCC Kästl e.K., Ostfildern

Danksagung

Diese Arbeit wurde gefördert durch ein Promotionsstipendium der Landesgraduiertenförderung. Ich danke dem Ministerium für Wissenschaft, Forschung und Kunst Baden-Württemberg für die großzügige finanzielle Unterstützung, die langfristig fokussiertes Arbeiten möglich gemacht hat. Teile der Arbeit entstanden während eines Forschungsaufenthalts in Princeton, USA. Ich danke dem Stuttgart Center for Simulation Science sowie dem Deutschen Akademischen Austauschdienst (DAAD) für die finanzielle Unterstützung dieses Forschungsaufenthalts und der bis heute andauernden Kooperation.

Diese Arbeit wäre nicht entstanden ohne die Unterstützung vieler großartiger Menschen, die mich auf diesem Weg am Lehrstuhl begleitet haben. Im Besonderen möchte ich Rainer Helmig danken, der mich schon während meines Bachelor-Studiums für die Fluidmechanik zu begeistern wusste. Seine weise Voraussicht und sein unermüdliches Engagement haben diese Arbeit ins Leben gerufen und mir den Weg geebnet, der mich unter Anderem bis an eine der Wirkungsstätten Albert Einsteins führte. Weiterhin möchte ich Bernd Flemisch danken, für kluge Korrekturen, zahlreiche Lehrstunden umd seine unentbehrliche Hilfe im Kampf mit C++. Ich danke Holger Class für anregende fachliche Diskussionen und die Möglichkeit, zunächst als studentische Tutorin und später als Doktorandin Lehre mit ihm machen zu dürfen. Christian Rohde danke ich für seinen Mitbericht und eine spannende, lehrreiche Zeit im Management der Graduiertenschule des SFB 1313. Allen meinen Kollegen am Lehrstuhl für Hydromechanik und Hydrosystemmodellierung danke ich für jeden Moment der willkommenen Ablenkung, für emotionale Diskussionen fachlicher und außerfachlicher Natur, und das Wissen, sich auf jeden Einzelnen verlassen zu können. Besonderer Dank geht an meinen langjährigen Schreibtischnachbarn Johannes Hommel, der dafür sorgt, dass unserem gemeinsamen Büro ein Hauch Wildnis anhaftet und der mir ein Vorbild ist in effizienter Arbeitsweise und Zielstrebigkeit. Mein unendlicher Dank gebürt David Werner und Michelle Hartnick, für ihre verlässliche Hilfe bei technischen Fragen wirklich jeder Natur, sowie Stefanie Siegert, Beate Spinner, Prudence Lawday und Maria Costa Jornet, die mit großem Einsatz und Verstand den Lehrstuhl zusammenhalten.

This work has strong ties to several people beyond the University of Stuttgart. I want to thank Mike Celia, for graciously inviting me to Princeton University and warmly

welcoming me into his group. Thank you for many fruitful discussions and the possibility to participate in your oustanding lecture. Thanks goes to Karl Bandilla, for his valuable advice and comments on our work. Last but not least a huge thanks to Bo Guo, who helped shaping this project and whose wise feedback and natural curiosity fueled this work from the very beginning.

Zu guter Letzt möchte ich meinen Freunden und meiner Familie danken, insbesondere meinen Eltern und meinem Mann, Steffen Becker, die mich durch die Höhen und Tiefen dieser Arbeit begleitet haben und mir an vielen Tagen den Rücken frei gehalten haben. Vielen Dank, dass ihr an mich glaubt und für eure Liebe.

Contents

List of Figures **V**

List of Tables **IX**

Nomenclature **XI**

Abstract **XVII**

Zusammenfassung **XIX**

1 Introduction **1**

1.1 Motivation 1

1.2 Energy storage in the subsurface 3

1.3 Modeling challenges 4

1.4 Structure of the thesis 7

2 Fundamentals **9**

2.1 Macroscopic considerations 9

2.1.1 Porosity and saturation 10

2.1.2 Wetting and non-wetting phases 11

2.1.3 Capillary pressure and residual saturation 12

2.1.4 Intrinsic permeability and relative permeability 13

2.2 Darcy's law and balance equations 14

2.2.1 Darcy's law for multiphase flow 14

2.2.2 Immiscible two-phase flow 15

2.2.3 Compositional two-phase flow 16

3 Pseudo-vertical equilibrium model **19**
3.1 VE models . . . 20
3.1.1 Governing equations of immiscible VE model . . . 21
3.1.2 Reconstruction . . . 23
3.2 Pseudo-vertical equilibrium and multiscale framework . . . 27
3.3 Pseudo-VE model . . . 30
3.3.1 Algorithm . . . 31
3.3.2 Update of pseudo-residual saturation . . . 32
3.3.3 Global and local pseudo-VE model . . . 34
3.4 Results and discussion . . . 36
3.4.1 Comparison of horizontal plume extent at $\mathbf{t} = \mathbf{10t}_{\text{seg}}$ . . . 39
3.4.2 Comparison of horizontal plume extent at $\mathbf{t} < \mathbf{10t}_{\text{seg}}$ . . . 42
3.4.3 Comparison of gas phase distribution . . . 44
3.5 Conclusion . . . 46

4 Multiphysics model for immiscible two-phase flow **49**
4.1 Multiphysics models . . . 50
4.2 Coupling strategy . . . 52
4.2.1 Fluxes across subdomain boundaries . . . 52
4.2.2 Computational algorithm . . . 54
4.3 Adaptivity . . . 55
4.3.1 VE criteria . . . 55
4.3.2 Local VE criteria . . . 56
4.3.3 Criteria analysis . . . 58
4.3.4 Adaptive algorithm . . . 61
4.4 Results and discussion . . . 62
4.4.1 Comparison between models . . . 64
4.4.2 Choice of threshold value for adaptive coupling . . . 68
4.5 Conclusion . . . 71

5 Multiphysics model for compositional two-phase flow **73**
5.1 Compositional full multidimensional model . . . 74
5.1.1 Sequential solution algorithm . . . 75
5.1.2 Transport estimate . . . 76
5.1.3 Flash calculations . . . 76

5.1.4 Discretization in space . . . 78
5.1.5 Advective flux calculation . . . 80
5.2 Compositional VE model . . . 81
5.2.1 States of compositional VE . . . 82
5.2.2 Model assumptions . . . 85
5.2.3 Governing equations . . . 87
5.2.4 Discretization in space . . . 90
5.2.5 Advective flux calculation . . . 91
5.2.6 Volume mismatch . . . 92
5.2.7 Reconstruction . . . 93
5.3 Coupling strategy . . . 99
5.3.1 Volume change due to fluxes across subdomain boundaries . . 100
5.3.2 Computational algorithm . . . 101
5.4 Adaptivity . . . 102
5.4.1 Local VE criteria . . . 103
5.4.2 Criteria analysis . . . 105
5.4.3 Adaptive algorithm . . . 108
5.5 Results and discussion . . . 109
5.5.1 Gas injection into a horizontal layer . . . 110
5.5.2 Gas storage in an idealized underground aquifer . . . 112
5.6 Conclusion . . . 117

6 Summary and Outlook **119**
6.1 Summary . . . 119
6.2 Outlook . . . 121

A Appendix **123**
A.1 Determination of fugacity coefficients . . . 123
A.2 Derivation of Rachford-Rice equation . . . 124

Bibliography **127**

List of Figures

1.1 Global anthropogenic CO_2 emissions from forestry and other land use as well as from burning of fossil fuel, cement production and flaring. . . 2

2.1 Averaging process from pore scale to REV scale 10

3.1 Coarse-scale saturation and fine-scale saturation in the vertically integrated framework. 21
3.2 Reconstruction of the fine-scale solution in the vertical direction based on the computed coarse-scale solution. 24
3.3 Relative permeability as a function of brine phase saturation. 28
3.4 Gas injection into a brine-filled confined aquifer with a relative permeability function with large exponent. 29
3.5 IMPES algorithm for the pseudo-VE model solving incompressible isothermal multiphase flow. Adapted from Becker et al. [2017] with permission from John Wiley & Sons, copyright 2017. 32
3.6 Sequence of calculation of the pseudo-residual brine phase saturation. 36
3.7 Horizontal plume extent for global pseudo-VE model, local pseudo-VE model and conventional VE model over horizontal plume extent for full multidimensional reference. 40
3.8 L2-norm for VE models for all test cases. 42
3.9 Relative error over dimensionless simulation time for global pseudo-VE model, local pseudo-VE model and conventional VE model. 43
3.10 Gas phase distribution for 2D reference, global pseudo-VE model, local pseudo-VE model and conventional VE model for case 1. 47
3.11 Gas phase distribution for 2D reference, global pseudo-VE model, local pseudo-VE model and conventional VE model for case 5 48

4.1 Schematic of the computational grid with subcells (dotted lines) at the interface between two subdomains. 53
4.2 Vertical profiles in one column. 57
4.3 Criterion values for the VE criteria based on saturation and relative permeability, respectively. 59
4.4 Buffer zone between full multidimensional subdomain and VE subdomain 63
4.5 A test of gas injection for the adaptive model. 63
4.6 Gas phase distribution for the adaptive multiphysics model with a threshold value of 0.03 and for the full multidimensional solution calculated on a two-dimensional grid for a series of simulation times after injection. 65
4.7 Gas phase distribution for the adaptive multiphysics model with a threshold value of 0.03, full multidimensional solution calculated on a two-dimensional grid and full VE model. 66
4.8 Number of computational cells in the domain over simulated time for full VE model, adaptive multiphysics model (with different threshold values ϵ) and full multidimensional model. Reprinted from Becker et al. [2018] with permission from John Wiley & Sons, copyright 2018. 68
4.9 Vertically averaged brine phase saturation over horizontal distance from injection location at $t = 192$ h for full VE model, adaptive multiphysics model (with different threshold values ϵ) and full multidimensional model. Reprinted from Becker et al. [2018] with permission from John Wiley & Sons, copyright 2018. 69
4.10 L2-norm error of brine phase saturation for full multidimensional model, adaptive multiphysics model and full VE model. 71

5.1 Algorithm for the sequential compositional flow model. 75
5.2 Three different model concepts for compositional VE with increasing complexity 85
5.3 Assumed vertical profiles of brine phase saturation, phase pressures, mass fractions of the water component, and phase densities. 88
5.4 Vertical profiles in one column. 104
5.5 Criterion values for the VE criteria based on saturation and relative permeability, respectively. 106
5.6 Criterion values for the VE criteria based on saturation and relative permeability, respectively. 108

5.7 Gas phase distribution for the full VE model, the adaptive multiphysics model with a threshold value of 0.03, and full multidimensional model. 110
5.8 Absolute and relative (to total mass of gas components) mass of dissolved gas components in entire domain over simulated time 111
5.9 Initial gas phase distribution in an idealized underground aquifer. . . 112
5.10 Injection rate, total mass of injected gas and bottom hole pressure for a full multidimensional simulation. We inject hydrogen into a radial symmetric anticline structure, previously filled with hydrogen and brine at equilibrium. 114
5.11 Total concentration of gas components after the last injection during injection-only phase (after 9 simulated months) and after the last extraction during operation phase (after 45 simulated months). 115
5.12 Gas phase pressure, mass fraction of water components in the gas phase, gas phase saturation, and total mass of dissolved gas components in the domain. 116

List of Tables

3.1 Parameter combinations considered in the simulations. 38

4.1 Relative average number of cells (compared to the full multidimensional model) and relative CPU times for full VE model, adaptive multiphysics model (with different threshold values ϵ) and full multidimensional model. 67

Nomenclature

Selected Acronyms

CAES compressed air energy storage

CFL Courant Friedrichs Lewis

CTZ capillary transition zone

GHG greenhouse gas

IMPES implicit pressure, explicit saturation

IMPET implicit pressure, explicit transport

IPCC Intergovernmental Panel on Climate Change

REV representative elementary volume

VE vertical equilibrium

Greek Letters

ϵ_{crit}	criterion threshold	[-]
λ	Brooks-Corey model parameter	[-]
λ_α, Λ_α	mobility of phase α	[(L T)/M]
μ	dynamic viscosity	[M/(L T)]

μ_α	dynamic viscosity of phase α	[M/(L T)]
ν_α	phase mass fraction	[-]
ϕ, Φ	porosity	[-]
Φ_α	potential of phase α	[M/(L^2 T^2)]
$\sigma_{\alpha\beta}$	interfacial tension between phases α and β	[M/T^2]
θ	boundary angle	[-]
φ_α^κ	fugacity coefficient of component κ in phase α	[-]
ϱ	density	[M/L^3]
ϱ_α	density of phase α	[M/L^3]

Roman Letters

$\boldsymbol{d}$	normalized vector connecting the centers of two cells	[L]
$\boldsymbol{J}_\alpha^\kappa$	diffusive mass flux of component κ in phase α	[M/(L^2 T)]
$\boldsymbol{k}$, $\boldsymbol{K}$	permeability tensor	[L^2]
$\boldsymbol{n}_\gamma$	normalized vector orthogonal to the interface γ	[L]
$\boldsymbol{u}$	Darcy velocity	[L/T]
$\boldsymbol{u}_\alpha$, $\boldsymbol{U}_\alpha$	Darcy velocity of phase α	[L/T]
$\boldsymbol{u}_{\text{tot}}$	total Darcy velocity	[L/T]
Δt	time step	[T]
Δx	distance between the center of cells	[L]
$\hat{v}$, $\hat{V}$	total specific volume of all fluid phases	[-]

A	area of interface	$[L^2]$
c^κ, C^κ	total concentration of component κ	$[M/L^3]$
c_α	compressibility factor of α	$[(L\ T^2)/M]$
c_{relPerm}	relative permeability criterion	[-]
c_{sat}	saturation criterion	[-]
c_ϕ	compressibility factor of the solid matrix	$[(L\ T^2)/M]$
d	pore diameter	[L]
f_α	fractional flow function of phase α	[-]
f_α^κ	fugacity of component κ in phase α	$[M/(L\ T^2)]$
g	gravitational acceleration	$[L/T^2]$
H	vertical cell height	[L]
h	gas-phase plume height	[L]
H_α^κ	Henry coefficient of component κ in phase α	$[M/(L\ T^2)]$
h_{tot}	total gas-phase plume height	[L]
k	permeability	$[L^2]$
K_α^κ	mass equilibrium ratio of component κ in phase α	[-]
k_α^κ	mole equilibrium ratio of component κ in phase α	[-]
$k_{r,\alpha}$	relative permeability of phase α	[-]
m^κ	total mass of component κ	[M]
m_α	total mass of phase α	[M]

p_c, P_c	capillary pressure	[M/(L T^2)]
p_e	entry pressure	[M/(L T^2)]
p_α, P_α	pressure of phase α	[M/(L T^2)]
p_{vap}^κ	vapor pressure of component κ	[M/(L T^2)]
q^κ, Q^κ	source/sink term of component κ	[M/(L^3 T)]
q_α, Q_α	source/sink term of phase α	[1/T]
q_α^κ	source/sink term of component κ in phase α	[M/(L^3 T)]
$s_{\alpha,e}$	effective saturation of phase α	[-]
$s_{\alpha,r}$	residual saturation of phase α	[-]
$s_{\alpha,r}^*$	pseudo-residual saturation of phase α	[-]
s_α, S_α	saturation of phase α	[-]
t	time	[T]
t_{seg}	segregation time	[T]
t_{sim}	simulated time	[T]
$u_{\alpha,z}$	vertical component of Darcy velocity of phase α	[L/T]
V	volume of cell	[L^3]
X_α^κ	mass fraction of component κ in phase α	[-]
x_α^κ	mole fraction of component κ in phase α	[-]
z	vertical direction	[L]
z^κ	feed mass fraction	[-]

z_B	bottom of aquifer	[L]
z_p	location of gas-phase plume	[L]
$z_p^{\min}$	minimum location of gas plume	[L]
z_T	top of aquifer	[L]

Abstract

Energy storage is an essential component of future energy systems with a large share of renewable energy. Apart from pumped hydro storage, large scale energy storage is mainly provided by underground energy storage systems. In this thesis we focus on chemical subsurface storage, i.e., the storage of synthetic hydrogen or synthetic natural gas in porous formations.

To improve understanding of the complex and coupled processes in the underground and enable planning and risk assessment of subsurface energy storage, efficient, consistent and adequate numerical models for multiphase flow and transport are required. Simulating underground energy storage requires large domains, including local features such as fault zones and a representation of the transient saline front, and simulation times spanning the whole time of plant operation and beyond. In addition, often a large number of simulation runs need to be conducted to quantify parameter uncertainty, and efficient models are needed for data assimilation as well. Therefore, a reduction of model complexity and thus computing effort is required.

Numerous simplified models that require less computational resources have been developed. In this thesis we focus on a group of multiscale models which use vertically integrated equations and implicitly include fine-scale information along the vertical direction that is reconstructed assuming vertical equilibrium (VE). Classical VE models are restricted to situations where vertical equilibrium is valid in the whole domain during most of the simulated time. This may not be the case for underground energy storage, where simulated times may be too short and locally a high degree of accuracy and complexity may be required, e.g., around the area where gas is extracted for the purpose of energy production. The three core chapters of this thesis present solutions to adapt VE models for the simulation of underground energy storage, with increasing complexity.

In the first main part of this thesis we investigate situations with slow gravity drainage dynamics, e.g., due to highly nonlinear relative permeability relationships. In these cases, classical VE models may not be applicable even for very long simulation times. A modified VE model is developed which introduces a pseudo-residual brine phase saturation inside the gas-phase plume that is initially higher than the natural residual brine phase saturation. During simulation, the pseudo-residual brine phase saturation is updated via explicit analytical calculations to approach the natural residual brine phase saturation. We test the pseudo-VE model on a range of injection scenarios with different parameters, and show that the pseudo-VE model has a much broader applicability than classical VE models while preserving the low computational cost.

The second main part of this thesis focuses on local areas in the domain that have not reached vertical equilibrium due to, e.g., continuing injection or geological heterogeneities, while most other parts of the domain can be considered to be in vertical equilibrium. In such cases, classical VE models may not capture the relevant vertical dynamics locally, which may have an impact on the overall global solution. A multiphysics model is developed which couples an immiscible VE model to an immiscible full multidimensional model. The subdomains are assigned adaptively during simulation based on local criteria that identify regions of the domain where the VE assumption is valid. This way, model complexity can be matched to process complexity. We test the multiphysics model on an injection scenario in a heterogeneous domain and show that the developed model is computationally efficient and maintains a high degree of accuracy, particularly in regions where vertical equilibrium is not valid.

In the last main part of this thesis we investigate situations where compositional processes play a role, e.g., around the extraction region where the composition of the extracted gas phase is of interest. For this purpose we extend the model hierarchy with two compositional models: a compositional VE model and a compositional full multidimensional model. We use our multiphysics framework to adaptively couple both models in one domain, and select subdomains using a compositional VE criterion during simulation. We test our models on a horizontal injection test case and an idealized energy storage test case, where we simulate several injection and extraction periods in a radially symmetric dome-shaped aquifer. The compositional multiphysics model shows to be computationally efficient with a high local accuracy.

Zusammenfassung

Energiespeicherung ist ein wesentlicher Bestandteil zukünftiger Energiesysteme, die einen hohen Anteil Erneuerbarer Energien aufweisen. Neben der Pumpspeicherung werden große Energiespeicher hauptsächlich durch unterirdische Energiespeichersysteme bereitgestellt. Diese Arbeit befasst sich mit der chemischen Speicherung im Untergrund, d.h. der Speicherung von synthetischem Wasserstoff oder synthetischem Erdgas in porösen Formationen.

Zur Verbesserung des Verständnisses der komplexen und gekoppelten Prozesse im Untergrund und um die Planung und Risikobewertung von Energiespeichern im Untergrund zu ermöglichen, sind effiziente, konsistente und adäquate numerische Modelle für Mehrphasenströmung und -transport erforderlich. Die Simulation unterirdischer Energiespeicherung erfolgt auf großen Simulationsgebieten, welche lokale Besonderheiten wie Verwerfungszonen einschließen, und setzt voraus, dass auch die Bewegung der Sole dargestellt werden kann. Simulationszeiten reichen dabei über die gesamte Betriebsdauer der Anlage und darüber hinaus. Zudem muss häufig eine große Anzahl von Simulationsläufen durchgeführt werden, um Parameterunsicherheit zu quantifizieren. Auch für Datenassimilation werden effiziente Modelle benötigt. Daher ist eine Reduzierung der Modellkomplexität und damit des Rechenaufwands erforderlich.

Es existieren zahlreiche vereinfachte Modelle, die weniger Rechenressourcen erfordern. Diese Arbeit konzentriert sich auf eine Gruppe von Multiskalenmodellen, die vertikal integrierte Gleichungen verwenden und implizit Information der feinen Skala enthalten, welche entlang der vertikalen Richtung unter der Annahme eines vertikalen Gleichgewichts (VE) rekonstruiert werden. Klassische VE-Modelle sind auf Situationen beschränkt, in denen das vertikale Gleichgewicht im gesamten Simulationsgebiet während des überwiegenden Teils der simulierten Zeit gültig ist. Dies ist bei unterirdischen Energiespeichern möglicherweise nicht der Fall, da die simulierten Zeiten zu kurz

sein können und lokal ein hohes Maß an Genauigkeit und Komplexität erforderlich sein kann, zum Beispiel in Bereichen, in denen Gas zur Energieerzeugung gefördert wird. Die drei Hauptkapitel dieser Arbeit präsentieren daher Lösungen zur Anpassung von VE-Modellen für die Simulation von unterirdischen Energiespeichern, mit steigender Komplexität.

Im ersten Hauptteil dieser Arbeit untersuchen wir Situationen mit langsamer Schwerkraft-getriebener Drainage, zum Beispiel durch stark nichtlineare relative Permeabilitätsbeziehungen. In diesen Fällen sind klassische VE-Modelle selbst für sehr lange Simulationszeiten möglicherweise nicht anwendbar. Wir entwicklen ein modifiziertes VE-Modell, welches eine pseudo-residuale Sättigung der Sole in der Gasfahne annimmt, die anfänglich höher ist als die natürliche residuale Sättigung der Sole. Während der Simulation wird die pseudo-residuale Sättigung der Sole durch explizite analytische Berechnungen aktualisiert, wobei sie sich der natürlichen residualen Sättigung der Sole annähert. Das Pseudo-VE-Modell wird anhand einer Reihe von Injektionsszenarien mit unterschiedlichen Parametern getestet und es zeigt sich, dass das Pseudo-VE-Modell einen viel breiteren Anwendungsbereich aufweist als klassische VE-Modelle, wobei zugleich die geringen Rechenkosten erhalten bleiben.

Der zweite Hauptteil dieser Arbeit konzentriert sich auf lokal begrenzte Bereiche im Simulationsgebiet, welche sich aufgrund von beispielsweise fortgesetzter Injektion oder durch geologische Heterogenitäten nicht im vertikalen Gleichgewicht befinden, während der übrige Großteil des Simulationsgebiets vertikales Gleichgewicht aufweist. In solchen Fällen erfassen klassische VE-Modelle nicht die möglicherweise vorhandene, lokal relevante vertikale Dynamik, welche Auswirkungen auf die globale Gesamtlösung haben kann. Wir entwickeln ein Multiphysikmodell, welches ein nicht mischbares VE-Modell mit einem nicht mischbaren volldimensionalen Modell koppelt. Teilgebiete werden den einzelnen Modellen während der Simulation adaptiv anhand lokaler Kriterien zugewiesen, welche Bereiche im Simulationsgebiet identifizieren, in denen die VE-Annahme gültig ist. Auf diese Weise kann die Modellkomplexität an die Prozesskomplexität angepasst werden. Wir testen das Multiphysikmodell an einem heterogenen Injektionsszenario und zeigen, dass das entwickelte Modell rechnerisch effizient ist und ein hohes Maß an Genauigkeit aufweist, insbesondere in Regionen, in denen vertikales Gleichgewicht nicht gültig ist.

Im letzten Hauptteil dieser Arbeit untersuchen wir Situationen, in denen Mischungs-

vorgänge eine Rolle spielen. Dies ist beispielsweise um das Extraktionsgebiet herum der Fall, da dort die Zusammensetzung der extrahierten Gasphase von Interesse ist. Zu diesem Zweck erweitern wir die Modellhierarchie um zwei weitere Modelle, die beide Mischungsvorgänge berechnen können: ein Zweikomponenten-VE-Modell und ein volldimensionales Zweikomponenten-Modell. Wir verwenden unser Multiphysikkonzept, um beide Modelle in einem Simulationsgebiet adaptiv zu koppeln und identifizieren während der Simulation Teilgebiete anhand eines Zweikomponenten-VE-Kriteriums. Wir testen unsere Modelle an einer horizontalen Injektion und einem idealisierten Energiespeicher. Letzterer simuliert mehrere Injektions- und Extraktionsperioden in einem radialsymmetrischen, kuppelförmigen Aquifer. Das Zweikomponenten-Multiphysikmodell erweist sich als rechnerisch effizient mit einer hohen lokalen Genauigkeit.

1 Introduction

1.1 Motivation

The Intergovernmental Panel on Climate Change (IPCC) concludes in its Fifth Assessment Report [IPCC, 2014] that climate change is unequivocal, and that human activities, in particular emissions of greenhouse gases (GHG), are extremely likely to be the dominant cause. The report states that changes are observed in all geographical regions: the atmosphere and oceans are warming, the amounts of snow and ice are diminishing, sea levels are rising and extreme weather events like, e.g., warm temperature extremes and heavy precipitation are more intense and frequent. According to the IPCC, continued emission of GHG will cause further warming, further rise in sea levels, and long-lasting changes in the climate system, increasing the likelihood of critical, pervasive and irreversible impacts for people and ecosystems. To prevent the most severe impacts of climate change, parties to the UN Framework Convention on Climate Change agreed a target of keeping the rise in average global temperature since pre-industrial levels below 2 °C, and to consider lowering the target to 1.5 °C in the near future [UNFCCC, 2010]. However, this goal will require an urgent and fundamental departure from business as usual. Moreover, the longer action is delayed, the more it will cost and the greater the technological, economic, social and institutional challenges will be.

Global CO_2 emissions are largely associated with the burning of fossil fuels and the energy sector. Emissions of CO_2 from fossil fuel combustion and industrial processes caused about 78% of the total GHG emissions increase from 1970 to 2010 [IPCC, 2014]. In 2010, CO_2 emissions from fossil fuel combustion, cement production and flaring contributed to about 90% of the global CO_2 emissions, as shown in figure 1.1. In 2019, the electric power sector alone accounted for nearly 40% of GHG emissions

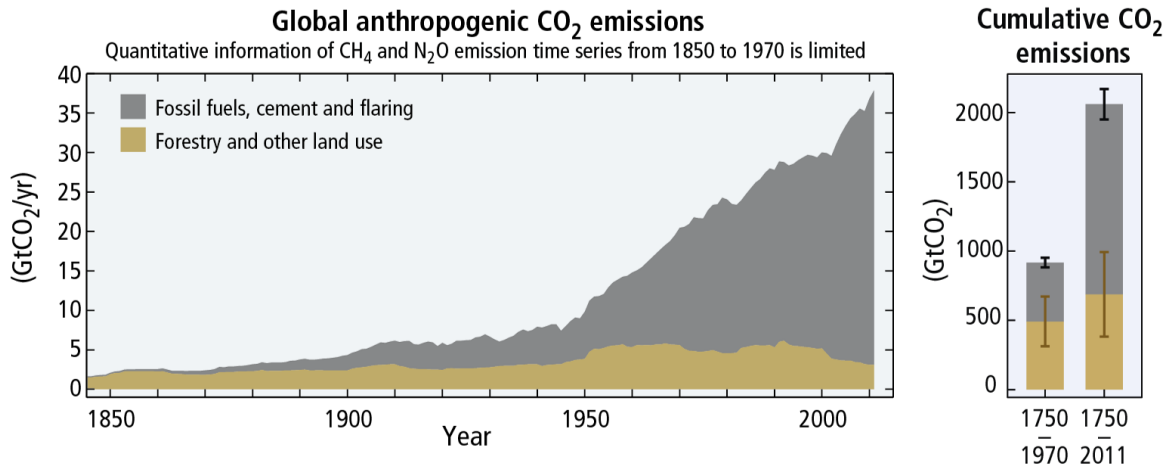

Figure 1.1: Global anthropogenic CO_2 emissions from forestry and other land use as well as from burning of fossil fuel, cement production and flaring. Cumulative emissions of CO_2 from these sources and their uncertainties are shown as bars and whiskers, respectively, on the right hand side. Reprinted from IPCC [2014], figure 1.5, with permission from IPCC, copyright 2015.

across the energy sector, dominated by emissions from burning coal [IEA, 2020a].

According to IPCC [2014] there are multiple mitigation pathways that are likely to limit warming to below 2 °C relative to pre-industrial levels. These pathways would require substantial emission reductions over the next few decades and near zero emissions of most GHG by the end of the century. Among other measures, the share of low-carbon electricity generation, e.g., renewable energy, will need to triple or quadruple by 2050. Driven by the significant potential for reducing GHG emissions, renewable energy sources are becoming more competitive. According to IEA [2020b], renewables-based electricity generation increased by 6.5% in 2019, which is the highest rate of generation growth. Moreover, in 2019, renewable energy provided 27% of the world's electricity supply – the highest level ever recorded. Only a small fraction of renewable potential has been tapped so far; estimates suggest that aggregated global technical potential for renewable energy as a whole is significantly higher than global energy demand [IPCC, 2014].

However, renewable energy like wind or solar power experiences intermittency as a combination of natural variability and partial unpredictability. The energy output is therefore typically not aligned with industrial and consumer needs. Additionally, most renewable energy depends on resources that are location-dependent. As a result,

electric energy is produced at a location that is not necessarily the same where it is needed, resulting in challenging transmission and distribution of energy. Energy storage is therefore an essential component of future energy systems that use large amounts of variable renewable resources [Denholm et al., 2010]. Large-scale energy storage is mainly provided by pumped hydro storage, which is restricted to a suitable topography and limited by ecological and social constraints [Kanakasabapathy, 2013]. In this context, underground energy storage can be a way to ensure large-scale energy storage in the future, since geological formations have the potential to store large volumes of fluids with minimal impact to environment and society [Matos et al., 2019].

1.2 Energy storage in the subsurface

Subsurface energy storage may potentially provide medium to long term (within a day up to several weeks or seasons) storage of energy required for bridging power and energy management [Evans, 2007, Bauer et al., 2013]. Three categories of subsurface energy storage can be identified, associated with three physical mechanisms: mechanical, chemical and thermal energy storage. Mechanical storage includes compressed air energy storage (CAES) and underground pumped hydro storage, chemical storage means synthetic hydrogen and synthetic natural gas storage, and thermal storage is associated with underground thermal energy storage. Conventional CAES are hybrid air-storage/gas-combustion plants, but can be combined with thermal storage to form adiabatic CAES that functions without the combustion of natural gas [Barbour et al., 2015]. Synthetic hydrogen can be produced by using surplus electric energy for hydrolysis. In a subsequent step via the Sabatier process and by adding CO_2, hydrogen can be converted to synthetic methane. Due to its high energy density, chemical storage offers a good possibility to store large amounts of energy, as opposed to mechanical and thermal storage [Bauer et al., 2013]. Two types of geological formations can be identified that are suitable for large-scale subsurface energy storage: engineered cavities, such as salt or hard-rock caverns, and porous formations, such as saline aquifers or depleted hydrocarbon reservoirs. In this thesis we focus on chemical subsurface storage, i.e., methane and hydrogen, in porous formations, i.e., saline aquifers.

The increased need for large-scale geological storage capacities leads to a competition for storage sites and with other planned or already existing types of subsurface use

[Bauer et al., 2013]. The numerous ways of using the subsurface include groundwater abstraction for drinking water purposes, shallow or deep geothermal energy production, mining of ores, coal or geomaterials, hydrocarbon production, CO_2 storage, or disposal of hazardous materials or waste. Underground energy storage systems are often located in the same aquifers used for public drinking water supply [Bonte et al., 2013]. In addition, environmental risks are of concern, including impacts on hydrological, thermal, chemical, and microbiological systems [Bonte et al., 2011]. As an example for gas storage in porous formations, the pressure in the formation will increase due to the injection of the storage gas, and the pressure signal will have a much larger radius of influence than the plume of the injected gas itself (see, e.g., Birkholzer et al. [2009], Zhou and Birkholzer [2011], Benisch and Bauer [2013]). The increased pressure may lead to rock deformation, causing land rise or subsidence. In addition, brine movement may be induced, which may rise to higher formations and could reach drinking water aquifers in cases of conductive pathways. Leakage of gas is of concern as well as geochemical reactions, either directly where the gas phase is located or through dissolved gas transported in brine. As a result, a thorough understanding of the governing processes is required for a sustainable and optimal planning of subsurface use.

1.3 Modeling challenges

Numerical models can be a tool to gain understanding of the complex and coupled processes associated with subsurface energy storage and enable planning of subsurface storage applications. Numerical models face several challenges in this context: Depending on the storage purpose, energy must be stored for a certain time interval and reproduced within a certain time span, defining the boundary conditions and constraints on the technology. However, physical processes inside the domain take place on several scales in space and time, ranging from meters to kilometers and seconds to years. As an example, the storage aquifer may be only a few tens of meters thick, but can span several hundred to thousand meters in the horizontal direction, whereas heterogeneities on relatively small length scales of several meters may significantly influence the overall flow and transport processes. Additionally, complex processes such as dissolution only take place in some parts of the domain (e.g., near the injection area where two phases are present), on the pore scale. Dissolution may be quick across these scales, while

transport of dissolved components by, e.g, diffusion, is a much slower process. Modeling all complex physical processes on the smallest scales everywhere is computationally expensive and may practically be unfeasible. In addition, often a large number of simulation runs need to be conducted to quantify parameter uncertainty, e.g., by Monte Carlo simulation. Efficient models are needed as well to integrate measurements during simulation to improve predictions, e.g., by means of data assimilation. Additionally, limited data on geological parameters often prevent the use of complex models with a high number of input parameters. Therefore, a reduction of model complexity and thus computational cost is required.

Various methods have been developed to efficiently model flow and transport phenomena in porous media on large scales. Two groups of models can be identified, which match model complexity to complexity of the physical processes: multiphysics models (see, e.g., Wheeler and Peszyńska [2002] and Helmig et al. [2013] for an overview regarding multiphase flow) and multiscale models (see, e.g., Singh et al. [2019] for a comparison between upscaling and multiscale methods, and Hajibeygi et al. [2020] for a benchmark study on homogenization and multiscale methods), as well as a combination with adaptive grid refinement [Trangenstein and Bell, 1989]. Multiphysics concepts adapt the model complexity locally, e.g., by splitting the domain in subdomains that are treated with a different set of equations and coupled across the subdomain boundary. Multiscale models decrease the number of global degrees of freedom, preserving important fine-scale features. Grid adaptation can be considered as an efficient method for global downscaling.

A group of multiscale models solves vertically integrated equations, implicitly using fine-scale information along the vertical direction that is reconstructed assuming vertical equilibrium (VE) of the two fluid phases [Yortsos, 1995, Lake, 1989]. Vertical equilibrium forms when gas (e.g., methane or hydrogen) is injected into a saline aquifer. A two-phase flow system develops in which the gas phase displaces the resident brine phase and moves laterally outward from the injection point. At the same time, the injected gas phase tends to move upward because of the large density contrast between gas phase and brine phase. Such a vertical equilibrium assumption allows elimination of the vertical dimension by vertical integration of the three-dimensional governing equations, which significantly reduces the computational cost. Some of these vertically integrated models can be solved analytically while more complex versions including, e.g., capillary pressure or heterogeneities, require a numerical solution [Nordbotten and Celia, 2011].

VE models are computationally efficient and have been widely used for modeling fluid migration in the subsurface, e.g., for field-scale applications of CO_2 storage. However, VE models are usually restricted to situations where the VE assumption, i.e, gravity segregation of the fluid phases, holds in most of the domain during most of the simulated time. While this is usually given for CO_2 storage, which involves simulation times of several hundred to thousand years [Nordbotten and Celia, 2011], it may not be the case for subsurface energy storage, which involves a typical operation time of less than 100 years. Moreover, pressure development near the injection/extraction area as well as composition of fluid phases may be of great interest for subsurface energy storage since the gas is to be extracted again. In particular, the VE assumption usually does not hold in the following situations relevant to subsurface energy storage:

1. Slow gravity drainage dynamics, e.g., due to very nonlinear relative permeability relationships, can significantly prolong the time until VE is reached and render VE models unsuitable for shorter time scales.

2. Around the injection/extraction area the VE assumption may not be valid at all times, due to continuous injection or extraction of gas and resulting vertical movement of the fluid phases.

3. The advancing gas-phase plume may encounter heterogeneities that cause time- and space-dependent vertical movement of fluid phases in the domain.

4. Compositional processes are typically not included in simpler VE models, and the requirements for VE may be even stricter if components are involved.

In each core chapter of this thesis, one or two of the above described situations in which the VE assumption may not be valid are investigated, and solutions are developed that are suitable for the application of subsurface energy storage. In particular, an immiscible VE model is adapted for slow gravity drainage dynamics by introducing a pseudo-residual saturation inside the gas-phase plume that accounts for the slow drainage and is analytically updated throughout the simulation. Further, a multiphysics model is developed that uses a full multidimensional model everywhere in the domain where the VE assumption does not hold, and a VE model everywhere else. Subdomains are assigned adaptively based on a local VE criterion. Finally, a VE model for compositional two-phase flow is presented, and the multiphysics framework is expanded to include compositional processes.

While hysteresis may play a role in scenarios involving repeated injection and extraction of gas into brine, and can be included in a VE framework, we focus in this work on the VE assumption and applicability of our models, neglecting hysteresis. We refer, e.g., to Doster et al. [2013b] for the analysis of a hysteresis model in a VE context, to Doster et al. [2013a] for a study on the impact of such a hysteresis model, and to Nilsen et al. [2016a] for application of hysteresis and VE to a large-scale test case.

1.4 Structure of the thesis

Objective of this thesis is the development of efficient, consistent and adequate numerical multiscale and multiphysics models for multiphase flow and transport, tailored to the application of subsurface energy storage. In particular, these models should be suitable for:

- description and prediction of the highly coupled multiphase flow processes and dynamic changes in boundary conditions of subsurface storage;
- assessment of risks concerning the effect of a subsurface storage operation, especially on protected entities like groundwater;
- optimization of operation of subsurface storage applications (e.g. infiltration/withdrawal rates).

The thesis is structured as follows. First, chapter 2 gives a short introduction to the fundamental concepts and equations for modeling flow in porous media. Then, chapter 3 presents a pseudo-VE model that is suitable for situations with slow gravity drainage dynamics. Chapter 4 introduces a multiphysics model that couples an immiscible VE model to an immiscible full multidimensional model, and adaptively assigns subdomains during the simulation, according to the validity of the VE assumption in space and time. Chapter 5 finally extends the multiphysics model and the local VE criteria to compositional flow. Efficiency and accuracy of all models are demonstrated on suitable test cases of gas injection and storage. The thesis is concluded with a summary and an outlook in chapter 6.

2 Fundamentals

A porous medium is a material containing small voids called pores. Natural substances like soil or biological tissues, or manufactured materials such as cement or the gas diffusion layer of fuel cells, can be considered porous media. The pore space of a porous medium is completely occupied by fluids, i.e., gases and liquids. A fluid is a substance that continually deforms under an applied shear stress while solids can at least to some degree resist. If two or more fluids filling the pore space are mostly immiscible and separated by a sharp interface, e.g., water and oil, these fluids are called phases. Phases consist of one or more components. A component represents a chemical element, e.g., hydrogen, or a molecular substance, e.g., pure water. A collection of substances can be considered a (pseudo) component if its composition is assumed to remain constant, e.g., air. While phases are mostly immiscible, they may exchange components by processes like dissolution and evaporation. In this work, the solid matrix defining the pore space of the porous medium is considered to be rigid and inert, hence we do not consider it as a separate, solid phase but refer to it as the solid matrix.

In this chapter, the main concepts and equations applied in this thesis for modeling flow in porous media are presented. Section 2.1 introduces the concept of representative elementary volumes and defines averaged quantities describing the state of a porous medium on a macroscopic level. Based on this, section 2.2 presents the main macroscopic, full multidimensional balance equations describing isothermal two-phase flow in porous media.

2.1 Macroscopic considerations

Flow processes take place inside the pore space of the porous medium. Because of the highly complex geometry of the solid matrix, it is in most cases unfeasible to

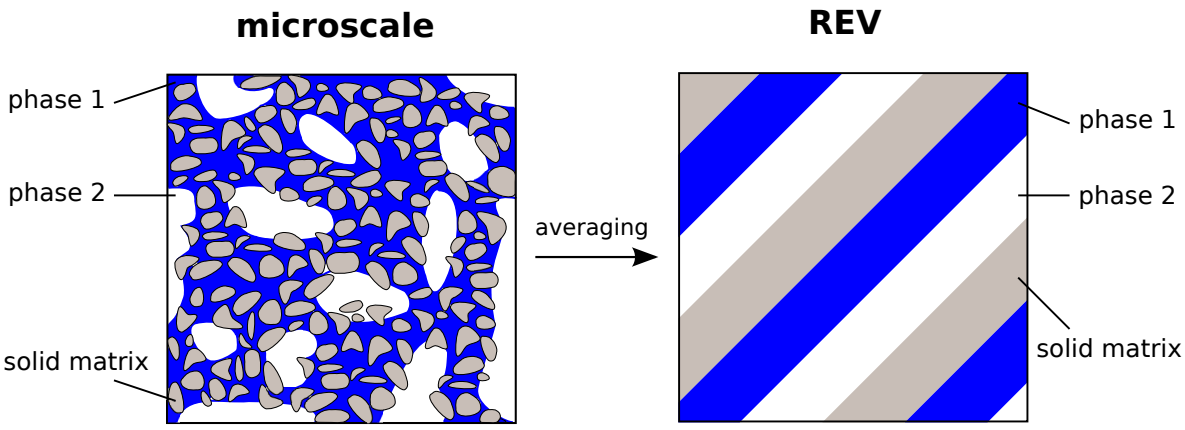

Figure 2.1: Averaging process from pore scale to REV scale

describe the microscopic structure of the pores and compute the flow within each pore, especially when a spatial scale much larger than several pores is of interest. Instead, this thesis uses an REV-based continuum approach to describe porous media on a macroscopic level. For this purpose, properties on the pore scale are averaged over a representative elementary volume (REV), as illustrated in figure 2.1. The concept of the REV was introduced by Bear [1972]. Each phase as well as the solid matrix fill the REV continuously.

The size of an REV is chosen depending on the properties of the porous medium. If a very small part of the porous medium is considered, e.g., on the size of one single pore, and averaged properties of this sample are measured, e.g. volume of pore space, the result of the measurement tends to change dramatically depending on the location of the sample. The sample may consist of one whole pore (100% pore space) or only of solid material (0% pore space). As the sample size increases, these oscillations dampen out until a consistent result is reached. This sample size is referred to as the REV. If the sample size is increased beyond the REV, measurements will remain stable until the sample size starts to include macroscopic heterogeneities.

2.1.1 Porosity and saturation

On the REV scale the exact pore geometry is not accessible anymore. The same REV is continuously filled by several phases and the solid matrix at the same time. Therefore, new averaged quantities to describe the pore space and the distribution of

phases within one REV are required. These quantities are porosity and saturation. Porosity [-] is defined as the ratio of pore space in the REV to the volume of the REV:

$$\phi = \frac{\text{volume of pore space in the REV}}{\text{volume of the REV}}. \tag{2.1}$$

It represents the fraction of REV that is filled by fluids. Porosity can change, e.g., due to the deformation of the solid matrix. Since we consider the solid matrix to be rigid in this thesis, porosity is constant and independent of pressure or other variables.

The pore space is completely filled with fluids. If more than one phase is present, each phase occupies a certain volume of the pore space. The phase saturation [-] represents the fraction of the pore space of an REV that is filled by that phase. It is defined as the ratio of the volume of one phase α to the pore space of the REV:

$$s_\alpha = \frac{\text{volume of phase } \alpha \text{ in the REV}}{\text{volume of pore space in the REV}}. \tag{2.2}$$

The sum of the phase saturations of all present phases must equal one, as the whole pore space is filled with fluids.

2.1.2 Wetting and non-wetting phases

In the following we consider a two-phase system, where we distinguish wetting and non-wetting phases. The degree of wettability is determined by a balance of adhesive and cohesive forces. Cohesion refers to the tendency of similar particles to cling to one another. Adhesion refers to the same tendency between dissimilar particles. The cohesive forces among particles of a liquid are responsible for surface tension. Inside the liquid where each molecule is surrounded by other molecules, every molecule is pulled equally in every direction by its neighbor. Consequently, the net forces sum up to zero. The molecules at the surface however are not completely surrounded by other molecules and mainly pulled inside by their neighbors. This results in internal pressure and forces liquids to minimize their total systems potential energy by contracting their surface to a minimal area. Adhesive forces on the other hand cause an extension of the surface area. The resulting tension at the interface between two phases is called interfacial tension.

At the interface between two phases and the solid matrix the interaction of these forces results in a boundary angle between the solid matrix and the phases. The interfacial tension [M/T^2] between a phase α and the solid matrix is denoted by $\sigma_{s\alpha}$, while σ_{12} refers to the interfacial tension between phase 1 and phase 2. At equilibrium, the sum of the forces is zero and the boundary angle θ [-] between solid matrix and phase 1 can be calculated by Young's equation [Young, 1805] as

$$\theta = \arccos\left(\frac{\sigma_{s2} - \sigma_{s1}}{\sigma_{12}}\right). \tag{2.3}$$

The phase with an acute boundary angle is referred to as the wetting phase, denoted with a subscript w. The phase with an obtuse boundary angle is referred to as the non-wetting phase, denoted with a subscript n.

2.1.3 Capillary pressure and residual saturation

The equilibrium between wetting and non-wetting phase leads to a pressure discontinuity at the interface between both phases. This pressure difference is called the capillary pressure p_c [M/(L T^2)]:

$$p_c = p_n - p_w, \tag{2.4}$$

where p_n and p_w are the non-wetting and wetting phase pressure [M/(L T^2)], respectively. The Young-Laplace equation [Young, 1805, Laplace, 1806] formulates the capillary pressure in a single column filled with two phases depending on the interfacial tension σ_{12}, the boundary angle θ and the pore diameter d [L]:

$$p_c = \frac{4\sigma_{12}\cos\theta}{d}. \tag{2.5}$$

According to the Young-Laplace equation, capillary pressure increases with decreasing pore diameter, and decreases with increasing pore diameter.

On the REV-scale, capillary pressure is defined as the pressure difference between non-wetting and wetting phase as well, and formulated depending on the phase saturation:

$$p_c = p_c(s_w). \tag{2.6}$$

When a wetting phase is replaced by a non-wetting phase it retreats to smaller pores while the non-wetting phase fills the larger pores. In accordance to the Young-Laplace equation (2.5), capillary pressure in the REV is thereby increased. In contrast to that, a wetting phase tends to displace a non-wetting phase from small pores, thereby decreasing capillary pressure. Capillary pressure-saturation relationships reflecting this behavior are given by empirical laws, e.g., by the Brooks-Corey law [Brooks and Corey, 1964]:

$$p_c = p_e(s_{w,e})^{-1/\lambda} = p_e \left(\frac{s_w - s_{w,r}}{1 - s_{w,r} - s_{n,r}} \right)^{-1/\lambda}, \tag{2.7}$$

where $s_{w,e}$ is the effective wetting phase saturation [-], λ is a model parameter [-], and $s_{w,r}$ and $s_{n,r}$ are residual wetting and non-wetting phase saturations [-], respectively. A residual saturation is a volume fraction of a phase that cannot be removed by further displacement. When a wetting phase is displaced by a non-wetting phase it retreats, as mentioned above, to smaller pores. There it can be trapped by the non-wetting phase. When a non-wetting phase is displaced by a wetting phase it retreats to larger pores. There it can be trapped surrounded by the wetting phase in the center of the larger pores. The model parameter λ captures the structure of the porous medium, i.e., the uniformity of pore size, and needs to be determined by fitting to experimental data. In the Brooks-Corey law, the capillary pressure does not reach zero for full wetting-phase saturation but instead reaches the entry pressure p_e [M/(L T^2)]. The entry pressure can be viewed as the pressure that is required to displace the wetting phase from the largest occuring pore.

2.1.4 Intrinsic permeability and relative permeability

The intrinsic permeability $\boldsymbol{k}$ [L^2] is a measure of the inverse resistance that is encountered by fluids flowing through a porous medium. The intrinsic permeability depends only on the structure of the solid matrix and, in the general case of an anisotropic porous medium, is a symmetric and positive definite tensor.

If more than one phase fills the spore space, the presence of the other phases acts like an obstruction that increases flow resistance. If, for example, the saturation of the wetting phase decreases, it retreats to smaller pores. The cross-sectional area for flow is hereby decreased. In addition, the wetting phase is forced to flow through smaller pores and

around bigger pores. The resulting increase in tortuosity lengthens the flow path of the wetting phase. The relative permeability $k_{r,\alpha}$ [-] accounts for this mutual influence, depending on the phase saturation. Relative permeability-saturation relationships are given by empirical laws, e.g., by the Brooks-Corey law [Brooks and Corey, 1964]:

$$k_{r,w} = s_{w,e}^{(2/\lambda+3)}, \quad k_{r,n} = (1 - s_{w,e})^2 \left(1 - s_{w,e}^{(2/\lambda+1)}\right). \tag{2.8}$$

2.2 Darcy's law and balance equations

With the averaged quantities introduced in section 2.1, balance equations to describe isothermal fluid flow in porous media can be formulated. First, a momentum balance (Darcy's law) is presented, followed by a mass and volume balance for immiscible two-phase flow, and a mass balance for compositional two-phase flow. Formulations for the governing equations taking the form of implicit pressure and explicit saturation/transport equation are given for both immiscible and miscible two-phase flow.

2.2.1 Darcy's law for multiphase flow

The average velocity of a single fluid in an REV is commonly described by Darcy's law [Darcy, 1856]. The equation is based on experiments of the flow of water through a sand column. It states that the average fluid velocity $\boldsymbol{u}$ [L/T] over a given cross-section is proportional to the gradient of the piezometric head $h = \frac{p}{\varrho g} + z$ [L], where ϱ is the fluid density [M/L^3], and g is the gravitational acceleration [L/T^2] acting in direction z [L]. Darcy's law can be written as:

$$\boldsymbol{u} = -\frac{1}{\mu}\boldsymbol{k}\left(\nabla p + \varrho g \nabla z\right), \tag{2.9}$$

where μ ist the dynamic fluid viscosity [M/(L T)]. The equation can be generalized for multiphase flow [Bear, 1972, Helmig, 1997] for each phase α:

$$\boldsymbol{u}_\alpha = -\boldsymbol{k}\lambda_\alpha\left(\nabla p_\alpha + \varrho_\alpha g \nabla z\right), \tag{2.10}$$

where $\boldsymbol{u}_\alpha$ is the Darcy velocity of a phase α [L/T], $\lambda_\alpha = \frac{k_{r,\alpha}}{\mu_\alpha}$ is the mobility of a phase α [(L T)/M], and ϱ_α is the density of a phase α [M/L^3].

2.2.2 Immiscible two-phase flow

The specific mass per volume of a phase α inside an REV can be calculated as $\phi s_\alpha \varrho_\alpha$. If solubility processes of one fluid into another are neglected, the mass of a phase in an REV changes only due to transport of mass over the boundary of the REV or due to sources or sinks inside the REV. Transport of a phase can be expressed by the specific mass flux per area $\varrho_\alpha \boldsymbol{u}_\alpha$, with the Darcy velocity $\boldsymbol{u}_\alpha$, and sources or sinks by the specific mass flux per volume $\varrho_\alpha q_\alpha$, with the source/sink term q_α [1/T]. The mass balance for an immiscible phase α inside a porous medium can then be described by the following equation:

$$\frac{\partial \phi s_\alpha \varrho_\alpha}{\partial t} + \nabla \cdot (\varrho_\alpha \boldsymbol{u}_\alpha) = \varrho_\alpha q_\alpha, \quad \alpha = w,\, n, \tag{2.11}$$

where t is the time [T]. In a two-phase system the phase α can either be a wetting phase w or a non-wetting phase n, resulting in two mass balance equations that need to be solved. Considering a rigid solid phase and incompressible fluids, the mass balance equation can be simplified to:

$$\phi \frac{\partial s_\alpha}{\partial t} + \nabla \cdot \boldsymbol{u}_\alpha = q_\alpha, \quad \alpha = w,\, n. \tag{2.12}$$

The multiphase Darcy's law (2.10) can be inserted for the phase velocities $\boldsymbol{u}_\alpha$. The four unknowns are the phase saturations s_α as well as the pressures p_α. To close the system of equations, two additional equations are needed. The saturations are related to each other by the assumption that the entire pore space is filled by fluids, $s_w + s_n = 1$. The pressures are related to each other by the capillary pressure $p_c(s_w) = p_n - p_w$, which is a function of phase saturation.

An alternative formulation for immiscible two-phase flow aims at splitting the governing equations into an implicit pressure equation and an explicit saturation equation. These weakly coupled IMPES (implicit-pressure, explicit-saturation) equations allow for a sequential solution algorithm: the pressure equation is solved first and the saturation equation is solved subsequently. In order to obtain the IMPES formulation for compressible two-phase flow, the mass balance equations (2.11), divided by the phase

density ϱ_α, are added up, resulting in the pressure equation:

$$\frac{\partial \phi}{\partial t} + \sum_\alpha \frac{1}{\varrho_\alpha} \left(\phi s_\alpha \frac{\partial \varrho_\alpha}{\partial t} + \nabla \varrho_\alpha \cdot \boldsymbol{u}_\alpha \right) + \nabla \cdot \boldsymbol{u}_{\text{tot}} = \sum_\alpha q_\alpha, \quad \alpha = w,\, n, \tag{2.13}$$

with the total Darcy velocity $\boldsymbol{u}_{\text{tot}} = \boldsymbol{u}_b + \boldsymbol{u}_g$ [L/T]. This formulation eliminates the temporal derivative of saturation by making use of the closure equation $s_w + s_n = 1$. The temporal derivatives of porosity and density, respectively, can be related to the temporal derivative of pressure by:

$$\frac{\partial \phi}{\partial t} = \frac{\partial \phi}{\partial p_\alpha} \frac{\partial p_\alpha}{\partial t} = c_\phi \frac{\partial p_\alpha}{\partial t}, \tag{2.14}$$

$$\frac{1}{\varrho_\alpha} \frac{\partial \varrho_\alpha}{\partial t} = \frac{1}{\varrho_\alpha} \frac{\partial \varrho_\alpha}{\partial p_\alpha} \frac{\partial p_\alpha}{\partial t} = c_\alpha \frac{\partial p_\alpha}{\partial t}, \tag{2.15}$$

with the compressibility factors c_ϕ [(L T^2)/M] and c_α [(L T^2)/M] of the solid matrix and phases, respectively, which are determined empirically and often assumed to be constants. Furthermore, equation (2.13) may be simplified assuming slight compressibility and consequently neglecting the spatial derivative of density. In the case of a rigid solid matrix and incompressible fluids, the pressure equation simplifies to:

$$\nabla \cdot \boldsymbol{u}_{\text{tot}} = \sum_\alpha q_\alpha, \quad \alpha = w,\, n. \tag{2.16}$$

Using the closure equation $p_c(s_w) = p_n - p_w$, one of the phase pressures can be eliminated, resulting in implicit equations for one phase pressure with weak coupling to saturation. The explicit saturation equation is chosen as one of the mass balance equations, either for compressible two-phase flow (2.11), or incompressible two-phase flow (2.12). In the sequential solution algorithm, the values for secondary variables like saturation and, in the compressible case, density, are taken from the previous time step. Iterations within one time step may be necessary if the coupling of the equations is too strong.

2.2.3 Compositional two-phase flow

The specific mass per volume of a component κ inside an REV is calculated as $\sum_\alpha \phi s_\alpha \varrho_\alpha X_\alpha^\kappa$, with the mass fraction X_α^κ [-], which denotes the ratio of mass of component κ in phase

α to total mass of phase α. The mass of a component in an REV changes again due to transport of mass over the boundary of the REV, and due to sources or sinks inside the REV. Transport of a component splits into an advective part, the specific mass flux per area $\sum_\alpha X_\alpha^\kappa \varrho_\alpha \boldsymbol{u}_\alpha$, and a diffusive part, the specific mass flux per area $\sum_\alpha \boldsymbol{J}_\alpha^\kappa$ [M/(L^2 T)]. Sources or sinks can be expressed by the specific mass flux per volume q^κ [M/(L^3 T)] for each component κ. The mass balance equation for each component κ is then given as:

$$\sum_\alpha \frac{\partial \left(\phi s_\alpha \varrho_\alpha X_\alpha^\kappa\right)}{\partial t} + \nabla \cdot \left(\sum_\alpha X_\alpha^\kappa \varrho_\alpha \boldsymbol{u}_\alpha + \boldsymbol{J}_\alpha^\kappa \right) = q^\kappa, \quad \alpha = w,\, n. \tag{2.17}$$

The multiphase Darcy's law (2.10) can be inserted for the phase velocities $\boldsymbol{u}_\alpha$ here as well, and the same closure equations as for immiscible phases apply.

The governing equations for compositional two-phase flow can be formulated in terms of an implicit pressure and an explicit transport (IMPET) equation, as well. To this end, a pressure equation balancing the fluid volume instead of mass was first proposed by Acs et al. [1985]. Similar pressure equations can be found in Watts [1986] and Coats [2000]. The derivation in this thesis follows Van Odyck et al. [2009], starting with the total specific volume of all fluid phases $\hat{v}$ [-], which equals the porosity ϕ:

$$\hat{v} = \phi. \tag{2.18}$$

A Taylor series expansion on the left hand side and neglecting higher order terms leads to:

$$\frac{\partial \hat{v}}{\partial t} = \frac{\phi - \hat{v}}{\Delta t}. \tag{2.19}$$

The right hand side of this equation is called the residual and introduced because it leads to higher stability in the sequential scheme where changes in fluid density due to partial miscibility and compressibility are not implicitly incorporated. The total specific volume of fluid phases is a function of pressure (can be expressed as any of the phase pressures p_α) and the total concentration of the components c^κ [M/L^3]:

$$\frac{\partial \hat{v}}{\partial t} = \frac{\partial \hat{v}}{\partial p}\frac{\partial p}{\partial t} + \sum_\kappa \frac{\partial \hat{v}}{\partial c^\kappa}\frac{\partial c^\kappa}{\partial t}. \tag{2.20}$$

The component transport can be calculated according to equation (2.17), rewritten in

terms of the total concentration c^κ:

$$\frac{\partial c^\kappa}{\partial t} = -\nabla \cdot \left(\sum_\alpha X_\alpha^\kappa \varrho_\alpha \mathbf{u}_\alpha + \boldsymbol{J}_\alpha^\kappa \right) + q^\kappa, \quad \alpha = w,\, n. \tag{2.21}$$

Inserting equation (2.20) and (2.21) into (2.19) leads to the final pressure equation:

$$\frac{\partial \hat{v}}{\partial p}\frac{\partial p}{\partial t} - \sum_\kappa \frac{\partial \hat{v}}{\partial c^\kappa} \nabla \cdot \left(\sum_\alpha X_\alpha^\kappa \varrho_\alpha \mathbf{u}_\alpha + \boldsymbol{J}_\alpha^\kappa \right) + \sum_\kappa \frac{\partial \hat{v}}{\partial c^\kappa} q^\kappa = \frac{\phi - \hat{v}}{\Delta t}, \quad \alpha = w,\, n. \tag{2.22}$$

This equation balances volume changes due to compositional changes with changes in the pressure field. The extension of Darcy's law for multiphase flow (2.10) is taken to compute $\boldsymbol{u}_\alpha$. One of the two pressures can be eliminated from the equation using the capillary pressure $p_c = p_n - p_w$ to close the system of equations.

3 Pseudo-vertical equilibrium model [1]

A group of simplified models solves vertically integrated equations under the assumption of vertical equilibrium. These VE models are computationally efficient and have proven to be well suited for modeling fluid migration in the subsurface. However, they rely on the assumption of instant gravity segregation of the two fluid phases which may not be valid especially for systems that have very slow drainage at low brine phase saturations. In these cases, the time scale for the brine phase to reach vertical equilibrium can be several orders of magnitude larger than the time scale of interest, rendering conventional VE models unsuitable. Here, we present a pseudo-VE model that relaxes the assumption of instant segregation of the two fluid phases by applying a pseudo-residual saturation inside the plume of the injected fluid that declines over time due to slow vertical drainage. This pseudo-VE model is cast in a multiscale framework for vertically integrated models with the vertical drainage solved as a fine-scale problem. Two types of fine-scale models are developed for the vertical drainage, which lead to two pseudo-VE models. We show that the pseudo-VE models have much wider applicability than the conventional VE model while maintaining the computational benefit of the conventional VE model.

This chapter is based in large parts on the work published in Becker et al. [2017] and structured as follows: Section 3.1 first gives a review of conventional VE models and the VE assumption. Then, section 3.2 introduces the pseudo-vertical equilibrium concept and the multiscale framework for VE models, followed by section 3.3, which presents the pseudo-VE model. Finally, section 3.4 shows comparisons of the two pseudo-VE models, the conventional VE model, and the full multidimensional model, to demonstrate the applicabilities of the new pseudo-VE models.

[1] Large parts of this chapter are taken and partly modified from Becker et al. [2017]

3.1 VE models

Analytical solutions to gravity-segregated flow have been developed assuming lateral symmetry for unconfined aquifers [Huppert and Woods, 1995, Lyle et al., 2005, Golding et al., 2011] and for confined aquifers [Nordbotten and Celia, 2006a, Hesse et al., 2007, Dentz and Tartakovsky, 2009, Juanes et al., 2010, Pegler et al., 2014, Zheng et al., 2015, Guo et al., 2016b] with later works primarily focused on CO_2 sequestration. VE models have to be solved numerically if capillary pressure or heterogeneities are included. These numerical VE models rely on integrated equations with numerically upscaled parameters depending on the phase distribution in the vertical extent [Nordbotten and Celia, 2011].

VE models have been applied to field-scale applications [Person et al., 2010, Nilsen et al., 2011, Gasda et al., 2012, Bandilla et al., 2012, 2014, Bandilla and Celia, 2017] and benchmark exercises [Class et al., 2009, Nordbotten et al., 2012]. For certain injection conditions, VE models have been found to be even more accurate than conventional 3D simulations [Ligaarden and Nilsen, 2010]. The applicability of the VE models are discussed in Court et al. [2012] and Nordbotten and Celia [2011] with regard to temporal and spatial scales. For the VE assumption to hold, the brine and gas phase need to segregate until a hydrostatic pressure profile in the vertical direction is reached. The time scale for segregation of the two fluid phases in the vertical direction needs to be short relative to the time scale of interest, and varies depending on geological parameters and the properties of the fluid. The permeability in the vertical direction plays an especially important role, with larger permeabilities leading to shorter segregation times.

For some cases, the time until the VE assumption is valid can be much longer than the time scales of interest, even if the permeability in the vertical direction is large. For nonlinear relative permeability functions, like the commonly used Brooks-Corey power law, the relative permeability of the brine phase approaches zero during the drainage process, leading to a slow-down of the drainage with time. Such slow drainage may be captured by solving a sub-scale problem in the vertical direction in a vertically integrated framework introduced by Nordbotten and Celia [2011]. In this framework, the vertically integrated equations correspond to the coarse scale while the underlying saturation profile in the vertical direction is the fine scale, as illustrated in figure 3.1. In the

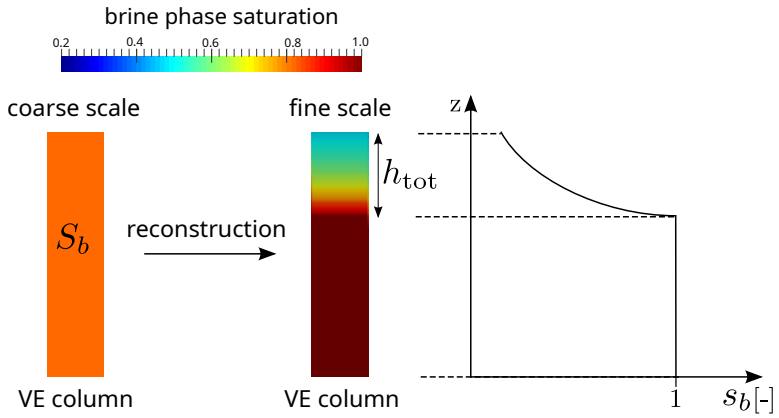

Figure 3.1: Coarse scale saturation and fine scale saturation in the vertically integrated framework. Parameters like, e.g., pressure, relative permeability, permeability and porosity can be treated analogously. Integrated parameters, denoted by uppercase letters, exist on the coarse scale, and are the basis on which fine-scale parameters, denoted by lowercase letters and varying with depth, are reconstructed. h_{tot} [L] refers to the region where the gas phase is present on the fine scale.

case of conventional VE models, the fine-scale solution is solved analytically using the VE assumption. Guo et al. [2014] extended this multiscale framework and developed a vertically integrated model that does not rely on the VE assumption. This is done by solving one-dimensional vertical flow dynamics as fine-scale problems for each of the coarse-scale numerical grid cells at every time step. However, the dynamic computations in the vertical direction come with a slightly higher computational demand than conventional VE models. If capillary forces and gravity effects in the horizontal velocity are neglected, this model is equivalent to the asymptotic approach presented by Yortsos [1995], which results in a single nonlocal equation for the saturation ([Armiti-Juber and Rohde, 2019]).

In the following, section 3.1.1 presents the governing equations of a conventional immiscible VE model, while section 3.1.2 explains the reconstruction of the fine-scale solution for this model.

3.1.1 Governing equations of immiscible VE model

The VE assumption postulates that the two fluid phases have segregated due to buoyancy (i.e., no more vertical flow), and that the phase pressures have reached gravity-capillary equilibrium in the vertical direction. With the VE assumption, the form of

the pressure distribution is known, *a priori*, in the vertical direction. This can be used to simplify the governing equations of fluid flow and leads naturally to vertical integration of the governing equations with associated reduction of dimensionality. The details along the vertical direction can be reconstructed from the imposed equilibrium pressure distribution.

In the following we assume that the wetting phase is liquid (e.g., brine) and the non-wetting phase is gaseous, and we use the subscripts $\alpha = b,\, g$ throughout the rest of the thesis to indicate the wetting brine phase and non-wetting gas phase. Since the gas phase is less dense than the brine phase, the gas phase consequently forms a plume below a no-flow upper boundary. Furthermore, in this chapter we assume that the fluids are immiscible and incompressible. For simplicity of presentation, we assume an aquifer with impermeable top and bottom. The mass balance equation (2.12) is integrated over the vertical direction from the bottom of the aquifer, z_B [L], to the top of the aquifer, z_T [L], to derive the coarse-scale equations for the VE model:

$$\int_{z_B}^{z_T} \phi \frac{\partial s_\alpha}{\partial t} dz + \int_{z_B}^{z_T} \nabla \cdot \boldsymbol{u}_\alpha dz = \int_{z_B}^{z_T} q_\alpha dz, \quad \alpha = b,\, g. \tag{3.1}$$

We note that z is aligned with the direction of gravitational acceleration. We introduce the depth-integrated parameters:

$$\Phi = \int_{z_B}^{z_T} \phi dz, \tag{3.2}$$

$$S_\alpha = \frac{1}{\Phi} \int_{z_B}^{z_T} \phi s_\alpha dz, \tag{3.3}$$

$$\boldsymbol{U}_\alpha = \int_{z_B}^{z_T} \boldsymbol{u}_{\alpha,//} dz, \tag{3.4}$$

$$Q_\alpha = \int_{z_B}^{z_T} q_\alpha dz, \tag{3.5}$$

with the subscript '//' denoting the xy-plane. This results in the depth-integrated equations:

$$\Phi \frac{\partial S_\alpha}{\partial t} + \nabla_{//} \cdot \boldsymbol{U}_\alpha = Q_\alpha, \quad \alpha = b,\, g. \tag{3.6}$$

The depth-integrated Darcy velocity is found by vertically integrating Darcy's law over

the height of the aquifer as:

$$\boldsymbol{U}_\alpha = -\boldsymbol{K}\Lambda_\alpha \left(\nabla_{//} P_\alpha + \varrho_\alpha g \nabla_{//} z_B\right), \quad \alpha = b,\, g, \tag{3.7}$$

with the depth-integrated permeability and depth-averaged mobility:

$$\boldsymbol{K} = \int_{z_B}^{z_T} \boldsymbol{k}_{//} dz, \tag{3.8}$$

$$\Lambda_\alpha = \boldsymbol{K}^{-1} \int_{z_B}^{z_T} \boldsymbol{k}_{//} \lambda_\alpha dz, \quad \alpha = b,\, g. \tag{3.9}$$

The coarse-scale pressure P_α of phase α in the vertically integrated Darcy's law is defined as the phase pressure at the bottom of the aquifer.

Two closure equations are required again to solve for the four unknown primary variables P_α and S_α: $S_b + S_g = 1$ and the coarse-scale pseudo capillary pressure $P_c(S_b) = P_g - P_b$ that relates the coarse-scale pressure difference at the bottom of the aquifer to the coarse-scale saturation. The coarse-scale gas phase pressure at the bottom of the aquifer P_g is constructed from the linear extension of the pressure distribution for the gas phase inside the plume to regions below that.

3.1.2 Reconstruction

We solve the coarse-scale equations (3.6) with the depth-integrated Darcy velocity (3.7) inserted. After the coarse-scale problem is solved, the fine-scale solution in the vertical direction can be reconstructed based on the coarse-scale quantities P_α and S_α (see figure 3.2). The fine-scale pressure is reconstructed based on the above stated assumption of a hydrostatic pressure profile. Given the two fine-scale phase pressures at every point in the vertical direction, the fine-scale capillary pressure function $p_c(s_b)$ can be inverted to give the fine-scale saturation profile. The saturation profile determined this way still contains one unknown, the vertical location of the gas-phase plume z_p [L], which can be determined by balancing the volume of the phases in the VE cell. The fine-scale saturation profile is used to calculate the fine-scale relative permeability. By integrating the fine-scale relative permeability using equation (3.9), the coarse-scale relative permeability can be updated.

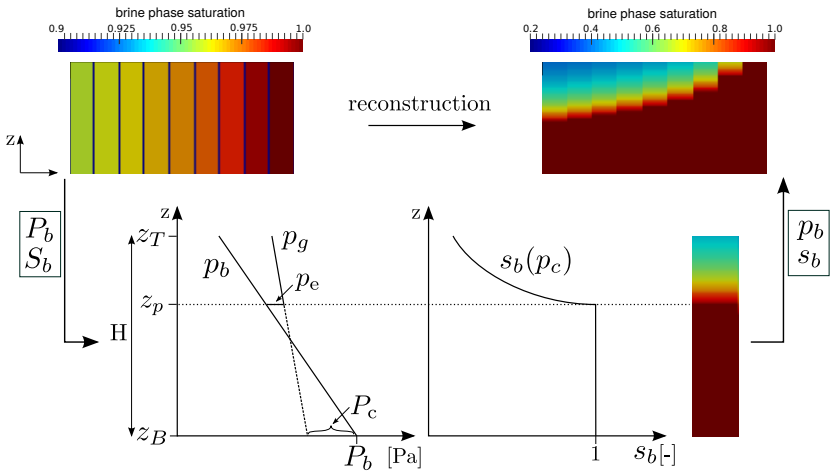

Figure 3.2: Reconstruction of the fine-scale solution in the vertical direction (top right) based on the computed coarse-scale solution (top left). The assumption of vertical equilibrium leads to hydrostatic pressure profiles for brine and gas phase (bottom left), which can be constructed based on the coarse-scale brine phase pressure P_b and coarse-scale pseudo capillary pressure P_c at the bottom of the aquifer. The brine phase saturation profile in the vertical direction (bottom right) results from the inverse of the fine-scale capillary pressure function. Adapted from Becker et al. [2017] with permission from John Wiley & Sons, copyright 2017.

In the following, the equations for the reconstructed pressure and saturation profiles are given for a VE model neglecting capillary pressure on the fine scale (sharp interface model), and a VE model with a capillary transition zone. For simplification we assume that the porosity is constant in the VE cell and we choose the brine phase pressure P_b as our primary pressure variable. Further, in this chapter we omit the case in which the plume has an area with residual gas phase below the plume, e.g., due to extraction. If an area with residual gas phase below the plume is present, additionally the minimum vertical location of the gas-phase plume $z_p^{\min}$ [L], known from the previous time step, is used in the reconstruction. A detailed description of the reconstruction procedure with residual gas phase below the plume can be found in section 5.2.7.

Reconstruction for sharp interface model

Pressure reconstruction: Since there is no capillary pressure on the fine scale of the sharp interface VE model, both phase pressures are equal along the vertical direction.

This leads to the following phase pressure distribution along the vertical direction:

$$p_b(z) = p_g(z) = \begin{cases} P_b - \varrho_b g(z_p - z_B) - \varrho_g g(z - z_p), & z_p < z \leq z_T, \\ P_b - \varrho_b g(z - z_B), & z_B \leq z \leq z_p. \end{cases} \tag{3.10}$$

Saturation reconstruction: The brine phase saturation along the vertical direction is straightforward:

$$s_b(z) = \begin{cases} s_{b,r}, & z_p < z \leq z_T, \\ 1, & z_B \leq z \leq z_p. \end{cases} \tag{3.11}$$

The calculation of z_p is based on a balance of the total volume of phases within the cell. Without a region of immobile gas phase below the mobile plume, z_p is:

$$z_p = z_B + H \frac{S_b - s_{b,r}}{1 - s_{b,r}}, \tag{3.12}$$

with the vertical height of the cell $H = z_T - z_B$ [L].

Reconstruction for capillary transition model

Pressure reconstruction: Due to taking capillary pressure into account on the fine scale of the capillary transition VE model, the phase pressures differ according to the capillary pressure depending on saturation. The entry pressure, p_e, is the (constant) difference between the phase pressures at $s_b \geq 1.0 - s_{g,r}$. The phase pressures along the vertical direction follow as:

$$p_b(z) = P_b - \varrho_b g(z - z_B), \tag{3.13}$$

$$p_g(z) = \begin{cases} P_b - \varrho_b g(z_p - z_B) + p_e - \varrho_g g(z - z_p), & z_p < z \leq z_T, \\ P_b - \varrho_b g(z - z_B) + p_e, & z_B \leq z \leq z_p. \end{cases} \tag{3.14}$$

The capillary pressure along the vertical direction can be calculated by subtracting the brine phase pressure from the gas phase pressure:

$$p_c(z) = p_g(z) - p_b(z) = \begin{cases} p_e + (\varrho_b - \varrho_g)g(z - z_p), & z_p < z \leq z_T, \\ p_e, & z_B \leq z \leq z_p. \end{cases} \tag{3.15}$$

The capillary pressure is a function of saturation, e.g., the Brooks-Corey relationship (2.7). Using the Brooks-Corey relationship, the saturation can be reconstructed as follows:

Saturation reconstruction, case 1 ($z_p > z_B$): Reconstruction of the brine phase saturation below the plume is straightforward:

$$s_b(z) = 1, \qquad z_B \leq z \leq z_p. \tag{3.16}$$

For the region of the plume, equation (3.15) is set equal to the Brooks-Corey relationship (2.7), and rearranged for s_b. This leads to an expression for the brine phase saturation inside the plume, depending on the location of the gas-phase plume z_p:

$$s_b(z) = \left(p_e + (\varrho_b - \varrho_g)g(z - z_p)\right)^{-\lambda} p_e^{\lambda}(1 - s_{b,r} - s_{g,r}) + s_{b,r}, \qquad z_p < z \leq z_T. \tag{3.17}$$

To calculate the unknown z_p, we balance the overall volume of brine phase with the integral of the brine phase saturation over the vertical direction:

$$\begin{aligned} \int_{z_p}^{z_T} s_b(z)dz + z_p - z_B &= S_b H \\ = \frac{1}{1-\lambda}\left(p_e + (\varrho_b - \varrho_g)g(z_T - z_p)\right)^{1-\lambda} &\frac{(1 - s_{b,r} - s_{g,r})p_e^{\lambda}}{(\varrho_b - \varrho_g)g} \\ + s_{b,r}(z_T - z_p) - \frac{p_e(1 - s_{b,r} - s_{g,r})}{(1-\lambda)(\varrho_b - \varrho_g)g} &+ z_p - z_B. \end{aligned} \tag{3.18}$$

This equation cannot be easily rearranged to determine z_p, which is why a numerical method, e.g. Newton-Raphson, must be used to solve for it.

Saturation reconstruction, case 2 ($z_p \leq z_B$): In this case, the entire vertical height of the VE cell is filled by the plume region. The distribution is the same as for case 1a:

$$s_b(z) = (p_e + (\varrho_b - \varrho_g)g(z - z_p))^{-\lambda} p_e^{\lambda}(1 - s_{b,r} - s_{g,r}) + s_{b,r}, \qquad z_B \leq z \leq z_T. \quad (3.19)$$

To calculate the unknown z_p, we use again a volume balance of the brine phase:

$$\begin{aligned} \int_{z_B}^{z_T} s_b(z)dz &= S_b H \\ &= \frac{1}{1-\lambda} \left(p_e + (\varrho_b - \varrho_g)g(z_T - z_p)\right)^{1-\lambda} \frac{(1 - s_{b,r} - s_{g,r})p_e^{\lambda}}{(\varrho_b - \varrho_g)g} \\ +s_{b,r}H - \frac{1}{1-\lambda} &\left(p_e + (\varrho_b - \varrho_g)g(z_B - z_p)\right)^{1-\lambda} \frac{(1 - s_{b,r} - s_{g,r})p_e^{\lambda}}{(\varrho_b - \varrho_g)g}. \end{aligned} \quad (3.20)$$

Again, this equation must be solved for z_p numerically.

3.2 Pseudo-vertical equilibrium and multiscale framework

The time scale associated with gravity segregation of the two fluid phases generally depends on physical parameters such as the permeability in the vertical direction, the density difference of the fluids and the height of the confined aquifer [Nordbotten and Dahle, 2011, Hunt et al., 2013, Ewing et al., 2015]. The shape of the relative permeability function can also play a significant role. Commonly used are power functions like the Brooks-Corey law (2.8). As the displaced fluid (oftentimes the brine phase) drains out from the plume of injected fluid due to gravity, the saturation of the brine phase in the plume of the injected fluid decreases. For nonlinear relative permeability-saturation relationships like the Brooks-Corey law, relative permeability is very low for small to medium brine phase saturations and high only for larger saturations (see figure 3.3 for examples of relative permeability-saturation relationships with different parameters). At the same time the driving force (density difference) stays the same. With that, a relative permeability and thus a mobility close to zero means that the flux of the brine phase draining out of the plume decays rapidly as the brine phase saturation decreases toward its residual value. Because of this large power-law nonlinearity of the relative

permeability, the segregation time can be very long, with the saturation of the brine phase not reaching its residual saturation even after hundreds to thousands of years, even if the permeability in the vertical direction is large. In those cases, the gas-phase plume appears to be in equilibrium, in the sense that the brine phase saturation inside the plume stays almost constant over a long period of time although it is still above the ultimate residual saturation and the gas phase is very close to vertical equilibrium. We refer to this type of fluid distribution as pseudo-equilibrium.

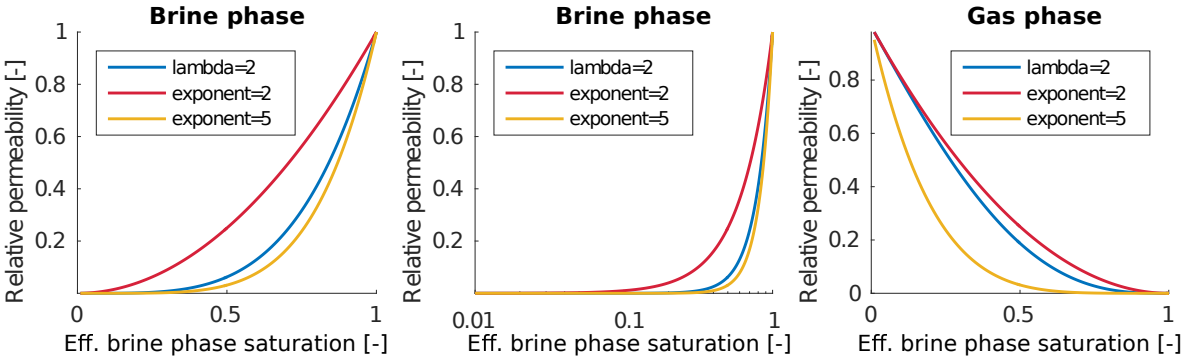

Figure 3.3: Relative permeability as a function of brine phase saturation, for the brine phase (linear and logarithmic scale) and gas phase. Shown is the Brooks-Corey law with $\lambda = 2$ and a power function with exponent 2 and 5 of the form $k_{r,b} = s_{b,e}^{\exp}, \quad k_{r,g} = (1 - s_{b,e})^{\exp}$. See Court et al. [2012] for ranges of parameters in relative permeability functions. Reprinted from Becker et al. [2017] with permission from John Wiley & Sons, copyright 2017.

Conventional VE models do not reflect the slow-down of drainage and assume instant gravity segregation of both phases from the beginning of the simulation. This can lead to inaccurate results, especially for relative permeability functions with large exponents. Figure 3.4 shows the gas phase distribution after 4.5 years of gas injection for a case with a relative permeability function with a large exponent (case 1 in table 3.1). It shows clearly that the full multidimensional reference solution is not reproduced by the conventional VE model even though it appears that gravity segregation has occured and the fluids are close to vertical equilibrium. The full multidimensional reference solution shows a brine phase saturation inside the gas plume that is larger than the ultimate residual saturation, indicating that full segregation has not taken place yet. This brine phase saturation inside the plume acts like a residual saturation because the relative permeability is almost zero at this value, which is why we refer to it as pseudo-residual saturation. The conventional VE model asssumes instant gravity segregation of the two fluid phases, which leads to different saturation profiles in the vertical direction

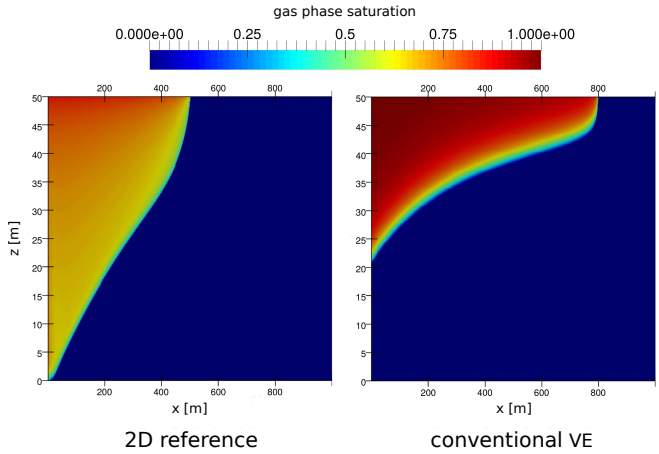

Figure 3.4: Gas injection into a brine-filled confined aquifer with a relative permeability function with large exponent (exponent 5). Shown is the gas plume after 4.5 years for the full multidimensional model (left) and for the conventional VE model (right). Parameters for the simulation are taken from case 1 in table 3.1. Reprinted from Becker et al. [2017] with permission from John Wiley & Sons, copyright 2017.

for the conventional VE model and the full multidimensional model. In the case of nonlinear relative permeability functions, the fine-scale saturation profiles and thus the distribution of the relative permeability in the vertical direction has a direct influence on the conventional VE model. As a result, incorrect representation of the saturation profiles in the vertical direction leads to incorrect prediction of the plume development.

To extend VE models to capture slow gravity drainage due to relative permeability functions with large exponents, we take the multiscale framework from Nordbotten and Celia [2011], extended by Guo et al. [2014], and develop a so-called pseudo-VE model. The pseudo-VE model involves a coarse scale which is identical to the coarse scale of conventional VE models and a fine scale where simple gravity drainage is considered. In the reconstruction step we apply a uniform pseudo-residual brine phase saturation inside the plume which is larger than the ultimate residual saturation of the brine phase. This way, the pseudo-VE model accounts for the pseudo-segregated state of the two fluid phases that can be observed for cases with relative permeability functions with large exponents. A larger residual brine phase saturation was used by Swickrath et al. [2016] as well, leading to improved results compared to full multidimensional models. However, their residual brine phase saturation is constant in both space and time and has to be fitted by running a full multidimensional model. In our model the pseudo-residual saturation is an analytical function derived using physical arguments,

and it is dynamically updated during the simulation at every time step after solving the coarse-scale VE model. This leads to much broader applicability.

We point out that, in terms of complexity, the pseudo VE model is an intermediate model in between the conventional VE model and the dynamic reconstruction model from Guo et al. [2014]. Compared to conventional VE models, the additional computation in the pseudo-VE model is a simple algebraic calculation and therefore we expect the pseudo-VE model to be computationally as fast as conventional VE models.

3.3 Pseudo-VE model

We take the multiscale framework and extend the VE model to capture slow gravity drainage due to relative permeability functions with large exponents. We develop a pseudo-VE model that assumes that due to the slow drainage a vertically uniform pseudo-residual saturation exists within the plume that is larger than the ultimate (long-time) residual saturation and decreases with time. The model solves vertically integrated equations on the coarse scale, and analytically solves the slow gravity drainage as a fine-scale problem, thereby reducing the pseudo-residual saturation dynamically in each time step. The two scales are coupled sequentially. We present two versions of the pseudo-VE model, where the first version assumes a single pseudo-residual saturation inside the entire plume, and the second version assumes varying pseudo-residual saturations along the horizontal direction of the plume. We refer to these models as pseudo-VE models in the sense that we assume they are in vertical equilibrium at every time step with a pseudo-residual saturation that is determined explicitly and continuously updated. The pseudo-VE models have a much broader applicability compared to the conventional VE models and fully maintain the low computational cost.

In the following, section 3.3.1 presents the solution algorithm of the pseudo-VE model, section 3.3.2 explains the general update of the pseudo-residual saturation by formulating vertical fluxes within a VE cell, which represent the slow drainage process, and section 3.3.3 finally introduces the two versions of pseudo-VE models.

3.3.1 Algorithm

By casting the pseudo-VE model into the multiscale framework we can identify two scales that are solved sequentially. On the coarse scale, the vertically integrated equations of the VE model (3.6) with the depth-integrated Darcy velocity (3.7) inserted are solved using an IMPES (implicit-pressure, explicit-saturation, see section 2.2.2) formulation and a cell-centered finite-volume method for discretization in space. The time stepping criterion for the explicit calculation of saturation is based on a Courant-Friedrichs-Lewis (CFL) condition [Courant et al., 1928]. The fine scale is a simple model to capture the slow gravity drainage that updates the residual saturation. It is this simple model that forms the basis of the pseudo-VE approach.

The algorithm of the pseudo-VE model is summarized in figure 3.5. As a first step in the algorithm, an IMPES calculation on the coarse scale is performed. This results in the primary variables on the coarse scale, P_α and S_α, computed at the new discrete time level. Then the fine scale with the drainage process in the vertical direction is taken into account and the pseudo-residual saturation inside the plume is updated. This step is followed by the reconstruction of the fine-scale variables, where the updated pseudo-residual saturation inside the plume as well as the primary variables are used to reconstruct the solution in the vertical direction. Based on the saturation profile in the vertical direction, the integrated coarse-scale relative permeability and coarse-scale capillary pressure are determined. These coarse-scale quantities are then applied for the next IMPES time step on the coarse scale. Following this algorithm, the pseudo-VE model preserves the low computational cost of the VE model since the explicit calculations of the vertical drainage add very little additional computational effort. We note that we can also solve the pseudo-VE model with a fully implicit time-stepping scheme. Such fully implicit time-stepping will require more computational effort for each time step due to the larger set of unknowns (e.g., vertical drainage state in addition to the usual pressure and saturation variables).

We note that the pseudo-residual brine phase saturation is only used to modify the fine-scale saturation profile. All constitutive relationships depending on saturation (e.g. fine-scale relative permeability-saturation relationship) are not altered, and effective saturations to evaluate those relationships are calculated based on the ultimate residual saturation. Thus, the difference of the pseudo-VE model to the conventional VE model solely lies in the reconstructed fine-scale saturation profile. This profile in turn directly

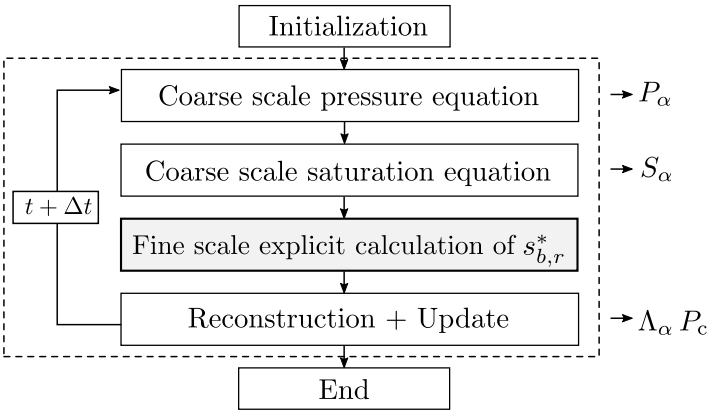

Figure 3.5: IMPES algorithm for the pseudo-VE model solving incompressible isothermal multiphase flow. Adapted from Becker et al. [2017] with permission from John Wiley & Sons, copyright 2017.

affects the value of the coarse-scale relative permeability and coarse-scale capillary pressure, and thus the evolution of the entire plume.

3.3.2 Update of pseudo-residual saturation

The pseudo-residual brine phase saturation inside the plume is determined by computing the drainage flux of the brine phase out of the plume after each coarse-scale time step. To illustrate the approach, we consider a closed vertical column with a plume height h_i [L] and a pseudo-residual saturation $s^*_{b,r,i}$ inside the plume. If capillary forces are present, the time scale to reach vertical equilibrium is smaller since the brine phase saturation does not need to reach low saturation values everywhere inside the plume. For cases with non-zero fine-scale capillary pressure, we define the capillary transition zone (CTZ) as the region of the plume where the brine phase saturation is significantly above residual. Following Court et al. [2012] and Lake [1989], we define the thickness of the transition zone as:

$$CTZ = \frac{p_c(s_{10\%}) - p_e}{(\varrho_b - \varrho_g)g}, \tag{3.21}$$

with $p_c(s_{10\%})$ [M/(L T^2)] being the capillary pressure at a 10% threshold saturation $s_{10\%} = s_{b,r} + 0.1(1.0 - s_{b,r})$, and the entry pressure p_e [M/(L T^2)] being the capillary pressure at a saturation of $s_b = 1.0$. In our simplified model for the pseudo-residual saturation, we assume that within the CTZ the brine phase has reached vertical equilibrium. In the following, the gas-phase plume height h in the case of capillary pressure

always excludes the CTZ from the full plume height h_{tot}, which is defined as the region with non-zero saturation of gas phase (see figure 3.1 for a reference to h_{tot}). Following this, the gas-phase plume height h is:

$$h = \begin{cases} h_{\mathrm{tot}} - CTZ & \text{for } h_{\mathrm{tot}} > CTZ, \\ 0 & \text{for } h_{\mathrm{tot}} <= CTZ. \end{cases} \tag{3.22}$$

During a time step Δt the brine phase drains out of the plume, which leads to a decrease of the plume height h_i and a decrease of the pseudo-residual saturation inside the plume. Because of the nonlinear relative permeability functions, gravity drainage in the vertical direction would typically lead to the formation of a shock followed by a rarefaction wave. For simplicity, we assume a constant pseudo-residual saturation $s^*_{b,r,i}$ inside the plume during Δt.

The Darcy velocity of brine phase draining out of the plume can be approximated based on the total Darcy velocity $\boldsymbol{u}_{\mathrm{tot}} = \boldsymbol{u}_b + \boldsymbol{u}_g$ and fractional flow function $f_b = \lambda_b/(\lambda_b + \lambda_g)$ [-] as:

$$\boldsymbol{u}_b = f_b \boldsymbol{u}_{\mathrm{tot}} + \lambda_g f_b k(g \nabla z(\varrho_g - \varrho_b) + \nabla p_c). \tag{3.23}$$

If a one-dimensional vertical column is considered that is closed at the top and the bottom, the total Darcy velocity u_{tot} equals zero. This implies countercurrent flow where the gas phase moves from the bottom to the top and the brine phase from the top to the bottom. Thus, the Darcy velocity of the brine phase out of the plume is given as:

$$u_{b,z} = \lambda_g f_b k \left(g(\varrho_b - \varrho_g) + \frac{\partial p_c}{\partial z} \right). \tag{3.24}$$

When capillary forces are neglected, we have the following approximation of the Darcy velocity for the segregation process:

$$u_{b,z} \approx \lambda_g f_b k g(\varrho_b - \varrho_g). \tag{3.25}$$

With the assumption of a constant pseudo-residual saturation during Δt, the gas phase mobility λ_g and the fractional flow function f_b are evaluated based on the pseudo-residual saturation $s^*_{b,r,i}$. The updated plume height h_{i+1} follows as:

$$h_{i+1} = h_i - \frac{u_{b,z} \Delta t}{\phi(1 - s^*_{b,r,i})}. \tag{3.26}$$

The mass balance for the brine phase inside the column is:

$$(H - h_i)\phi + h_i \phi s^*_{b,r,i} = (H - h_{i+1})\phi + h_{i+1}\phi s^*_{b,r,i+1}. \tag{3.27}$$

Finally, the updated pseudo-residual saturation $s^*_{b,r,i+1}$ can be obtained by rearranging (3.27) and inserting (3.26):

$$s^*_{b,r,i+1} = \frac{h_i \phi s^*_{b,r,i} - \frac{u_{b,z}\Delta t}{(1-s^*_{b,r,i})}}{h_i \phi - \frac{u_{b,z}\Delta t}{(1-s^*_{b,r,i})}}. \tag{3.28}$$

The brine phase saturation is assumed to be constant within the plume during vertical drainage. This leads to faster drainage because the drainage velocity decreases with saturation. The explicit calculation of the pseudo-residual saturation therefore requires a time step restriction for the segregation process. The updated pseudo-residual saturation $s^*_{b,r,i+1}$ cannot be smaller than the ultimate residual saturation $s_{b,r}$. Following this, the time step is limited due to the explicit calculation of the pseudo-residual saturation by:

$$\Delta t \leq \frac{h_i \phi \left(s^*_{b,r,i} - s_{b,r}\right)\left(1 - s^*_{b,r,i}\right)}{u_{b,z}\left(1 - s_{b,r}\right)}. \tag{3.29}$$

It is expected that the time-step limitation due to the pseudo-residual saturation update plays a role mostly during early times of the simulation. In the beginning of the segregation process, the velocities in the vertical direction will be large and the time stepping will be limited by (3.29). With time, the segregation process slows down as the brine phase saturation inside the plume decreases. Accordingly, for later times the CFL-criterion from the coarse-scale simulation (horizontal flow) will be more restrictive.

3.3.3 Global and local pseudo-VE model

The pseudo-residual brine phase saturation can either be determined for the entire plume (referred to as global pseudo-VE model) or for each vertical column inside the plume separately (referred to as local pseudo-VE model). For the global pseudo-VE model, a total drainage flux out of the plume is computed, which leads to a single value for the pseudo-residual saturation that is valid for the entire plume. For the local pseudo-VE model, we calculate the drainage flux out of each vertical column in the plume, leading to a separate pseudo-residual saturation for each column.

In the *global pseudo-VE model* we consider an averaged plume during the drainage calculation on the fine scale. The entire plume height is averaged over its horizontal length, resulting in an averaged gas phase plume height h. For the case that capillary pressure is included, the gas plume height h follows from averaging the plume height above the CTZ for all vertical columns. As a result of averaging the plume, we observed a slower decrease of the pseudo-residual saturation compared to the full multidimensional model. Accordingly, we suggest to enhance the segregation process by applying a correction to the global pseudo-VE model. This correction is based on the assumption that the averaged height of the plume and the CTZ of the entire plume is constant during the coarse-scale time step and only changes afterward due to segregation. If the plume does not advance in one time step, this implies that gas phase entering the plume at the injection well replaces the brine phase inside the plume instead of adding to the averaged height of the plume. Such correction gives the best results based on our observations.

In the following, we present the sequence of the fine-scale calculations for the global pseudo-VE model as illustrated in figure 3.6 (a). During the coarse-scale time step the averaged coarse-scale saturation inside the columns of the plume changes from $S_{b,i}$ to $S_{b,i+1}$. After the coarse-scale time step, the correction step leads to an update of the pseudo-residual saturation, so that $h'_{i+1} = h_i$:

$$s^{*'}_{b,r,i+1} = s^{*}_{b,r,i} + \frac{(S_{b,i+1} - S_{b,i})H}{(H - h_i)}. \tag{3.30}$$

Following this, gravity drainage of the brine phase is computed based on (3.28), with the adjusted gas plume height h_i and the adjusted pseudo-residual saturation $s^{*'}_{b,r,i+1}$. This leads to the final pseudo-residual saturation:

$$s^{*}_{b,r,i+1} = \frac{h_i \phi s^{*'}_{b,r,i+1} - \frac{u_{b,z}\Delta t}{(1-s^{*'}_{b,r,i+1})}}{h_i \phi - \frac{u_{b,z}\Delta t}{(1-s^{*'}_{b,r,i+1})}}, \tag{3.31}$$

with the flux of the brine phase draining out of the plume based on $s^{*}_{b,r,i}$.

In the *local pseudo-VE model*, the pseudo-residual saturation is updated for each vertical grid column, without averaging the gas plume height. Differences in the plume height along the horizontal direction are thus directly included by considering each column separately and the correction of the gas plume height due to effects of averaging are not

necessary. The sequence of the calculation for the local pseudo-VE model is illustrated in figure 3.6 (b). The drainage flux is calculated using equation (3.28), with the plume height h'_{i+1} and a flux of the brine phase draining out of the plume that is based on $s^*_{b,r,i}$ as before. This results in an update for the pseudo-residual saturation in each column:

$$s^*_{b,r,i+1} = \frac{h'_{i+1}\phi s^*_{b,r,i} - \frac{u_{b,z}\Delta t}{(1-s^*_{b,r,i})}}{h'_{i+1}\phi - \frac{u_{b,z}\Delta t}{(1-s^*_{b,r,i})}}. \tag{3.32}$$

In contrast to the global pseudo-VE model, additional considerations need to be taken into account for columns that have not been entered by the plume previously and thus have an unknown initial pseudo-residual saturation. These columns get assigned an initial pseudo-residual saturation that is equal to the average pseudo-residual saturation over all columns inside the plume. We consider the average pseudo-residual saturation in the plume a characteristic value for the system. Using it as the initial pseudo-residual saturation for the leading edge gives best results in our simulations. This is also done as a correction for a column when the time step restriction (3.29) is violated.

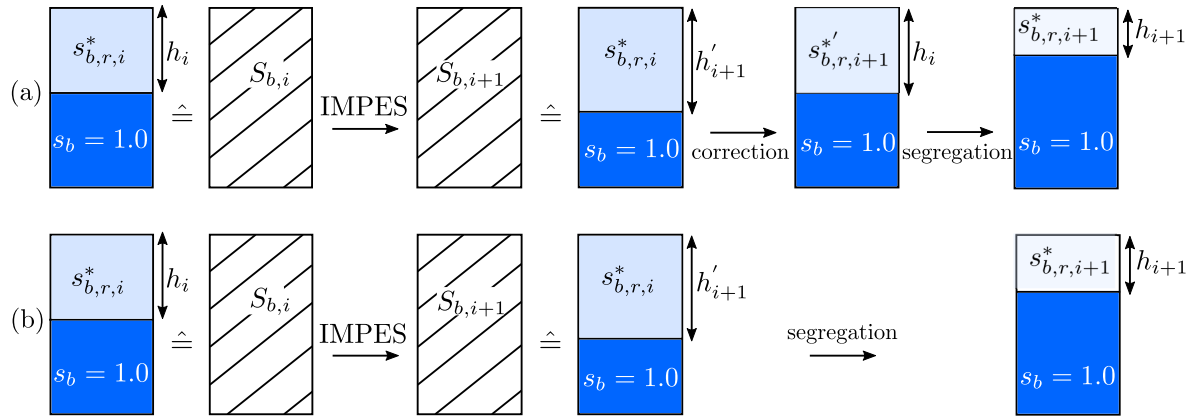

Figure 3.6: Sequence of calculation of the pseudo-residual brine phase saturation. (a) Global pseudo-VE model, (b) local pseudo-VE model. Adapted from Becker et al. [2017] with permission from John Wiley & Sons, copyright 2017.

3.4 Results and discussion

We show accuracy, robustness and efficiency for both pseudo-VE models by comparing the solutions against a conventional VE model and a full multidimensional model. The pseudo-VE models, the conventional VE model and the full multidimensional model

are all implemented in DuMu^{x} [Flemisch et al., 2011, Koch et al., 2020], allowing for a comparison of the different methods within the same software framework. The code to produce the results presented here can be obtained from https://git.iws.uni-stuttgart.de/dumux-pub/Becker2017a.git.

We design 15 base test cases (see table 3.1) of gas injection into an aquifer filled with brine to analyze:

- dynamic migration of the gas front with the change of the inflow rate,
- anisotropy of the aquifer and influence on the segregation process,
- influence of capillarity and especially entry pressure,
- behavior for different viscosity and density ratios,

for different realistic aquifer parameters. We show the influence of the power-law nonlinearity of the relative permeability function by applying three different relative permeability-saturation relationships to every base test case. This leads to 45 different cases in total. The three relative permeability functions that we use are power functions with exponent 2 and 5 and a Brooks-Corey relationship with $\lambda = 2$, as shown in figure 3.3. The Brooks-Corey relationship with the chosen parameter $\lambda = 2$ results in a relative permeability function for the gas phase that is similar to the power law with an exponent 2. For the brine phase this Brooks-Corey relationship results in a function that is close to a case of exponent 5. We consider the Brooks-Corey relationship a mixed case in terms of power-law nonlinearity of the relative permeability functions.

For simplicity, we solve the injection scenarios in two dimensions (horizontal and vertical). However, this is not a necessity for the newly developed pseudo-VE algorithm. In each test case we inject supercritical CO_2 (supercritical CH_4 in case 15) over the entire depth of one side of a two-dimensional homogeneous domain whose pore space is filled with brine. The other side is open for flow (Dirichlet boundary condition) and sufficiently far away from the injection that no gas phase crosses the boundary. On the open side we fix the brine phase saturation to $s_b = 1.0$ and prescribe a hydrostatic distribution of the brine phase pressure p_b, starting with $1.0 \times 10^7\,\mathrm{Pa}$ at the top. The top and bottom of the domain are closed. We assume a density of CO_2 of $710\,\mathrm{kg/m^3}$ and a viscosity of CO_2 of $4.25 \times 10^{-5}\,\mathrm{Pa\ s}$. For case 15 we assume a density of CH_4 of $59.2\,\mathrm{kg/m^3}$ and a viscosity of CH_4 of $1.202 \times 10^{-5}\,\mathrm{Pa\ s}$. The density of the brine

Table 3.1: Parameter combinations considered in the simulations.

cases	porosity [-]	permeability horizontal [mD]	permeability vertical [mD]	B.C. λ for p_c [-]	entry pressure [Pa]	inflow rate [kg/(s m)]	aquifer height [m]
1	0.15	100	100	2	1×10^4	7.1×10^{-3}	50
2	0.15	100	100	2	5×10^4	7.1×10^{-3}	50
3	0.15	100	100	2	1.5×10^4	7.1×10^{-3}	50
4	0.15	66.6	66.6	2	1×10^4	7.1×10^{-3}	50
5	0.15	1000	1000	2	1×10^4	7.1×10^{-3}	50
6	0.15	100	100	2	1×10^4	2.37×10^{-3}	50
7	0.15	100	100	2	1×10^4	8.9×10^{-3}	50
8	0.2	100	100	2	1×10^4	7.1×10^{-3}	50
9	0.3	100	100	2	1×10^4	7.1×10^{-3}	50
10	0.15	100	100	2	1×10^4	7.1×10^{-3}	30
11	0.15	100	100	2	1×10^4	7.1×10^{-3}	60
12	0.15	100	100	1.5	1×10^4	7.1×10^{-3}	50
13	0.15	100	100	2.5	1×10^4	7.1×10^{-3}	50
14	0.15	50	100	2.5	1×10^4	7.1×10^{-3}	50
15	0.15	100	100	2.5	3×10^4	7.5×10^{-4}	50

phase is assumed to be 991 kg/m^3 and the viscosity of the brine phase 5.23×10^{-4} Pa s. The residual saturations of both phases are assumed to be zero. The injection rates are shown in table 3.1. For most test cases (cases 1-5 and 8-14), the injection rate corresponds to an injection of 0.1 Mt CO_2 per year through a 500 m horizontal well. We increase this rate by 25 % and decrease it by 66 % for a variation in injection rate. The injection rate of CH_4 is adjusted according to the lower density of CH_4 to yield the same injected volume as for CO_2.

We use a full multidimensional model as a reference to compare with our pseudo-VE models. We performed a grid convergence test to ensure a converged solution on our two-dimensional grid. Based on that, a resolution of the grid of 2 m in the horizontal direction and 0.125 m in the vertical direction was chosen to generate the two-dimensional reference solutions of all test cases in table 3.1 with the relative permeability-saturation relationships from figure 3.3. Following that, all test cases were simulated with the three VE models: the global pseudo-VE model, the local pseudo-VE model and the conventional VE model. The same resolution in the horizontal direction was chosen as for the reference solutions. For all our test cases, the two pseudo-VE models are similar to the conventional VE model in terms of computational time, and three orders of magnitude

faster than the reference model.

We note that the time step restriction due to vertical segregation as in equation (3.29) has been in none of the cases for the global pseudo-VE model more restrictive than the CFL-condition applied for the coarse-scale simulation. In the global pseudo-VE model the columns with small plume heights are averaged out along with the saturation inside the plume, leading to less restrictive time steps. A more restrictive time step due to the explicit calculation of the pseudo-residual saturation has only been observed for the local pseudo-VE model. The correction resulting from that has been rarely necessary and has occured only for the columns near the leading edge of the plume when the plume height was very small there ($\approx$ 100 times smaller than the average height of the entire plume). However, small oscillations that can be observed in the saturation inside the plume of the local pseudo-VE model are attributed to the correction and initialization of columns at the leading edge of the plume. This can lead to slightly different plume heights and initial pseudo-residual saturations inside the columns at the leading edge of the plume at the start of segregation.

The presentation and analysis of the results is structured in three parts: 3.4.1 is concerned with the plume extent at later times, 3.4.2 investigates the plume extent at earlier times and in 3.4.3 we analyze the gas phase distribution in the domain for exemplary test cases.

3.4.1 Comparison of horizontal plume extent at $\mathrm{t} = 10\mathrm{t}_{\mathrm{seg}}$

We take the horizontal plume extent as an indicator for accuracy. The horizontal plume extent refers to the horizontal distance from the injection point to the leading edge of the plume. The leading edge is defined as the location closest to the injection where the reconstructed gas phase saturation is smaller than 1.0×10^{-6}. The comparison is done after a simulated time of $10t_{\mathrm{seg}}$, with the segregation time t_{seg} [T] calculated after Nordbotten and Dahle [2011]. The segregation time can be used to estimate the time after which VE models are applicable and can be written as:

$$t_{\mathrm{seg}} = \frac{H\phi(1 - s_{b,r})\mu_b}{k_{r,b}k_z g(\varrho_b - \varrho_g)}, \tag{3.33}$$

where k_z represents the vertical permeability [L^2]. Practically, we choose the characteristic value for the relative permeability of the brine phase to be 1, which leads to a smallest possible segregation time.

The horizontal plume extent for all VE models is plotted against the full multidimensional reference solutions in figure 3.7. Both pseudo-VE models lead to a very good

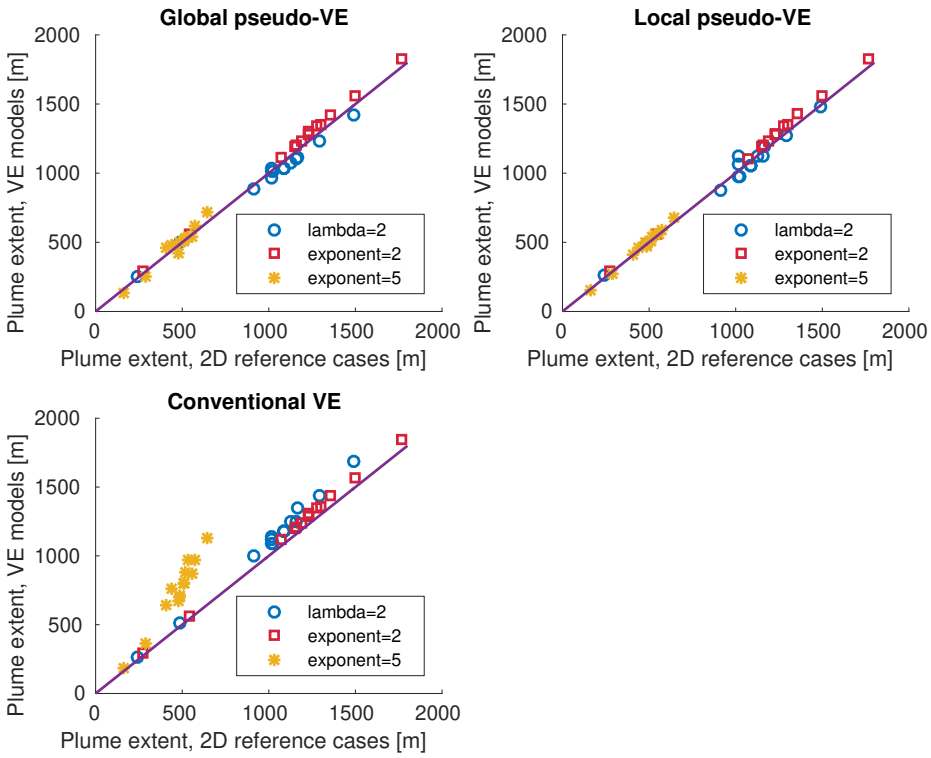

Figure 3.7: Horizontal plume extent for global pseudo-VE model, local pseudo-VE model and conventional VE model over horizontal plume extent for full multidimensional reference. A perfect match to the reference solution is the purple line, dots above this line indicate overestimation of the horizontal plume extent, dots below this line indicate underestimation of the horizontal plume extent. The colors indicate the relative permeability-saturation relationship; Blue: Brooks-Corey law with $\lambda = 2$ (mixed case), red: power function with exponent 2 (low nonlinearity), yellow: power function with exponent 5 (high nonlinearity). Reprinted from Becker et al. [2017] with permission from John Wiley & Sons, copyright 2017.

estimation of the horizontal plume extent. They compare well with the full multidimensional model for all cases, independent of the power-law nonlinearity of the relative permeability functions. Relative permeability functions with large exponents as well as the Brooks-Corey relationship with a parameter $\lambda = 2$ can be handled.

As expected, due to the nonlinear relative permeability functions used, the results show an overestimation of the horizontal plume extent for the conventional VE model for almost all test cases, in particular for the relative permeability cases with large exponents. This is because the conventional VE model does not reflect the slow gravity drainage since it assumes gravity segregation of both phases from the start. Especially in the case of relative permeability functions with large exponents, assuming gravity segregation from the beginning of simulation results in a higher coarse-scale relative permeability and consequently a much faster propagation of the front. The conventional VE model appears to give good results for cases with a large permeability or a low injection rate as well. This is mostly due to the fact that the horizontal plume extent for these cases is smaller, leading to the dots in the figure to be closer to the reference line than for the other cases. However, the relative error (difference in horizontal plume extent in percentage of horizontal plume extent of the reference simulation) stays in the same range as for all other cases.

For relative permeability functions with low exponents the results of the pseudo-VE models recover the results of the conventional VE model, while all of them compare well with the results from the full multidimensional model. In cases with relative permeability functions with low exponents the assumption of instant segregation can be considered as more valid. Here, both phases segregate faster because relative permeability does not reach very low values for medium brine phase saturations. This is reflected in the pseudo-VE models by a faster segregation of the two phases, leading to similar results as for the conventional VE model. Additionally, for linear relative permeability functions, the coarse-scale relative permeability does not depend on the fine-scale saturation profile at all. Thus, a relative permeability function with low exponent (close to linear) results in less dependency of the coarse-scale relative permeability on a correct reconstruction of the saturation profile in the vertical direction. Accordingly, for these cases all VE models show generally satisfying agreement with the reference model.

The results indicate that including the segregation process in a simplified way (pseudo-VE model) gives saturation profiles in the vertical direction that are closer to the reference solution and results in a more correct coarse-scale relative permeability. Consequently, both pseudo-VE models greatly improve the results compared to the conventional VE model and thereby extend the applicability of VE models.

We also measure the difference between the three VE models and the reference solution

using the L2-norm of the difference of the horizontal extent, see figure 3.8. The L2-norm is calculated as the square root of the sum of squares of differences in horizontal plume extent between the reference solutions and the three VE models. For the mixed cases and the cases with relative permeability functions with large exponents, the L2-norm for both pseudo-VE models is significantly lower than for the conventional VE model. Only for the cases with low exponents the L2-norm is similar for all VE models. The global pseudo-VE model always shows a slightly higher L2-norm than the local pseudo-VE model, which is still significantly lower than for the conventional VE model.

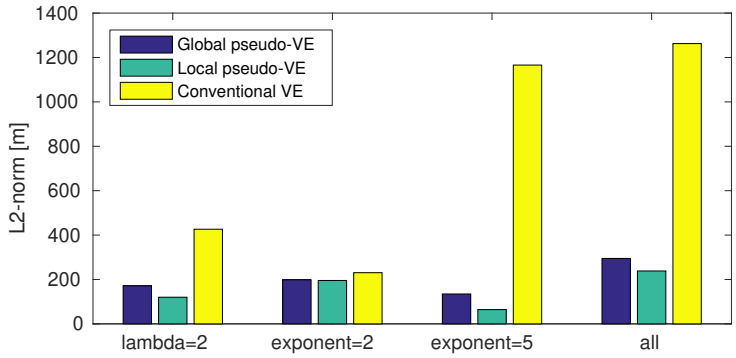

Figure 3.8: L2-norm for VE models for all test cases. The L2-norm is calculated as the square root of the sum of squares of differences in horizontal plume extent between the reference solution and the VE models. Reprinted from Becker et al. [2017] with permission from John Wiley & Sons, copyright 2017.

3.4.2 Comparison of horizontal plume extent at $t < 10t_{seg}$

We analyze the horizontal plume extent for times closer to the estimated segregation time. This is done using case 1 and case 5 (large-permeability case with $k = 1000$ mD) as examples, to show the influence of permeability. The relative permeability function is given by a Brooks-Corey relationship with a parameter $\lambda = 2$ (mixed case) and a power function with exponent 5 (highly nonlinear). The relative error is calculated as the difference between the horizontal plume extent resulting from the VE models and the reference solution, and given in percentage of the horizontal plume extent of the reference solution. The relative error is plotted over time normalized by the segregation time t_{seg} in figure 3.9.

The global pseudo-VE model shows a less good agreement for early times. However, the

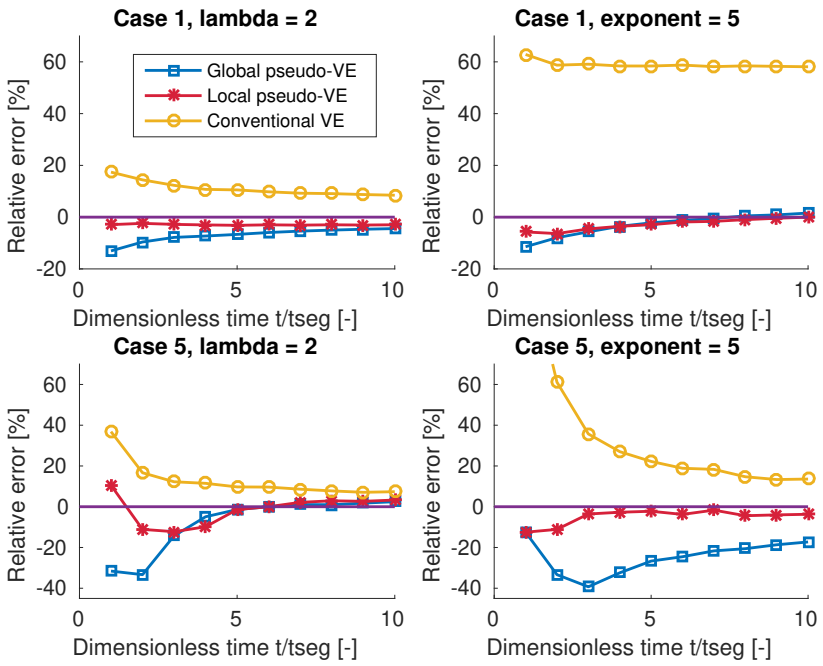

Figure 3.9: Relative error over dimensionless simulation time for global pseudo-VE model, local pseudo-VE model and conventional VE model. First row: case 1, second row: case 5 (large-permeability case). First column: relative permeability function with Brooks-Corey $\lambda = 2$, second column: relative permeability function with exponent 5 (highly nonlinear). The relative error is calculated as the difference to the horizontal plume extent of the reference solution and given as the percentage of the horizontal plume extent of the reference solution. Reprinted from Becker et al. [2017] with permission from John Wiley & Sons, copyright 2017.

results improve after approximately $5t_{\text{seg}}$ for most cases, for both permeability functions. This is attributed to the global pseudo-VE model being a very simple modification of the conventional VE model. It gives stable results but it neglects variations of the saturation inside the plume in the horizontal as well as vertical direction. During the fine-scale calculations we assume that the plume height is approximately the same everywhere to be able to calculate the drainage using an averaged plume height. This assumption does not hold for earlier simulation times when the horizontal plume shape has not developed yet. Consequently, this leads to the observed discrepancies between the reference solution and the global pseudo-VE model in earlier times and to a slower convergence toward the reference solution over time. The global pseudo-VE model manages to capture the horizontal plume extent well for later times, except for cases with large permeability and a relative permeability function with large exponent, where

the horizontal plume extent is underestimated. This indicates that the correction of the global pseudo-VE model does not reflect the local processes equally well for all cases. However, the relative error in this case is in the range of the conventional VE model.

All results for the local pseudo-VE model show good agreement with the reference solution over all times, even times close to the segregation time. This holds for both the Brooks-Corey relative permeability function and the highly nonlinear relative permeability function. The local pseudo-VE model accounts for vertical fluxes by the explicit calculation of the pseudo-residual saturation in each single grid column. This way, the local pseudo-VE model includes variations of the saturation inside the plume along the horizontal direction. This is especially relevant for earlier times, during which the gas plume exhibits large variations of the plume height along the horizontal direction, leading to different saturation values inside the plume. Consequently, the local pseudo-VE model leads to a very good approximation of the horizontal plume extent, even for relative permeability functions with large exponents and earlier times that are closer to the segregation time.

The conventional VE model overestimates the horizontal plume extent in all cases, especially for cases with relative permeability functions with large exponents. The solution of the conventional VE model seems to approach the reference solution very slowly in general. This is again because instant gravity segregation is assumed and leads to incorrect saturation profiles in the vertical direction.

3.4.3 Comparison of gas phase distribution

We plot exemplary saturation distributions for case 1 and case 5 (large-permeability case with $k = 1000$ mD), using a highly nonlinear relative permeability function (exponent 5). The results for the reference simulation and all VE models are shown in figure 3.10 and 3.11 for three different time steps.

Case 1 shows that both the local pseudo-VE model and the global pseudo-VE model agree well with the reference solution over time. The variations in plume height along the horizontal direction are represented well. However, one can see a difference in saturation distribution within the plume. The reference solution shows a clear vertical gradient in saturation which is not represented by the VE models. As expected, the

conventional VE model and the global pseudo-VE model have a uniform saturation inside the entire plume. The local pseudo-VE model shows variations along the horizontal direction, with lower saturation values around the injection area. The conventional VE model results in an incorrect plume shape with a very different saturation inside the plume compared to the reference solution. The plume is thinner, which leads to an overestimation of the horizontal plume extent.

Case 5 shows again a good agreement between reference solution and local pseudo-VE model. The global pseudo-VE model does not represent the plume height along the horizontal direction correctly for earlier times, which leads to an underestimation of the horizontal plume extent also for later times. The conventional VE model again shows an overall thinner plume and overestimation of the horizontal plume extent.

Compared to the multiscale dynamic reconstruction model in Guo et al. [2014] which produces results with a very high accuracy also in the vertical direction, both pseudo-VE models show a more simplified saturation profile in the vertical direction. This might have an impact especially for early simulation times and lead to less accurate results by the pseudo-VE models in comparison. Particularly the variations in the saturation profile in the vertical direction cannot be represented by the pseudo-VE models. In terms of computational effort, the multiscale dynamic reconstruction model relies on vertical fine-scale one-dimensional simulations inside each column. This requires gridding for the fine-scale simulation and storage of the data for the determination of the coarse-scale parameters by integration, which results in a more complex implementation and higher computational cost. The computational effort for the pseudo-VE models are similar to those for the conventional VE model, resulting in a faster computation compared to the multiscale dynamic reconstruction model. Thus, the pseudo-VE models can be seen as intermediate models between the conventional VE model and the multiscale dynamic reconstruction model in Guo et al. [2014]. The decision of which model to take has to be done by weighing accuracy against computational speed based on the exact question of interest that is to be answered by the model.

3.5 Conclusion

In this chapter a pseudo-VE model was developed by casting it into a multiscale framework for VE models and treating the segregation process on the fine scale explicitly without having to rely on the VE assumption. The newly developed pseudo-VE model assumes a pseudo-segregated state with a pseudo-residual brine phase saturation higher than the ultimate brine phase saturation inside the plume, with the pseudo-residual saturation being continuously updated during the simulation. The pseudo-residual saturation can either be determined for the entire plume or for each column separately, leading to two versions of the pseudo-VE model.

The pseudo-VE models showed better (or equal) accuracy in predicting the gas plume extent compared to the conventional VE model throughout the range of aquifer parameters in the injection test scenarios, in particular for relative permeability functions with large exponents. The local pseudo-VE model gives significantly improved results especially for earlier times of the simulation. The pseudo-VE models extend the applicability of VE models to cases with relative permeability functions with large exponents and shorter time scales, while fully maintaining the computational benefit of conventional VE models. As such, pseudo-VE models can provide a very efficient computational tool for dealing with practical cases of underground gas storage in which large domains, long simulation times and parameter uncertainty are major challenges.

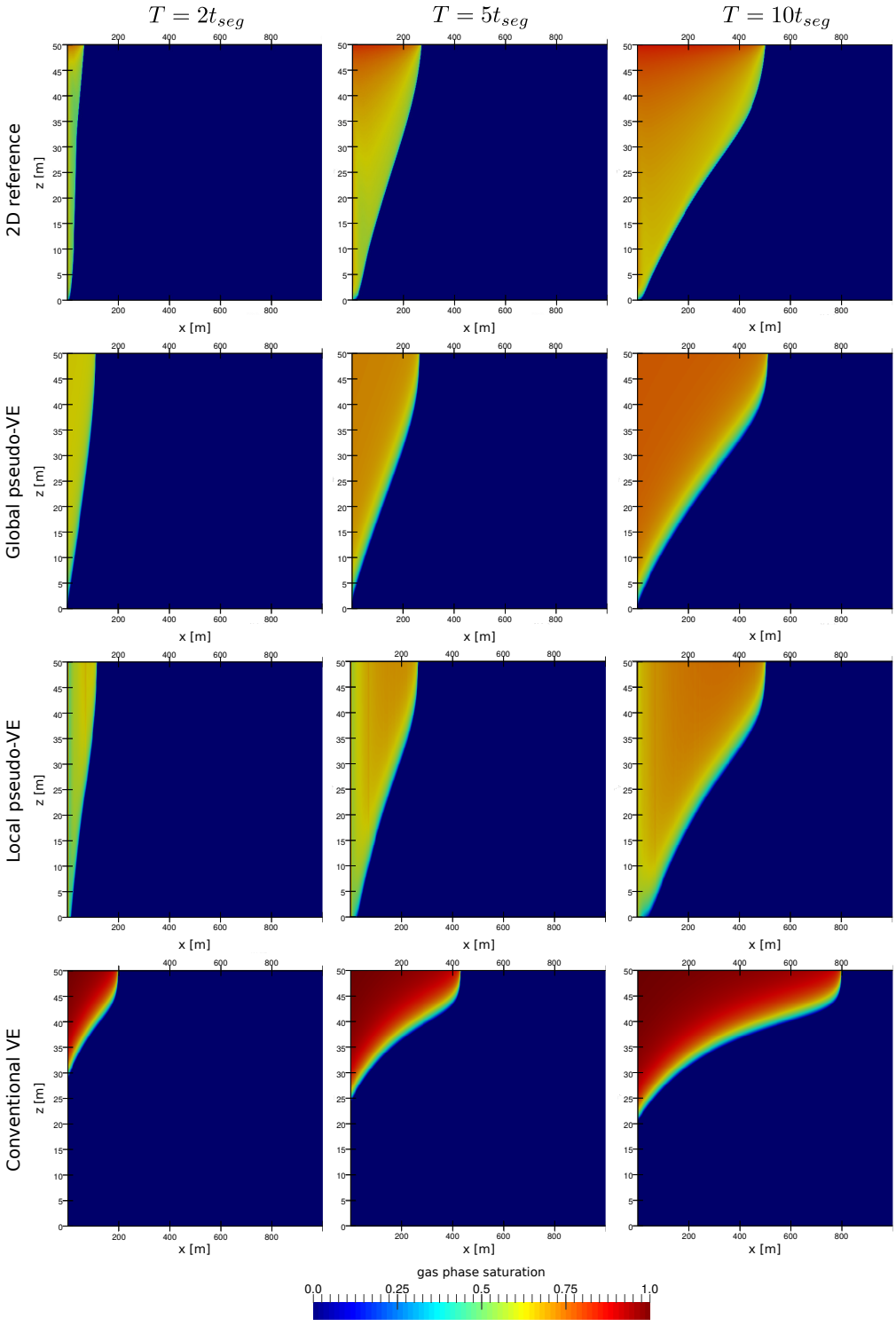

Figure 3.10: Gas phase distribution for 2D reference, global pseudo-VE model, local pseudo-VE model and conventional VE model for case 1 with highly nonlinear relative permeability function (exponent 5) for different time steps: $2t_{\text{seg}}$, $5t_{\text{seg}}$, $10t_{\text{seg}}$. Reprinted from Becker et al. [2017] with permission from John Wiley & Sons, copyright 2017.

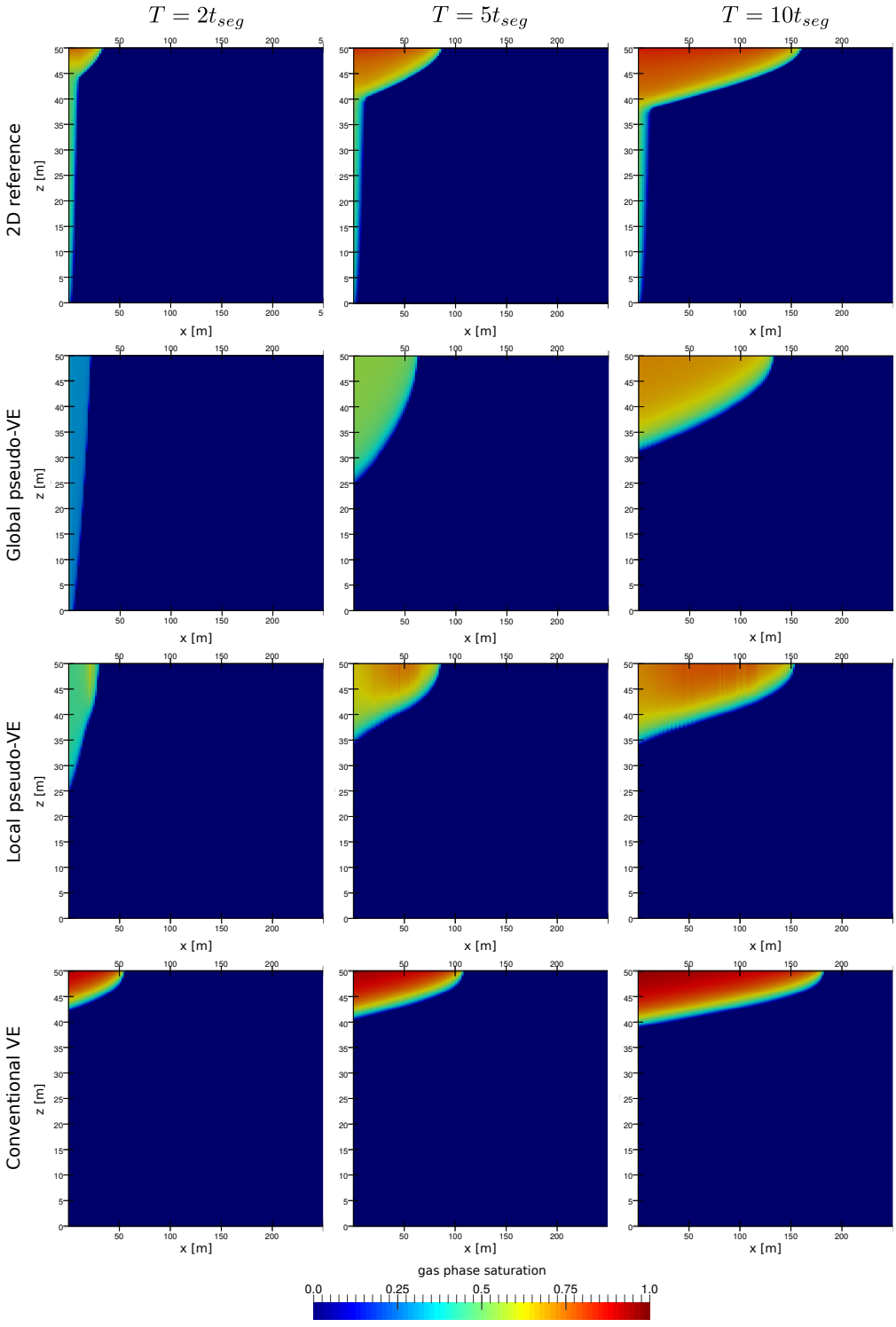

Figure 3.11: Gas phase distribution for 2D reference, global pseudo-VE model, local pseudo-VE model and conventional VE model for case 5 (large permeability $k = 1000$ mD) with highly nonlinear relative permeability function (exponent 5) for different time steps: $2t_{\text{seg}}$, $5t_{\text{seg}}$, $10t_{\text{seg}}$. Reprinted from Becker et al. [2017] with permission from John Wiley & Sons, copyright 2017.

4 Multiphysics model for immiscible two-phase flow [2]

The most efficient model at a specific time during the simulation or at a specific location in the domain can be used by coupling models of different complexity (multiphysics or hybrid model). Multiphysics models are robust and computationally efficient on domains with varying complexity because they can adaptively match model complexity to domain/process complexity for different parts of the domain, which significantly reduces computational costs. As such, they are perfectly suited for the challenges associated with modeling energy storage in the underground. The storage gas injected into a saline aquifer leads to a complex two-phase flow system, in which gas phase moves laterally outward from the injection point and at the same time upward due to buoyancy. The overall spatial extent of the gas plume is important in general, but a much more detailed flow field is desired near the well than farther away, e.g., for well management. In addition, gas phase near the well migrates in the vertical as well as horizontal direction during injection and extraction, while farther away from the well hydrostatic pressure profiles may have developed in the vertical direction. At these larger distances, the gas phase may be considered to be in vertical equilibrium with the brine phase, as long as the domain is homogeneous. In subdomains where the VE assumption is valid, VE models give accurate solutions at significantly lower computational costs. However, in all subdomains where the VE assumption is not valid, using a VE model gives inaccurate results. Therefore, a multiphysics framework that allows coupling of spatially non-overlapping subdomains and adaptively selects subdomains during the simulation run is developed in this chapter. The multiphysics model couples a full multidimensional two-phase model to a VE model. The VE model assumes that vertical flow is negligible and thus represents a model of lower complexity. The VE model is applied in regions of the domain where the vertical equilibrium assumption

[2] Large parts of this chapter are taken and partly modified from Becker et al. [2018]

holds, while the full multidimensional model is applied in the rest of the domain. We design a criterion to adaptively identify the subdomains where the VE model can be applied during the simulation. For the coupling of the subdomains, we exploit the fact that all fine-scale variables of the VE model can be reconstructed at every point in the vertical direction. This leads to the introduction of subcells in the VE grid columns at the interface. We achieve the coupling through the fluxes across the subdomain boundaries from the full multidimensional cells to the subcells. The resulting system is solved monolithically.

This chapter is based on the work published in Becker et al. [2018] and structured as follows: First, an overview of multiphysics models for multiphase flow in porous media is given in section 4.1. Then, section 4.2 presents the coupling strategy for the multiphysics model. Following that, criteria for vertical equilibrium are developed and analyzed, and the adaptive algoritm is presented in section 4.3. Lastly, section 4.4 shows the applicability of the developed approach on a test case of gas injection in an aquifer and gives recommendations for choosing the optimal threshold parameter for the adaptive algorithm.

4.1 Multiphysics models

Developing and analyzing multiphysics models is an ongoing, vibrant field of research, spanning the entire community of hydrology and computational physics. Here, we focus on multiphysics models for multiphase flow in porous media. An overview of multiphysics models for multiphase flow can be found in Wheeler and Peszyńska [2002] and for different coupling strategies in Helmig et al. [2013]. Models which couple the transition from one submodel to another in time are distinguished from models which couple in space. Furthermore, coupled models in space can be overlapping within one domain, e.g., coupling of different processes like flow and geomechanics (see White et al. [2016] for a comprehensive framework) or coupling of different scales (see, e.g., Kippe et al. [2008] for a review of multiscale methods for elliptic problems in porous media flow). They can also be coupled in separate subdomains with shared interfaces, e.g., models for flow inside discrete lower-dimensional fractures embedded in the porous matrix (see, e.g., Singhal and Gupta [2010], Sahimi [2011] for a comprehensive review) or

compartments with different models coupled in one domain. The models in those coupled compartments can be of different complexity, e.g., a black-oil model, a two-phase flow model and a single-phase flow model [Peszyńska et al., 2000], where each model is applied in a different subregion of the domain depending on the number and type of fluids present. Another example of coupling compartments is a multiscale model coupling a Darcy-scale and a pore-scale model [Tomin and Lunati, 2013]. This framework allows considering pore-scale fluxes only in some regions of the domain, while Darcy fluxes are used in the rest of the domain. Coupling subdomains with different models often involves the so-called mortar methods [Bernardi et al., 1994, Belgacem, 1999], that use Lagrange multipliers at the interfaces to realize the coupling. Another group of coupling schemes exploits similarities between the individual mathematical equations of the subdomains to couple models without requiring specifically constructed coupling conditions. One example of such a coupled model was developed by Fritz et al. [2012]. This multiphysics model considers two-phase multicomponent flow only where both phases are present and solves a simpler one-phase model that is a degenerate version of the two-phase model everywhere else. The approach was extended to non-isothermal flow by Faigle et al. [2015], using a subdomain in which non-isothermal effects are accounted for and a subdomain where simpler, isothermal equations are solved. The method is shown to be accurate and significantly reduces computational cost. Another example is presented by Guo et al. [2016a], where multiscale vertically integrated models that can capture vertical two-phase flow dynamics are coupled for gas migration in a layered geological formation. The coarse scale consists of several horizontal layers that are vertically integrated. They are coupled together by formulating a new coarse-scale pressure equation that computes the vertical fluxes between the layers. In each coarse-scale layer, horizontal and vertical fluxes are determined on the fine scale. The transport calculation on the fine scale is coupled to the coarse scale sequentially. A multiresolution coupled vertical equilibrium model for fast flexible simulation of CO_2 storage is presented by [Møyner and Nilsen, 2019]. This framework allows the coupling of a VE model and a full multidimensional model, while the subdomains need to be determined *a priori*.

4.2 Coupling strategy

We develop a multiphysics model that couples a VE model for immiscible, incompressible two-phase flow (3.6, 3.7) to a full multidimensional model for immiscible, incompressible two-phase flow (2.12, 2.10). In this section we present the coupling scheme to couple the two models at the interfaces of the subdomains. The coupling of the subdomains is implemented in a monolithic framework. We exploit similarities between the full multidimensional governing equations and the VE coarse-scale governing equations, which have the same form. They balance a storage term consisting of a porosity and the time derivative of the saturation with fluxes and a source/sink term, while the flux term is calculated with the gradient of driving forces, pressure and gravity, multiplied by a term describing flow resistance. In the case of the VE model, the quantities are depth-integrated over the height of the VE column. In the following, section 4.2.1 presents the formulation of fluxes across the subdomain interfaces and section 4.2.2 explains the computational algorithm for the coupled multiphysics model.

4.2.1 Fluxes across subdomain boundaries

We discretize space with a cell-centered finite-volume method. Figure 4.1 shows a possible configuration of grid cells with two subdomains and one shared boundary between them. In this example we consider a two-dimensional domain, where the first two grid columns are part of the full multidimensional subdomain, the third and fourth grid column are part of the VE subdomain. The black dots indicate the location of the calculation points for the primary variables. For the full multidimensional model the calculation points are located in the cell center, for the VE model at the bottom of the domain.

Fluxes between two full multidimensional cells and between two VE cells are determined using a two-point flux approximation. We require flux continuity across the subdomain boundary. For the calculation of fluxes across the subdomain boundary, the VE grid column directly adjacent to the subdomain boundary is refined into full multidimensional subcells in the vertical direction, with each subcell corresponding to a neighboring full multidimensional cell (see gray dots and dotted lines in figure 4.1). Fluxes are formulated across the interface between each full multidimensional cell and

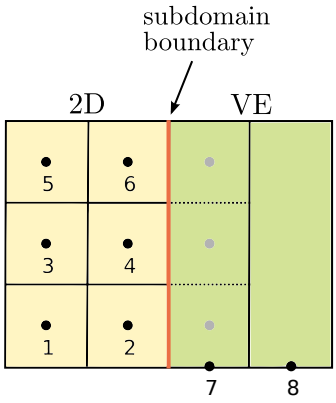

Figure 4.1: Schematic of the computational grid with subcells (dotted lines) at the interface between two subdomains. Black dots denote the calculation points of the primary variables in both subdomains. Gray dots denote the calculation points of the primary variables for subcells, which can be seen as fine-scale cells of the VE model. Reprinted from Becker et al. [2018] with permission from John Wiley & Sons, copyright 2018.

the neighboring VE subcell. For each full multidimensional cell there is only one flux across the interface to the adjacent VE subcell. The flux over the subdomain boundary to the VE cell is computed as the sum of the fluxes from the neighboring full multidimensional cells.

The total Darcy flux is:

$$\boldsymbol{u}_{\mathrm{tot}} = \boldsymbol{u}_b + \boldsymbol{u}_g = -\boldsymbol{k}\lambda_{\mathrm{tot}} \left(\nabla p_b + f_g \nabla p_{\mathrm{c}} + f_b \varrho_b g \nabla z + f_g \varrho_g g \nabla z\right). \tag{4.1}$$

In the following we exploit the fact that the primary variables at the calculation points of the VE subcells can be expressed analytically via the primary variable of the VE cell. This is because the solution in the vertical direction can be reconstructed analytically using the VE assumption in the VE subdomain. With this, the total normal Darcy flux from a full multidimensional cell denoted with superscript 'i' to a VE subcell denoted with superscript 'j'' can be constructed as:

$$\begin{aligned} u_{\mathrm{tot}}^{ij'} &= u_b^{ij'} + u_g^{ij'} \\ &= -k^{ij'} \lambda_{\mathrm{tot}}^{ij'} \left(\frac{p_b^{j'} - p_b^i}{\Delta x} + f_g^{ij'} \frac{p_c^{j'} - p_c^i}{\Delta x} + f_b^{ij'} \varrho_b g \frac{z_{j'} - z_i}{\Delta x} + f_g^{ij'} \varrho_g g \frac{z_{j'} - z_i}{\Delta x} \right), \end{aligned} \tag{4.2}$$

where $p_b^{j'}$ is the reconstructed pressure at the z-coordinate of the calculation point of the VE subcell, Δx is the distance between the centers of the cells i and j', and $z_{j'}$ is the z-coordinate of the calculation point of the VE subcell. The reconstructed pressure $p_b^{j'}$ is calculated for a sharp interface VE model according to equation (3.10), for a VE model with capillary transitioning zone according to equation (3.14). The reconstructed capillary pressure at the calculation point of the VE subcell is determined as:

$$p_c^{j'} = p_c(s_b^{j'}), \tag{4.3}$$

where $s_b^{j'}$ is the reconstructed brine phase saturation at the node in the middle of the subcell. The mobilites for the VE subcells are based on the brine phase saturation averaged over the subcell, $\bar{s}_b'$. We apply full upwinding for the mobilities, so that they are either taken directly from the full multidimensional cell or the reconstructed subcell in the VE column, depending on the phase potentials:

$$\lambda_\alpha^{ij'} = \begin{cases} \lambda_\alpha^i(s_b^i) & \text{if} \quad \Phi_{\alpha,ij'} > 0, \\ \lambda_\alpha^{j'}(\bar{s}_b^{j'}) & \text{if} \quad \Phi_{\alpha,ij'} < 0, \quad \alpha = b,\, g. \end{cases} \tag{4.4}$$

For $\Phi_{\alpha,ij'} = 0$, the flux is zero and the choice of mobility does not matter. The phase potentials are:

$$\Phi_{\alpha,ij'} = \frac{p_\alpha^i - p_\alpha^{j'}}{\Delta x} + \varrho_\alpha g \frac{z_{i'} - z_j}{\Delta x}, \quad \alpha = b,\, g. \tag{4.5}$$

This concept is used for all cells at the interface between the full multidimensional subdomain and the VE subdomain. The flux from a VE cell to neighboring full multidimensional cells is determined as the sum of the individual fluxes over the subdomain boundary from VE subcells to full multidimensional cells. Following this approach, all fluxes are the same as calculated from either the VE cell side or the full multidimensional cell sides.

4.2.2 Computational algorithm

The full multidimensional governing equations (2.12, 2.10) and the VE coarse-scale governing equations (3.6, 3.7), can in principle be solved fully implicitly, sequentially implicitly or sequentially with a combination of implicit and explicit schemes. Here,

we reformulate the governing equations into a pressure and a saturation equation and solve them sequentially with an IMPES algorithm. The pressure equation is solved in an implicit manner with a single computational matrix for the entire domain (multidimensional plus VE subdomains) and therefore we do not use iterations between subdomains. Specifically this means that the pressure in the different subdomains is solved simultaneously and each VE cell and each full multidimensional cell contribute one row to the pressure matrix. For cells at the subdomain interfaces the velocity is constructed as shown above with the help of the VE subcells. For VE cells at the subdomain boundary the fluxes from all neighboring cells are taken into account. Once the fluxes have been calculated from the pressure solution, the saturations are updated explicitly for each cell using the saturation equation. The corresponding saturation equation for VE cells at the subdomain interface again takes into account all fluxes from neighboring full dimensional cells and VE cells.

The saturation is lagged one time step in the IMPES algorithm, meaning the values from the last time step are used for capillary pressure and all other secondary variables that depend on the saturation. The phase fluxes are computed from the pressure field solved in the pressure step, with equation (4.2) to compute fluxes across subdomain boundaries, resulting in a mass conservative scheme.

4.3 Adaptivity

In the following, section 4.3.1 discusses general criteria for vertical equilibrium. Criteria to determine when and where to apply a VE subdomain in the multiphysics model are developed in section 4.3.2 and the behavior of these criteria is analyzed in section 4.3.3. Finally, in section 4.3.4, an algorithm that adaptively moves the boundaries between subdomains is presented.

4.3.1 VE criteria

We identify two groups of criteria that determine whether the vertical equilibrium assumption holds: one is referred to as a global criterion and the other is referred to as a local criterion. The global criterion gives an *a priori* estimate of the time after

which the vertical equilibrium assumption holds in the entire spatial domain, e.g., the segregation time (3.33). The VE model gives accurate results for time scales that are much larger than the segregation time.

The local criterion can determine if the VE assumption is valid for a specific point in time and space. This is usually an *a posteriori* criterion, which means the information is only known during runtime based on the computed solution, unlike the global criterion which can be evaluated before the solution is computed. As a result, the global criterion is typically very approximative in nature. Additionally, in a realistic geological setup, there may be regions of the model domain (e.g., near the well, local heterogeneities) where the VE assumption does not hold, even provided the simulation time is much larger than the segregation time. Around the well the fluid phases will not reach vertical equilibrium at any time, especially considering frequently alternating injection and extraction cycles. In contrast to that, vertical equilibrium may be reached locally within the plume even before the segregation time has been reached. Because the global criterion gives average information for the entire domain, it is unsuited to identify local regions where the vertical equilibrium assumption holds. We will therefore use a local criterion to determine the applicability of the VE model for each vertical grid column in the domain at every time step.

4.3.2 Local VE criteria

We develop two local criteria that can be used to determine if the brine and gas phases in a grid column have reached vertical equilibrium. For the first criterion we compare the full multidimensional profile of brine phase saturation in the vertical direction to the VE-profile that would develop if the phases were segregated and hydrostatic pressure conditions had been reached. The difference indicates how far away the two fluids are from vertical equilibrium. The approach for the second criterion is the same, except that we compare relative-permeability profiles of the brine phase. For nonlinear relative permeability functions the relative-permeability profile will differ from the saturation profile and the two local criteria will give different values. Although the saturation profile is directly linked to the state of vertical equilibrium in the column, the relative permeability profile is more relevant to the calculation of the coarse-scale relative permeability and thus applies more directly to the development of the plume.

The VE profiles are reconstructed from the total volume of gas phase inside the grid column, in the same way as the fine-scale saturation and relative permeability profiles in the VE model are constructed. We can compute the area of the differences between the

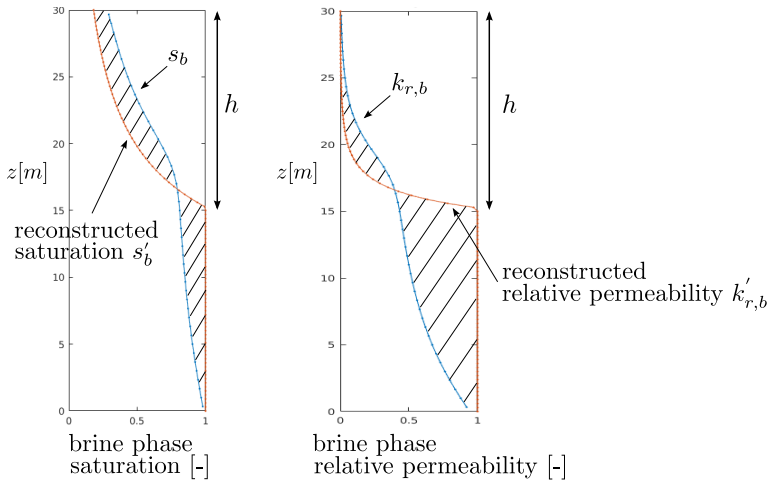

Figure 4.2: Vertical profiles in one column. Left: brine phase saturation, right: brine phase relative permeability using a Brooks-Corey relationship with pore size distribution index $\lambda = 2.0$ and entry pressure $p_e = 10^5$ Pa. The blue curve is the result of the full multidimensional solution, and the orange curve is the reconstructed profile that would develop if the fluid phases were in equilibrium. The difference between profiles is depicted as striped areas. Reprinted from Becker et al. [2018] with permission from John Wiley & Sons, copyright 2018.

profiles (see figure 4.2) and use that to develop the criteria. Specifically, we normalize the computed area with the height of the VE-profile h and define c_{sat} and c_{relPerm} as the criteria values for saturation and relative permeability, respectively:

$$c_{\text{sat}} = \frac{\int_{z_B}^{z_T} |s_b - s_b'| dz}{h}, \tag{4.6}$$

$$c_{\text{relPerm}} = \frac{\int_{z_B}^{z_T} |k_{r,b} - k_{r,b}'| dz}{h}. \tag{4.7}$$

The vertical equilibrium assumption can be considered to be valid in a grid column during a time step when the criterion value c_{crit} is smaller than a threshold value ϵ_{crit}, where the threshold is a constant value that has to be chosen by the user.

We use profiles of saturation or relative permeability to determine the state of vertical equilibrium because they show a noticeable variation between the VE subdomains and the full multidimensional subdomains. This does not require much additional compu-

tational effort as the saturation and relative permeability profiles are needed anyway to determine upscaled mobilities. We note that pressure profiles could also be used for the criteria, though we have not explored this in much depth.

4.3.3 Criteria analysis

We analyze the behavior of the two local criteria for vertical equilibrium over space and time as well as for different simulation parameters. In our two-dimensional test case we inject methane (CH_4) from the left over the entire thickness (30 m) of an initially brine-saturated domain. We use conditions which are typical for gas storage in 1000 m depth. Bottom and top are closed to flow and Dirichlet conditions are prescribed on the right-hand side with $s_b = 1.0$ and a hydrostatic distribution of the brine phase pressure p_b, starting with 1×10^7 Pa at the top. We chose our domain long enough so that the gas phase will not reach the right-hand side boundary during the simulation. We assume a density of 59.2 kg/m^3 and a viscosity of 1.202×10^{-5} Pa s for CH_4. The density of the brine phase is assumed to be 991 kg/m^3 and the viscosity of the brine phase 5.23×10^{-4} Pa s. We uniformly inject 0.0175 kg/s/m CH_4 for 240 h. The permeability is assumed to be 2000 mD and the porosity 0.2 . For relative permeability and capillary pressure we use Brooks-Corey curves with pore size distribution index $\lambda = 2$ and entry pressure $p_e = 10^5$ Pa. We use a grid resolution of 1 m in both horizontal and vertical direction, and estimate the segregation time with equation (3.33) as $t_{\text{seg}} = 48$ h.

We compute the criterion values in each numerical grid column of the two-dimensional domain and compare them in space and time, as shown in figure 4.3. We plot criterion values of both criteria over the length of the two-dimensional domain for three different times and over dimensionless time t/t_{seg} for two vertical grid columns. For our chosen injection scenarios the criterion based on relative permeability gives higher values than the saturation criterion. This is due to the strong nonlinearity of the relative permeability function. On one hand, brine held back inside the region of the gas plume contributes less to the relative permeability criterion than to the saturation criterion since the relative permeability will be almost zero for small brine phase saturations. On the other hand, small gas phase saturations below the gas plume in equilibrium lead to very large criterion values of the relative permeability criterion. This makes the relative permeability profile deviate strongly from the VE profile in the region below

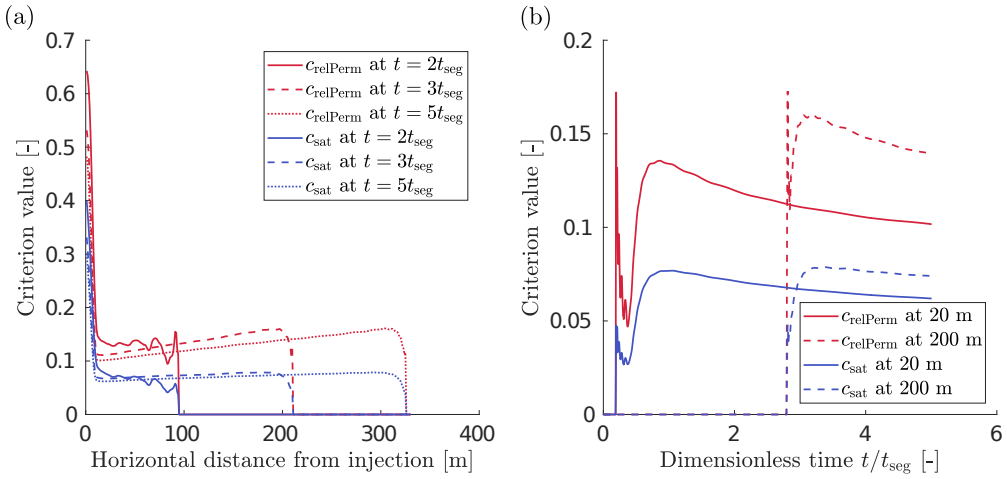

Figure 4.3: Criterion values for the VE criteria based on saturation and relative permeability, respectively. (a) Over the entire length of domain for three times: $2t_{\text{seg}}$, $3t_{\text{seg}}$ and $5t_{\text{seg}}$, (b) over dimensionless time for a grid column with 20 m distance from the injection location and a grid column with 200 m distance from the injection location. Reprinted from Becker et al. [2018] with permission from John Wiley & Sons, copyright 2018.

the VE gas plume. In conclusion, if the gas plume in equilibrium is small compared to the vertical height of grid cells, the relative permeability criterion will lead to higher values than the saturation criterion.

Around the injection location both criteria show very high values (figure 4.3 (a)). Here the brine and gas phase are not in equilibrium during the simulation since the gas phase moves continuously upward during injection. Farther away from the injection point the criteria values decrease steeply which shows that the two phases are much closer to equilibrium. The saturation criterion stays constant over most of the length of the plume while the relative permeability criterion increases slightly toward the leading edge of the plume. This is due to the decreasing thickness of the plume toward the leading edge which, as explained, is penalized more by the relative permeability criterion.

For early simulation times a non-monotonic behavior of both criteria can be observed over the length of the domain in figure 4.3 (a). This is due to the small thickness of the plume in early times and the grid discretization. In some parts of the domain the vertical location of the gas plume will correspond well with the vertical spacing of the computational grid, while in others the saturation will be more smeared out due to the

finite size of the grid cells. This effect grows less important as the gas plume height increases with time and contains an increasing number of cells in the vertical direction. Both criteria include a normalization with the height of the VE plume, which leads to a large peak in criterion values when the leading edge of the gas plume moves into a cell that has previously been fully saturated with brine. This can be observed in figure 4.3 (b) for early times. The peak in criterion value is followed by a non-monotonic decrease for both criteria. This is again due to the finite size of the cells and a simultaneous increase of VE gas plume height.

We define requirements for good *a posteriori* criteria for vertical equilibrium, to compare the two local criteria that we developed. In practice, a good local criterion for vertical equilibrium should:

1. locally start at a high value for early injection times and decrease over time steeply until $t_{sim} > t_{seg}$, then tend toward zero;
2. show enough difference in value when comparing grid columns close to injection and far away from it.

Both criteria fullfill the second requirement with very large differences in criterion values at the injection and farther away from it (figure 4.3 (a)). For a fixed location in space as in figure 4.3 (b) the criteria values seem to flatten out with time and it appears that they converge to a low, non-zero value. This value is defined by the finite grid size in the vertical direction beyond which the approximation of the vertical profile cannot be further improved. In comparison, the criterion based on the relative permeability shows an overall more promising behavior. It decreases faster for earlier times and it shows differences also when comparing values at the leading edge and the middle of the plume.

Since the local criterion depends on the simulation result of the full multidimensional model, the results depend on the resolution of the grid. If the grid is too coarse, it will take longer for the brine phase to drain out of the plume because part of the gas phase will be smeared out over the grid cells by numerical diffusion. This inaccuracy will directly be reflected by the local criterion because the profiles in the vertical direction will not resemble vertical equilibrium. In those cases, higher criterion values can occur although in a real scenario the two phases may already be in equilibrium. The local criterion is only able to give information about the real physical behavior of the system

when grid resolution is fine enough and the full multidimensional model gives accurate enough results.

4.3.4 Adaptive algorithm

During the simulation, regions where the VE assumption is valid can appear or disappear and change in location and size. At the beginning of injection, the less dense gas phase is usually not in equilibrium with the denser brine phase. Over time, the brine phase drains out of the plume and the area where the VE model can be applied increases. Around the well, the flow field will always have components in the vertical direction and require a full multidimensional resolution at all times. Furthermore, even an already segregated plume can reach heterogeneous zones that require a full multidimensional resolution for accuracy. An efficient model therefore adapts automatically to changes during the simulation.

We develop an algorithm for adaptation that applies the VE model in all regions where the VE assumption is valid and tests the validity in every time step. The location of the boundaries between the two submodels are found based on the local criteria for vertical equilibrium from the last time step. The local criterion is evaluated for each full multidimensional grid column before each time step. If the criterion value c_{crit} is smaller than a user-defined threshold value ϵ_{crit}, the grid column is assumed to be in vertical equilibrium. Depending on the criterion value and the threshold, either one of the following decisions is made for each grid column:

1. A full multidimensional grid column stays full multidimensional if the VE criterion is not met ($c_{\text{crit}} \geq \epsilon_{\text{crit}}$).

2. A full multidimensional grid column is turned into a VE column if the VE criterion is met ($c_{\text{crit}} < \epsilon_{\text{crit}}$) and the column is not a direct neighbor to a column where the criterion is not met.

3. A VE grid column is turned into a full multidimensional grid column if it is a direct neighbor to a column where the criterion is not met.

The criterion value is used directly to turn full multidimensional grid columns into VE columns. The third requirement from above is required to turn VE columns back into

full multidimensional cells. Together with the second requirement it results in a buffer zone around the VE columns, which is made up of full multidimensional columns (see figure 4.4). It guarantees that a VE column is converted back to a full multidimensional column before the flow field returns to full multidimensional at this location. This approach with one layer of buffer cells assumes that the subdomain boundary does not need to be moved more than one cell into the horizontal direction in each time step, which should be guaranteed by fulfilling the CFL criterion of the explicit time stepping. For stability reasons (e.g., to prevent frequent switching of columns from VE to full multidimensional and back) the buffer zone can be extended to have more than one layer. We note that Yousefzadeh and Battiato [2017] apply a similar buffer zone for a hybrid multiscale model for single-phase transport in porous media, by enlarging the subdomain where continuum-scale equations are invalid. Their coupling conditions lead to the coupling error being bounded by the upscaling error, which can be minimized by placing the coupling boundary further away from the reacting front.

With the VE criteria used in this approach, all single-phase columns will be converted to VE columns (except for buffer cells). However, in cases where the detailed vertical movement of a single phase is of interest (e.g., a leaky well or a fault zone that could be reactivated), we think it best to apply a spatially and temporally fixed full multidimensional subdomain to this region. First, those critical regions are known beforehand and usually need to be meshed accordingly. Second, even a different criterion, e.g., a vertical flux criterion that would work for single phase columns in theory, cannot detect the later onset of vertical movement in a single phase grid column, because the grid column would have been converted to a VE grid column before that.

4.4 Results and discussion

In this section, we use a heterogeneous test case to test accuracy, robustness and computational efficiency of the multiphysics model. We compare the solution against results from a full multidimensional model and a VE model. Based on the comparison, we develop guidelines for the choice of the threshold value ϵ_{crit}. The multiphysics model and the full multidimensional model are both implemented in DuMu$^{\text{x}}$ [Flemisch et al., 2011, Koch et al., 2020], allowing for a comparison of the different methods within

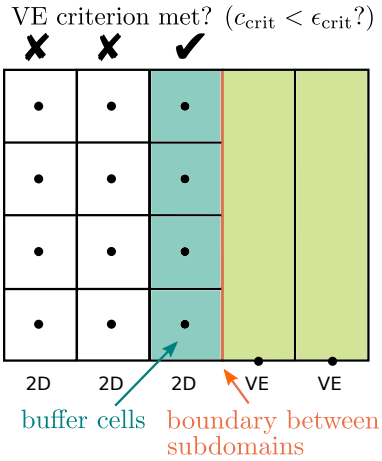

Figure 4.4: Buffer zone between full multidimensional subdomain and VE subdomain: one (or several) grid column(s) that fullfill the requirement of vertical equilibrium (according to the applied criterion) but are still kept as full multidimensional grid columns to detect changes in the flow field. Reprinted from Becker et al. [2018] with permission from John Wiley & Sons, copyright 2018.

the same software framework. The code to produce the results presented here can be obtained from https://git.iws.uni-stuttgart.de/dumux-pub/Becker2018a.git.

In the test case, we again inject CH_4 into a previously brine-saturated domain (see figure 4.5). We uniformly inject 0.0175 kg/s/m gas for 192 h. The scenario is equal to

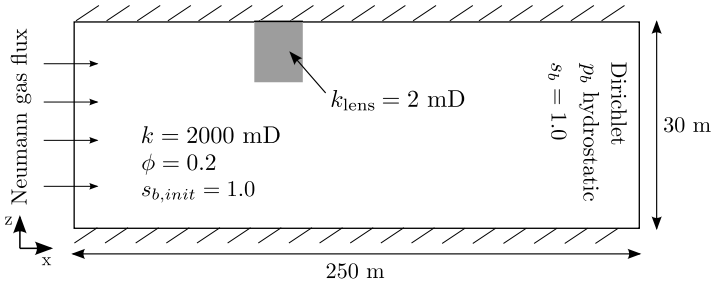

Figure 4.5: A test of gas injection for the adaptive model. A low-permeability lens is located at the top of the aquifer at 100 m distance from the injection location. Reprinted from Becker et al. [2018] with permission from John Wiley & Sons, copyright 2018.

the one used to analyze the VE criterion values with the same geological parameters and the same fluid properties. Additionally, a low-permeability lens directly below the top boundary of the aquifer is added ($k_{lens} = 2$ mD). The lens is located at 100 m distance from the injection location with a length of 20 m and a height of 10 m. The entry pressure of the low-permeability lens is kept the same as inside the domain. The

gas phase will pool in front of the lens and flow around it while a small part of the gas phase may migrate into the lens. This creates a full multidimensional flow pattern that can only be resolved accurately with a full multidimensional simulation. For simplicity, we solve the injection scenarios in two dimensions (horizontal and vertical directions). However, we note that this is not a necessity for the coupling algorithm. We choose a grid resolution of 1 m in the horizontal direction and (in the full multidimensional subdomain) 0.23 m in the vertical direction and apply the relative permeability criterion to identify subregions. We vary the threshold value between 0.01 and 0.06 to analyze its influence on the simulations and develop recommendations for the choice of the threshold value. A full multidimensional solution is obtained on a two-dimensional grid with a grid resolution of 1 m in the horizontal direction and 0.23 m in the vertical direction.

4.4.1 Comparison between models

We show the resulting gas phase saturation distribution of the adaptive multiphysics model with a threshold value of 0.03 for different times in figure 4.6. At the beginning of simulation, only the single-phase region is turned into a VE subdomain by the adaptive algorithm, which means that the entire gas plume is located within the full multidimensional subdomain. After a few simulated hours, a second VE subdomain starts developing in the middle of the plume where, according to the criterion, the two fluid phases have reached vertical equilibrium. When the plume reaches the low-permeability lens, a full multidimensional region develops around it and accurately captures the flow of gas phase around the obstacle. Farther away from the lens, another VE subdomain develops after some time. During the entire simulation, the area around the injection stays a full multidimensional subdomain as expected. The advancing thin leading edge is always resolved in full dimensions as well, because water constantly drains out of it. The full multidimensional region around the leading edge of the plume serves here as an indicator for heterogeneous regions like the lens, that would otherwise not be recognized.

We compare the results from the adaptive multiphysics model with a threshold value of 0.03, full multidimensional model, and VE model in figure 4.7. The newly developed multiphysics model compares well with the full multidimensional model: the horizontal

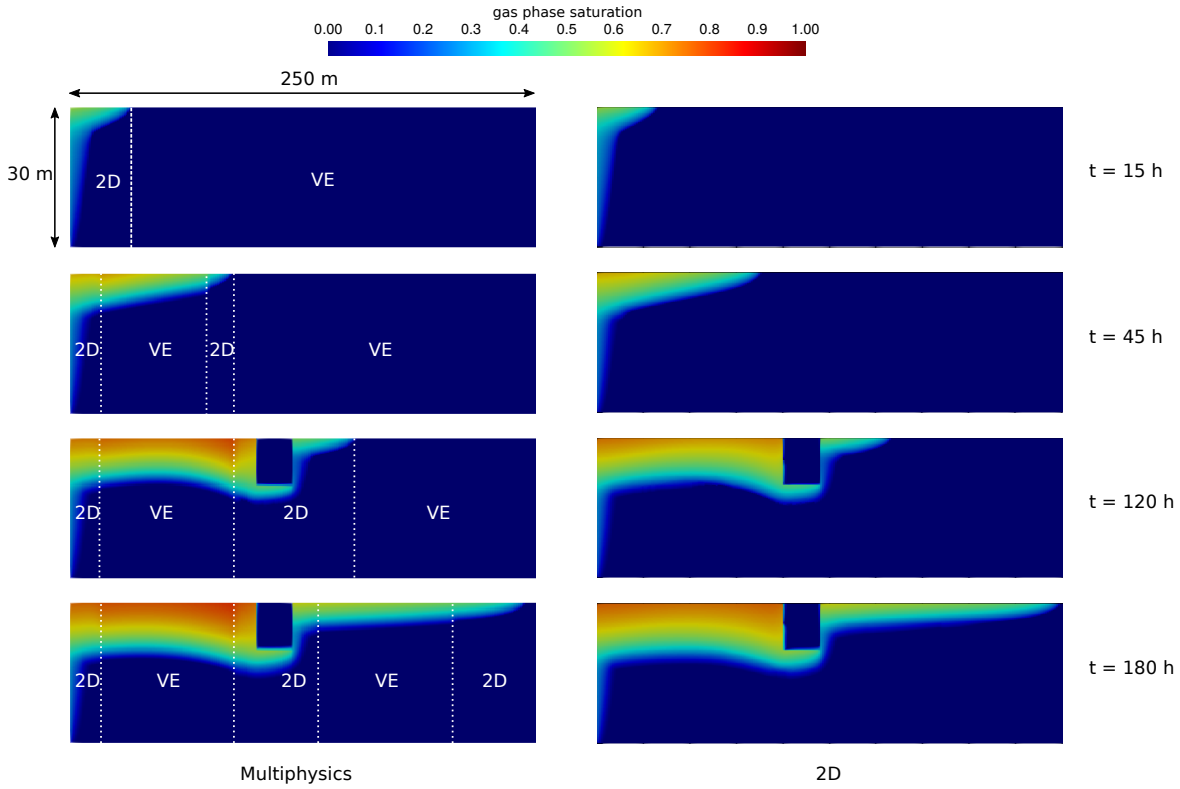

Figure 4.6: Gas phase distribution for the adaptive multiphysics model with a threshold value of 0.03 (left) and for the full multidimensional solution calculated on a two-dimensional grid (right) for a series of simulation times after injection. Subdomain boundaries are marked by dotted lines. The reconstructed solution is shown in the VE subdomains . The domain is homogeneous except for a low-permeability lens at 100 m distance from the injection location. Reprinted from Becker et al. [2018] with permission from John Wiley & Sons, copyright 2018.

extent of the plume is represented correctly as is the diversion of the gas phase around the low-permeability lens. Differences to the full multidimensional solution are evident in the VE subdomain region, where a higher brine phase saturation is calculated in the plume. In the full multidimensional model the brine phase is retained at a low saturation within the gas plume due to its low mobility resulting from the nonlinear relative permeability relationship. Vertical drainage in this state continues only at a very low rate and is not reproduced by the VE model which assumes that no brine phase above residual saturation is held back in the gas plume. This could be improved by a pseudo-VE model that assumes a pseudo-residual brine phase saturation in the plume which is higher than the residual saturation and reduced dynamically due to slow vertical drainage [Becker et al., 2017]. We note that the full multidimensional model

does not necessarily give better solutions in the VE subdomain. If the VE assumption is valid, the VE model may be equally as accurate or more accurate than the solution of the full multidimensional model since it does not rely on a finite grid discretization in the vertical direction [Nilsen et al., 2011, Bandilla et al., 2014, Celia et al., 2015]. The full VE model leads to an underestimation of the horizontal extent of the plume because it is assumed that the gas phase is in equilibrium with the brine phase at all locations. This leads to the gas phase entering the lens since the entry pressure here is not different than in other parts of the domain. Because of the low permeability in the lens, large parts of the gas phase that have entered the lens are retained there.

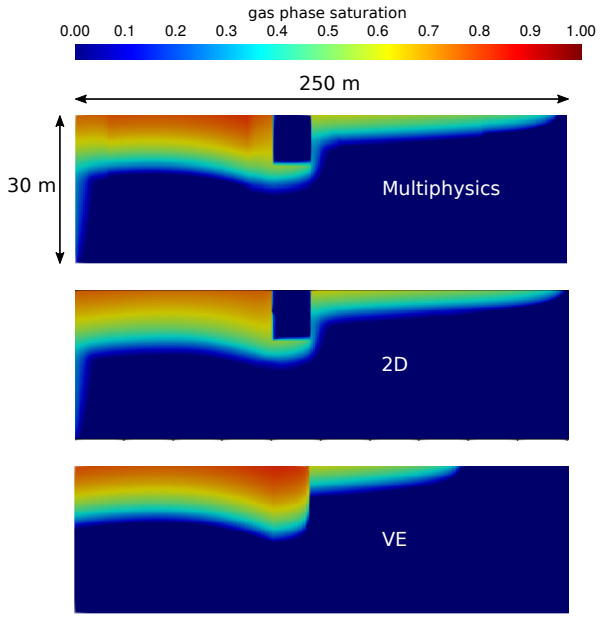

Figure 4.7: Gas phase distribution for the adaptive multiphysics model with a threshold value of 0.03 (top), full multidimensional solution calculated on a two-dimensional grid (middle) and full VE model (bottom). The simulation time is $t = 180\,\mathrm{h}$. Reprinted from Becker et al. [2018] with permission from John Wiley & Sons, copyright 2018.

The adaptive multiphysics model is significantly faster than the full multidimensional model even though this is a small test case. Table 4.1 shows the average number of cells and the CPU times for the models. The speed-up in the adaptive model is attributed to the reduction in the number of computational cells. It leads to a smaller linear system to be solved for the pressure step in the IMPES algorithm and thus lower computational costs. Note that we expect the adaptive multiphysics model to be even more computationally efficient for larger, three-dimensional test cases, because evaluating the coupling criterion and adapting the grid requires relatively little computational

Table 4.1: Relative average number of cells (compared to the full multidimensional model) and relative CPU times for full VE model, adaptive multiphysics model (with different threshold values ϵ) and full multidimensional model.

Model	relative average number of cells [-]	relative CPU time [-]
Full VE	0.008	0.003
Multiphysics $\epsilon_{\text{relPerm}} = 0.06$	0.04	0.02
Multiphysics $\epsilon_{\text{relPerm}} = 0.05$	0.11	0.05
Multiphysics $\epsilon_{\text{relPerm}} = 0.04$	0.12	0.06
Multiphysics $\epsilon_{\text{relPerm}} = 0.03$	0.19	0.12
Multiphysics $\epsilon_{\text{relPerm}} = 0.02$	0.3	0.18
Multiphysics $\epsilon_{\text{relPerm}} = 0.01$	0.41	0.22
Full multidimensional	1	1

resources.

For different threshold values we plot the number of cells in the domain over simulated time in figure 4.8. As expected, the number of computational cells is higher for lower threshold values at any time. At the beginning of injection, the number of cells increases as the plume advances regardless of which threshold value is chosen. For higher threshold values, the number of cells remains stable as soon as a VE subdomain develops within the gas plume. For the lower threshold value of 0.02 the plume develops a VE subdomain region only when the low-permeability lens is reached and the gas phase is backed up. This is indicated by a drop in number of cells in the domain. Until the end of the simulation the gas plume has not yet developed a VE subdomain after the lens, which is why the number of cells is still increasing at the end of the simulation time for this threshold value and lower threshold values. For an even lower threshold value of 0.01 the entire plume is discretized with the full multidimensional model over all times. Since the plume advances into the domain over the entire time of simulation, the number of cells increases steadily for this threshold value. Even so, a significant speed-up compared to a non-adaptive, full two-dimensional model is achieved, since the one-phase region is a VE subdomain at all times. In many practical cases the extent of the plume in the horizontal plane may be one or two orders of magnitude smaller than the domain and is locally restricted due to alternating injection and extraction cycles, making the adaptive model even more favorable.

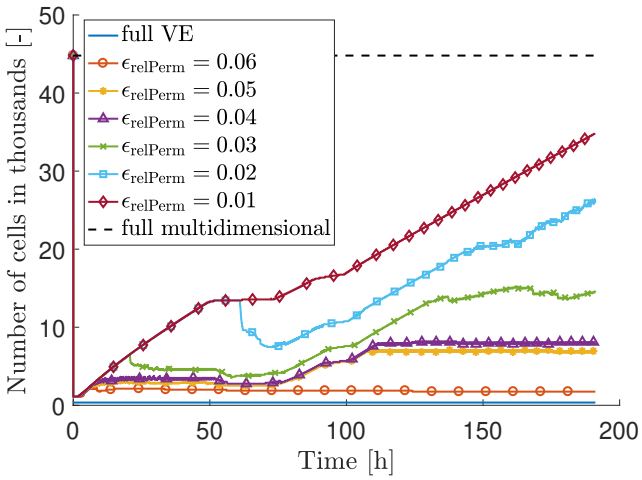

Figure 4.8: Number of computational cells in the domain over simulated time for full VE model, adaptive multiphysics model (with different threshold values ϵ) and full multidimensional model. Reprinted from Becker et al. [2018] with permission from John Wiley & Sons, copyright 2018.

4.4.2 Choice of threshold value for adaptive coupling

We analyze the influence of the threshold value and give recommendations for the choice of the threshold. We plot vertically averaged brine phase saturation for the full VE model, for the multiphysics model with different threshold values and the full multidimensional model in figure 4.9. For a very low threshold, where the entire plume is discretized with a full multidimensional model, the results match very well with the full multidimensional model. Differences with the full multidimensional model increase slightly with an increase in threshold value, especially for the averaged saturation in front of the low-permeability lens and the location of the subdomain boundaries. At the subdomain boundaries the averaged brine phase saturation shows non-monotonic behavior with more gas phase in the VE subdomain than in the full multidimensional subdomain. This is likely due to small differences between the two models at the subdomain boundary: the VE model assumes vertical equilibrium of the two fluid phases which is not completely represented by the full multidimensional model at that location, either because of finite grid size in the vertical direction or because the two phases are physically not in vertical equilibrium yet. For a high threshold value, the low-permeability lens is not detected anymore and the results differ greatly from the previous results, especially at the low-permeability lens and in the region behind it, as

a consequence of gas phase being trapped within the lens. The same is observed for the full VE model, with an additional difference in averaged brine phase saturation close to the injection region.

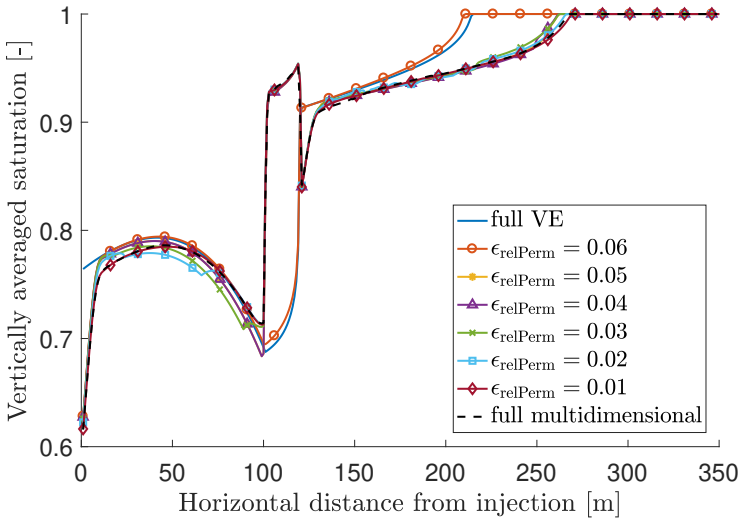

Figure 4.9: Vertically averaged brine phase saturation over horizontal distance from injection location at $t = 192$ h for full VE model, adaptive multiphysics model (with different threshold values ϵ) and full multidimensional model. Reprinted from Becker et al. [2018] with permission from John Wiley & Sons, copyright 2018.

We identify three major sources of errors in our models: upscaling error due to applying the VE model in regions that are not in vertical equilibrium, discretization error due to insufficient grid resolution especially in the vertical direction, and coupling error at the subdomain boundary. Upscaling error is controlled by the threshold value while discretization error mainly applies to the full multidimensional model and the full multidimensional subdomains in the multiphysics model. In this context we analyze the influence of the threshold value on the accuracy of the adaptive multiphysics model. We measure accuracy with respect to a full multidimensional reference that was obtained on a very fine grid determined by grid convergence ($\Delta x = 0.25$, $\Delta y = 0.05$). The resolution of this grid is considered to be small enough so that errors due to discretization are minimized but would be impracticable in real applications. It is used here to calculate the L2-norm error of the brine phase saturation for the full multidimensional model on the coarser and more practicable grid, the full VE model and the multiphysics model. Prior to calculating the L2-norm error, the solution on the coarser grids is refined in a post-processing step, assuming that refined grid cells contain the

same saturation value as the father cell. In the case of full VE model or VE subdomain, the solution is reconstructed with the same resolution as the reference grid. Then, we determine the L2-norm error of the brine phase saturation, which is calculated as the square root of the sum of squares of the saturation differences between each cell of the reference grid and the refined full multidimensional grid, reconstructed full VE grid, or refined and reconstructed multiphysics grid. This way, we can put the accuracy of the multiphysics model into context of the discretization error of the full multidimensional model, as shown in figure 4.10 for a simulated time $t = 192\,\mathrm{h}$. It can clearly be seen that the L2-norm error of the multiphysics model is similar to the L2-norm error of the full multidimensional model, within a wide range of the threshold values. Even when only small parts of the domain (injection area, advancing edge of the plume, low-permeability lens) are resolved with a full multidimensional model, the multiphysics model still gives very accurate results. This is because losses in accuracy of the multiphysics model due to coupling error that leads, e.g., to the non-monotone vertically averaged saturation at the subdomain boundary observed in figure 4.9, are outbalanced by a better representation of the plume in the VE subdomains of the multiphysics model. The coarse grid resolution in the vertical direction however leads to a high discretization error and thus a significant L2-norm error for the full multidimensional model. We can see that a large threshold value ($\epsilon = 0.06$) leads to an L2-norm error close to that from the VE model, which is significantly higher than for smaller threshold values ($\epsilon \leq 0.05$). The jump in the L2-norm error indicates that in this case the multiphysics model fails to accurately capture the relevant physical processes in the domain, like gas phase flowing around the low-permeability lens. We note that this transition between L2-norms from one criterion value to another is likely going to be smoother for a situation with more than one relevant local heterogeneity. For a threshold value only slightly lower than this critical value (e.g., $\epsilon = 0.05$), the multiphysics model is much faster than the full multidimensional model while showing the same accuracy, which makes it a very efficient model.

An optimal threshold value can be determined by varying the threshold from larger to smaller values. In analogy to a grid convergence study, we determine the appropriate (average) size of the VE subdomain by adding step-wise more full multidimensional cells. The threshold value has to be reduced in small steps so that a region for the threshold value can be identified for which the results do not change significantly anymore with further reduction of the threshold value. This can be seen in figure 4.9,

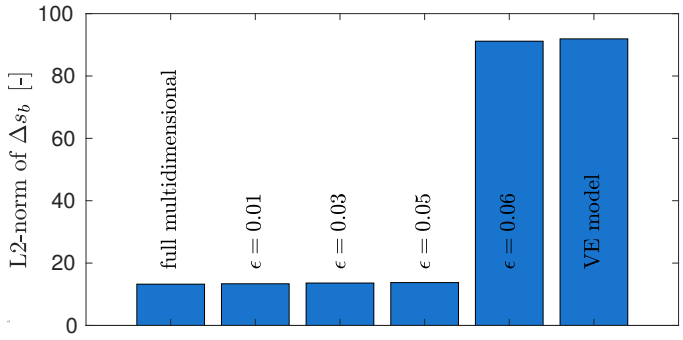

Figure 4.10: L2-norm error of brine phase saturation at $t = 192\,\mathrm{h}$ for full multidimensional model, adaptive multiphysics model (with different threshold values ϵ) and full VE model. Comparison is done with respect to a full multidimensional reference on a very fine grid determined by grid convergence. Reprinted from Becker et al. [2018] with permission from John Wiley & Sons, copyright 2018.

where for a very high threshold value the results are much different from all lower threshold values. This approach may require multiple runs of the multiphysics model before the optimal threshold value is found. However, starting with a high threshold for the multiphysics model results already in a very fast model and once the optimal threshold value is found, a large number of most efficient simulation runs can be carried out, e.g., for a Monte-Carlo type simulation.

4.5 Conclusion

In this chapter we have developed an adaptive multiphysics model that couples a full multidimensional model to a VE model. The coupling is realized in a monolithic framework. We couple the fluxes over the subdomain boundaries by using variables in the full multidimensional boundary cells and reconstructed fine-scale variables in the VE boundary subcells. The unknown variables in the VE subcells are expressed as fine-scale reconstructions of the VE cell variables using the assumption of vertical equilibrium. The pressure and saturation equations are solved sequentially with an IMPES algorithm, where we solve the pressure implicitly for the entire domain. The subdomains are assigned adaptively during simulation based on a local, *a posteriori* criterion for vertical equilibrium that compares computed and reconstructed vertical profiles of saturation or relative permeability in the grid columns.

The adaptive multiphysics model showed high accuracy in predicting the gas phase distribution with a much smaller number of grid cells and consequently lower computational cost compared to a full multidimensional model. The multiphysics model can accurately capture full multidimensional flow dynamics, e.g., around the injection location or heterogeneities farther away, and has a high accuracy in the VE subdomains where the VE assumption is valid. The threshold value to determine the VE subdomains can be chosen by decreasing the threshold value step-wise in a test similar to grid convergence tests. Overall, the multiphysics model coupling VE and full multidimensions is an efficient tool for modeling large scale applications of gas injection in the underground.

5 Multiphysics model for compositional two-phase flow

Compositional flow is an important feature of a numerical model in the context of subsurface gas storage. In practice, maximum inflow and outflow rates, development of reservoir pressure and gas plume shape in time are of importance, but because the gas is to be extracted and, e.g., used in industry, to produce energy, or for mobility purposes, its molecular composition is of great interest, as well. The gas composition will change depending on temperature and pressure due to brine components evaporating and mixing with the storage gas, but also due to geochemical or biochemical reactions. In addition, dissolution of the storage gas into the brine phase can occur, which reduces the total amount of retrievable and thus commercially usable gas. In some cases, convective mixing can even further accelerate the dissolution process. Modeling compositional processes generally increases the complexity of models and with that the computational cost, which is why efficient and accurate compositional models for energy storage in the underground need to be developed. The concept of vertical equilibrium can be exploited in the context of compositional flow to develop fast models that give accurate solutions. In addition to phase equilibrium, which develops when a less dense gas phase is injected into the resident brine and moves upward to pool below an impermeable barrier, chemical equilibrium forms along the vertical direction driven by the chemical potential between the phases and diffusion within the phases. Inside the gas-phase plume, chemical equilibrium can be considered to be valid almost instantaneously, whereas chemical equilibrium along the entire depth of the aquifer is reached only in much larger time scales. In this chapter we develop a vertically integrated compositional model and adaptively couple it to a compositional full multidimensional model. We use the compositional VE model in regions of the domain where the compositional VE assumption is valid, and the compositional full multidimensional model

everywhere else. The compositional VE model is coupled to the compositional full multidimensional model by formulating the volume change due to fluxes across subdomain boundaries. We develop and analyze local criteria to identify where the compositional VE assumption is valid in the domain, including extraction and hysteretic effects on the coarse scale. As the multiphysics model runs, VE subdomains are identified by the local criterion and the models are assigned adaptively to these regions. We use two test cases: gas injection into a horizontal layer and gas storage with reversed flow in an idealized dome-shaped aquifer, and demonstrate efficiency and accuracy of the compositional VE model and the compositional multiphysics model.

In section 5.1, a sequential compositional, full multidimensional model is presented. Based on this, the vertically integrated model is developed in section 5.2 and the coupling strategy is presented in section 5.3. Following that, criteria for compositional VE are developed and analyzed, and the adaptive solution algorithm is presented in section 5.4. Finally, section 5.5 shows the applicability of the developed compositional multiphysics model by means of two gas storage scenarios.

5.1 Compositional full multidimensional model

The sequential compositional flow model uses a volume balance formulation for its pressure equation, as derived in section 2.2.3, which makes it possible to directly include changes of density due to changes of composition. We focus on the two components water and gas and neglect geochemical and biochemical reactios in this work. We remark that the model can be extended for multiple components and that chemical reactions can be included in the source and sink terms.

In the following, section 5.1.1 explains the sequential solution algorithm. Then, section 5.1.2 gives the estimation of partial derivatives of the total specific volume in a pre-computational step prior to each time step. Section 5.1.3 presents the computation of secondary variables like, e.g., phase saturation by flash calculations. The discretized governing equations are given in section 5.1.4 and the advective flux calculation is presented in section 5.1.5.

5.1.1 Sequential solution algorithm

The sequential solution algorithm to solve equations (2.21) and (2.22) with (2.10) is illustrated in figure 5.1. The pressure equation is solved implicitly, while the transport equations are solved explicitly, resulting in an implicit pressure, explicit transport (IMPET) scheme. We first compute an estimate for the transport, leading to an estimate of the change of total specific volume of fluid phases $\hat{v}$ [-] with varying total concentration of the components c^κ [M/L^3] and varying pressure. Then the pressure equation (2.22) is solved, with one pressure as the primary variable (e.g., the brine pressure p_b) and all secondary variables (densities, viscosities, relative permeabilities, capillary pressure, saturations, mass fractions, total volume) taken from the previous time step. With the new pressure field, the transport equations (2.21) for each component are solved, leading to an update of the total concentrations. All secondary variables are used from the previous time step. The time stepping criterion is based on a CFL condition [Courant et al., 1928] that requires that the representative flux of each cell does not exceed the available storage of that cell. The representative flux is defined as the maximum volumetric out- or influx of each cell, as proposed by Helmig et al. [2010]. A flash calculation finally determines mass fractions and saturations. With that, all other secondary variables that are used in the next time step can be updated.

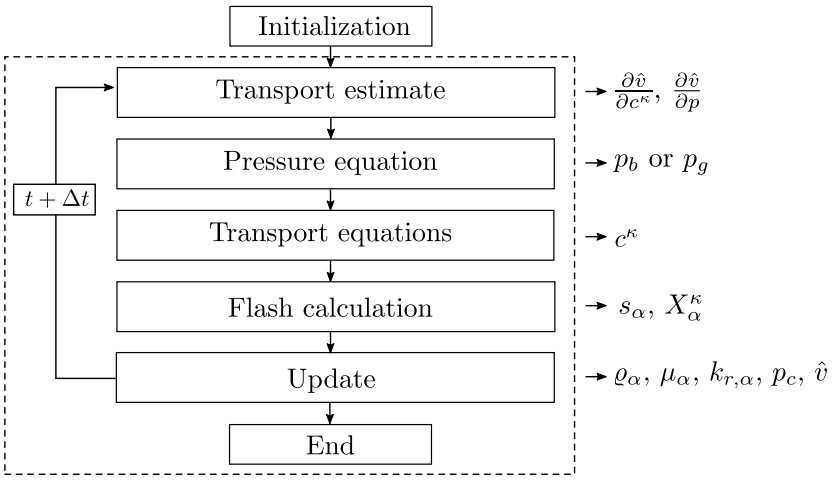

Figure 5.1: Algorithm for the sequential compositional flow model.

5.1.2 Transport estimate

The partial derivatives of the total specific volume of fluid phases $\hat{v}$ with respect to changes in total concentration c^κ and pressure are determined numerically, following the procedure developed by [Fritz, 2010]. For changes in pressure, this is done by increasing the pressure slightly. The change in total specific volume is calculated with the standard flash routine used in the simulation (see section 5.1.3). If this leads to unphysical (i.e., positive, see Trangenstein and Bell [1989]) values of the partial derivative, the pressure is decreased slightly. If this leads to unphysical values again, phase transition is neglected.

For changes in total concentration, a more sophisticated approach is used to determine the offset. First, the transport equations are solved based on the pressure field of the previous time step, with updated saturation-dependent secondary variables and the time step size of the previous time step. Then, the offset in total concentration of each component is taken from this transport estimate and the total specific volume is determined with the standard flash, individually for each component offset. Due to the nonlinearity of the relationship, [Fritz, 2010] found this secant approach to be more accurate than determining the tangent using a very small offset of total concentrations.

5.1.3 Flash calculations

The flash calculations are written using the definition for feed mass fraction z^κ [-] (ratio of component mass to total fluid mass) and phase mass fraction ν_α [-] (ratio of phase mass to total fluid mass):

$$z^\kappa = \frac{m^\kappa}{\sum_\kappa m^\kappa}, \tag{5.1}$$

$$\nu_\alpha = \frac{m_\alpha}{\sum_\alpha m_\alpha}, \tag{5.2}$$

where m^κ is the total mass of component κ [M] and m_α the total mass of phase α [M]. Input for the isothermal flash calculation are feed mass fraction z^κ, pressures p_α and the constant temperature. The flash is based on the thermodynamic requirement that the fugacities f_α^κ [M/(L T^2)] of a component in two phases are equal when those phases

are in equilibrium:

$$f_\alpha^\kappa = f_\beta^\kappa. \tag{5.3}$$

Using the fugacity coefficients φ_α^κ [-] and mole fractions x_α^κ [-] to define the fugacities as $f_\alpha^\kappa = x_\alpha^\kappa \varphi_\alpha^\kappa p_\alpha$ leads (for a system with one liquid and one gaseous phase) to:

$$x_l^\kappa \varphi_l^\kappa p_l = x_g^\kappa \varphi_g^\kappa p_g. \tag{5.4}$$

The mole equilibrium ratios k_α^κ [-] determine the ratio of mole fraction of κ in phase α to the mole fraction of κ in the reference phase. For a two-phase, two-component system with brine and gas phases and components water and gas, and the brine phase as the reference phase, the mole equilibrium ratios are calculated as follows:

$$k_b^w = \frac{x_b^w}{x_b^w} = 1, \tag{5.5}$$

$$k_b^g = \frac{x_b^g}{x_b^g} = 1, \tag{5.6}$$

$$k_g^w = \frac{x_g^w}{x_b^w} = \frac{\varphi_b^w p_b}{\varphi_g^w p_g} = \frac{p_{\text{vap}}^w}{p_g}, \tag{5.7}$$

$$k_g^g = \frac{x_g^g}{x_b^g} = \frac{\varphi_b^g p_b}{\varphi_g^g p_g} = \frac{H_b^g}{p_g}, \tag{5.8}$$

$$\tag{5.9}$$

where p_{vap}^w is the vapor pressure [M/(L T^2)] of pure brine (usually depends on temperature) and H_b^g is the Henry coefficient [M/(L T^2)] for the gas component in the brine phase (usually depends on temperature). Using Raoult's and Henry's law implies that the effect of composition of a phase on dissolution is neglected. For the determination of fugacity coefficients see A.1.

Together with the requirement that $\sum_\kappa x_\alpha^\kappa = 1$ in each phase, the mole fractions in equilibrium can now be calculated:

$$x_b^w = \frac{1 - k_g^g}{k_g^w - k_g^g}, \tag{5.10}$$

$$x_g^w = x_b^w k_g^w, \tag{5.11}$$

$$x_b^g = 1 - x_b^w, \tag{5.12}$$

$$x_g^g = 1 - x_g^w. \tag{5.13}$$

In a second step, the Rachford-Rice equation [Rachford Jr. and Rice, 1952] for two phases is used to determine the phase mass fractions ν_α:

$$\sum_\kappa \frac{z^\kappa (K_\alpha^\kappa - 1)}{1 + \nu_\alpha (K_\alpha^\kappa - 1)} = 0, \tag{5.14}$$

where K_α^κ are mass equilibrium ratios [-]. For two phases and two components this equation can be written for the (reference) brine phase and rearranged to give the phase mass fraction ν_b directly:

$$\nu_b = 1 + \frac{(K_g^w - 1) z^w + (K_g^g - 1)(1 - z^w)}{(K_g^w - 1)(K_g^g - 1)}. \tag{5.15}$$

For a derivation of the multiphase Rachford-Rice equation see A.2.

In a third step, the phase distribution is calculated (as well as all other missing secondary variables):

$$s_\alpha = \frac{\nu_\alpha / \varrho_\alpha}{\sum_\alpha (\nu_\alpha / \varrho_\alpha)}. \tag{5.16}$$

The mole fractions calculated above assuming equilibrium between two phases only hold if two phases are present. If $\nu_b \leq 0$, only a gas phase is present and the mass (and mole) fractions are corrected to $X_g^w = z^w$, $X_g^g = 1 - z^w$. Conversely, if $\nu_b \geq 1$ only brine phase is present and the mass fractions are corrected to $X_b^w = z^w$, $X_b^g = 1 - z^w$.

5.1.4 Discretization in space

The transport equations (2.21) and the pressure equation (2.22) are discretized in space using a finite volume method. The domain is subdivided into cells i with the volume V_i, that are connected via interfaces γ, which each have the area A_i. The discretization points are located in the center of the cells, and most fluid properties are considered to be constant within a cell volume V_i.

Using a two-point flux approximation, the transport equation (2.21) can be discretized

as:

$$\frac{\Delta c_i^\kappa}{\Delta t} = \sum_\gamma \frac{A_\gamma}{V_i} \boldsymbol{n}_\gamma^T \boldsymbol{k} \boldsymbol{d}_{ij} \sum_\alpha X_\alpha^\kappa \varrho_\alpha \lambda_\alpha \left(\frac{p_{\alpha,j} - p_{\alpha,i}}{\Delta x} + \varrho_\alpha g \frac{z_j - z_i}{\Delta x} \right) + q_i^\kappa, \quad \alpha = b,\, g, \tag{5.17}$$

where $\boldsymbol{n}_\gamma$ is the normalized vector orthogonal to the interface γ and pointing outward of the cell i, $\boldsymbol{d}_{ij}$ is the normalized vector connecting the centers of the cells i and j and pointing away from i, and Δx is the distance between the centers of the cells i and j. Note that we neglect diffusion in this implementation of the model.

When the pressure equation (2.22) is integrated over a volume G with surface Γ and normal $\boldsymbol{n}_\Gamma$, it results in:

$$\int_G \frac{\partial \hat{v}}{\partial p} \frac{\partial p}{\partial t} dG - \int_G \sum_\kappa \frac{\partial \hat{v}}{\partial c^\kappa} \nabla \cdot \left(\sum_\alpha X_\alpha^\kappa \varrho_\alpha \boldsymbol{u}_\alpha \right) dG + \int_G \sum_\kappa \frac{\partial \hat{v}}{\partial c^\kappa} q^\kappa dG = \int_G \frac{\phi - \hat{v}}{\Delta t} dG, \tag{5.18}$$

with

$$\int_G \sum_\kappa \frac{\partial \hat{v}}{\partial c^\kappa} \nabla \cdot \left(\sum_\alpha X_\alpha^\kappa \varrho_\alpha \boldsymbol{u}_\alpha \right) dG = \oint_\Gamma \sum_\kappa \frac{\partial \hat{v}}{\partial c^\kappa} \boldsymbol{n}_\Gamma \cdot \left(\sum_\alpha X_\alpha^\kappa \varrho_\alpha \boldsymbol{u}_\alpha \right) d\Gamma - \int_G \nabla \sum_\kappa \frac{\partial \hat{v}}{\partial c^\kappa} \cdot \left(\sum_\alpha X_\alpha^\kappa \varrho_\alpha \boldsymbol{u}_\alpha \right) dG. \tag{5.19}$$

The volume integral on the right-hand side of equation (5.19) can only be neglected in slightly compressible systems [Pau et al., 2012] where the volume derivatives can be considered piecewise constant in each cell. For other cases, Fritz et al. [2012] proposed dividing each cell into one subvolume per interface γ, scaling by the face area A_γ and the cells surface U_i. In each of these subvolumes, the gradient of each volume derivative is approximated linearly between the values in cell i and j. The total compressibility $\frac{\partial \hat{v}}{\partial p}$, the sources q^κ and the error term $\frac{\phi - \hat{v}}{\Delta t}$ are considered piecewise constant within the

volume G. The pressure equation is then discretized as:

$$
\begin{aligned}
V_i \frac{\partial \hat{v}_i}{\partial p_i} \frac{p_i^t - p_i^{t-\Delta t}}{\Delta t} \\
+ \sum_\gamma A_\gamma \boldsymbol{n}_\gamma^T \boldsymbol{k} \boldsymbol{d}_{ij} \sum_\alpha \varrho_\alpha \lambda_\alpha \left(\frac{p_{\alpha,j}^t - p_{\alpha,i}^t}{\Delta x} + \varrho_\alpha g \frac{z_j - z_i}{\Delta x} \right) \sum_\kappa X_\alpha^\kappa \frac{\partial \hat{v}}{\partial c^\kappa} \\
- \sum_\gamma V_i \frac{A_\gamma}{U_i} \boldsymbol{n}_\gamma^T \boldsymbol{k} \boldsymbol{d}_{ij} \sum_\alpha \varrho_\alpha \lambda_\alpha \left(\frac{p_{\alpha,j}^t - p_{\alpha,i}^t}{\Delta x} + \varrho_\alpha g \frac{z_j - z_i}{\Delta x} \right) \sum_\kappa X_\alpha^\kappa \frac{\frac{\partial \hat{v}_j}{\partial c_j^\kappa} - \frac{\partial \hat{v}_i}{\partial c_i^\kappa}}{\Delta x} \\
= -V_i \sum_\kappa \frac{\partial \hat{v}}{\partial c^\kappa} q_i^\kappa + V_i \frac{\phi_i - \hat{v}_i}{\Delta t}, \quad \alpha = b,\, g, \qquad (5.20)
\end{aligned}
$$

with all coefficients calculated on the old time level $t - \Delta t$. To solve the equation, one of the two pressures is eliminated using the capillary pressure.

5.1.5 Advective flux calculation

We use full upwinding [Helmig, 1997] for the flux-related properties phase density ϱ_α, phase mobility λ_α and mass fraction X_α^κ. The upstream cell is determined by the sign of the potential gradient of each phase:

$$
\Phi_{\alpha,ij} = \frac{p_{\alpha,i} - p_{\alpha,j}}{\Delta x} + \bar{\varrho}_\alpha g \frac{z_i - z_j}{\Delta x}, \quad \alpha = b,\, g. \qquad (5.21)
$$

The pressures and densities are determined from the previous time step. If the sign of the potential gradient is positive for phase α, the flux-related properties for phase α are taken from cell i; if it is negative, they are taken from the neighboring cell j. In the case of gravity-influenced systems where counter-current flow may occur, the signs of the potential gradients and resulting upwind directions may be different for different phases. To obtain a unique potential gradient for each phase, the phase density $\bar{\varrho}_\alpha$ is centrally weighted between cells i and j.

The permeability tensor in equations (5.19) and (5.20) is determined by calculating the harmonic mean of corresponding entries of the tensors in the cells adjacent to the interface γ. The volume derivative $\frac{\partial \hat{v}}{\partial c^\kappa}$ is centrally weighted between cells i and j.

5.2 Compositional VE model

Compositional processes in a VE context have been introduced by Gasda et al. [2011a], using an upscaled representation of the dissolution-convection process. The model assumes chemical equilibrium within a gas-phase plume containing mobile and immobile CO_2, with concentrations being constant within the entire gas-phase plume. A drying front within the gas-phase plume is neglected. The dissolution of CO_2 across the macroscale interface between gas-phase plume and brine region below is modeled assuming a constant dissolution rate. It is assumed that the dissolved CO_2 usually comes from the immobile CO_2 region of the gas-phase plume, and from the mobile region only if there is no immobile region. Additionally, the brine region below the gas-phase plume is assumed to have a constant (averaged) CO_2 concentration in the vertical direction. Horizontal fluxes are calculated separately for each region in the VE cell, accounting for the different densities in brine with and without dissolved gas. The unknown variables, pressure, concentration of CO_2 in the brine below the gas-phase plume and the thickness of the mobile and immobile CO_2 regions, are determined using the total component mass balance equations and an additional component transport equation for dissolved CO_2. The system is assumed to be incompressible due to pressure changes but volume changes due to dissolution are included. A sharp interface is assumed in this work, but a follow-up paper extends the model to include a capillary transition zone [Gasda et al., 2011b]. The model is applied to the Johansen formation and it is shown that residual trapping, capillary forces, and dissolution have a great impact on gas plume migration and long-term trapping. Integrating compositional processes in a vertical equilibrium context also has been developed and tested by Nilsen et al. [2016b] for a sharp-interface VE model considering residual CO_2 and dissolution of CO_2 in brine only. Two models were developed: one with instant dissolution of CO_2 into brine along the vertical height of the cell, and a second one with a (constant) rate-dependent dissolution of CO_2 into brine (similar to Gasda et al. [2011a], assuming constant concentrations within the entire gas-phase plume). The dissolved CO_2 is assumed to come from the residual region of the gas-phase plume and only from the mobile gas-phase region if the residual part is absent. A mass balance for CO_2, brine and dissolved CO_2 is used to solve the system. Lateral transport of dissolved CO_2 induced by density differences is not regarded since this would require separate description of fluxes from the pure brine and the brine with dissolved CO_2. Results with both developed models show that there is a significant to-

tal amount of gas components dissolving into brine, which in turn has a strong influence on gas plume development. This approach is extended by Møyner et al. [2020], with a numerical upscaling to account for the transient dissolution of gas components below the gas-phase plume. For this purpose, tables are generated based on pre-computed one-dimensional simulations, that link the vertical height of the column, coarse-scale pressure, temperature, time since onset of dissolution and total mass of components to the coarse-scale deviaton from chemical equilibrium. Furthermore, this framework allows coupling of a full multidimensional model (e.g., near the injection region) to a compositional VE model. However, subdomains need to be assigned *a priori*. The developed model proved to be efficient as its results compared well against those from fine-scale simulations, especially regarding the accumulated mass of gas components in brine and gas phase.

In this section we present a compositional VE model that allows for mutual dissolution/evaporation of water and gas components, directly includes volume changes due to pressure and composition, and takes lateral transport due to density differences into account. The model is rigorously derived by integrating the full multidimensional compositional governing equations (2.22) and (2.21) over the height of the aquifer. In the following, we first discuss states of VE in the context of compositional multiphase flow in section 5.2.1. Necessary simplifications for our compositional VE model for underground energy storage and assumptions for the reconstruction of the fine-scale solution in the vertical direction are presented in section 5.2.2. Section 5.2.3 shows the derivation of the vertically integrated governing equations of our compositional VE model and section 5.2.4 gives the discretized form of these equations, using a finite volume approach. In section 5.2.5 we describe the advective flux calculation while section 5.2.6 discusses the role of volume mismatch in the compositional VE model. Finally, the reconstruction of fine-scale variables in the vertical direction is presented in section 5.2.7.

5.2.1 States of compositional VE

Three different states of vertical equilibrium can be identified for compositional flow in the context of gas storage:

1. Phase equilibrium: gas and brine phase are in equilibrium, resulting in hydrostatic pressure distribution in the vertical direction.

2. Chemical equilibrium within the gas-phase plume: everywhere where the gas phase is present there is chemical equilibrium between the gas and brine phase contained in this region. Chemical equilibrium means that, locally, the chemical potential between the present phases is equal.

3. Chemical equilibrium over the entire depth of the aquifer. This includes chemical equilibrium within the gas-phase plume as described above, as well as a fully gas-saturated brine phase below the gas-phase plume.

We expect the time scales for these three equilibrium states to differ greatly, with phase equilibrium being reached first, followed almost instantaneously by chemical equilibrium within the gas-phase plume. The time scale associated with chemical equilibrium over the entire depth of the aquifer would then be expected to be much larger. Reasons for the different time scales are the two main mechanisms that lead to phase transitioning between gas and brine phase due to chemical potential: dissolution across the pore-scale interfaces in volumes of the porous medium containing both gas and brine phase, and dissolution across large-scale interfaces (which exist on the pore scale but can be localized on a larger scale) that separate bulks of gas and brine phase (e.g., across the boundary between gas-phase plume and brine region below). Everywhere where gas and brine phase are both present in a volume of porous material, phase transition is an almost instantaneous process, since the pore-scale interfaces separating the phases have a very large specific area. Dissolution across pore-scale interfaces occurs mainly near the injection region, where the gas and brine phases are not in equilibrium and distributed over the entire depth of the aquifer. Furthermore, dissolution across pore-scale interfaces occurs within the developing gas-phase plume, until the residual brine phase disappears due to evaporation of all water into the gas phase (drying front). Dissolution across pore-scale interfaces also plays a role when the mobile gas phase retreats, leaving residual gas phase, which may come in contact with fresh brine, until all gas components are dissolved in brine (wetting front).

Dissolution across large-scale interfaces is a slow process in general, since the large-scale interface separating the phases has a relatively small specific area, and the dissolution rate is often limited by diffusion carrying components away from the large-scale interface. As a result, dissolution across large-scale interfaces may only be relevant in later

times. However, in some cases it may be accelerated by convective mixing. Convective mixing means that density differences in the phases due to different compositions lead to fluxes within one phase that increase the concentration difference over a large-scale interface. As an example, CO_2 that diffuses from the gas-phase plume into the brine phase below increases the brine-phase density. The heavier brine phase sinks to the bottom of the aquifer (often inducing instabilities, i.e., fingering), bringing fresh, non-saturated brine phase back up to the gas-phase plume. This way, the concentration difference across the boundary of the gas-phase plume is maintained and dissolution of CO_2 remains at a steady rate. This system has been studied extensively in the context of CO_2 storage [Lindeberg and Bergmo, 2003, Ennis-King and Paterson, 2005, Riaz and Hesse, 2006, Farajzadeh et al., 2007, Pruess and Zhang, 2008, Pau et al., 2010].

Both mechanisms can be accounted for by numerical models. Dissolution across pore-scale interfaces is included usually by applying local chemical equilibrium on the level of a computational cell, meaning local equilibrium is reached instantaneously, or by applying a chemical non-equilibrium model for each cell. While difffusive fluxes to/from neighboring cells may be accounted for by simulations, dissolution over cell boundaries is usually not implemented explicitly. Nevertheless, dissolution over large-scale interfaces is included implicitly in simulations. There is usually no sharp representation of the large-scale interface, but rather a smearing over one layer of cells within which a chemical equilibrium model is assumed. As a result, dissolution over large-scale interfaces occurs implicitly inside the cells where the large-scale interface is located.

Three different model concepts for compositional VE can be identified as illustrated in figure 5.2, associated with increasing complexity. Figure 5.2 (a) shows a simple model concept for compositional VE where the fluid phases and the components are assumed to be in equilibrium over the entire vertical direction. In reality, this state will only be reached in the entire domain after a very long time that is possibly much larger than the time required to reach phase equilibrium. As a result, compositional VE models assuming chemical equilibrium over the entire depth of the aquifer are only applicable for long time scales. If smaller time scales are of interest, compositional VE models may assume chemical equilibrium in the gas-phase plume only, as depicted in figure 5.2 (b). Diffusion/dissolution over the interface between gas-phase plume and brine region below is neglected, assuming pure brine below the gas-phase plume. Compositional VE models assuming chemical equilibrium restricted to the gas-phase plume are of medium complexity since gas-phase plume and region below are treated differently.

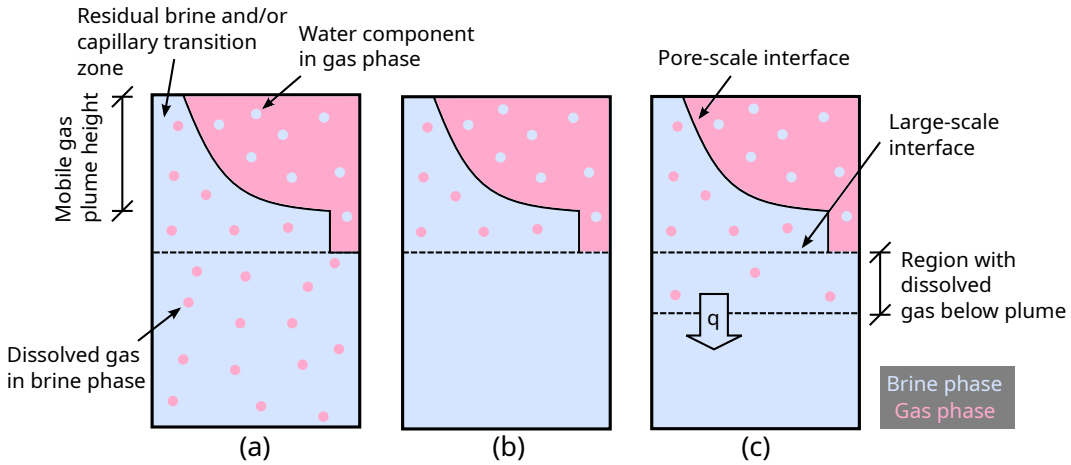

Figure 5.2: Three different model concepts for compositional VE with increasing complexity: (a) assuming chemical equilibrium over the entire depth of the aquifer, (b) assuming chemical equilibrium only in the gas-phase plume, (c) assuming chemical equilibrium in the gas-phase plume and a rate q of components dissolving into brine below the gas-phase plume. Note that the height of the gas-phase plume may differ between (a)-(c).

Applicability of such models is given only for short time scales or cases where there is no convective mixing. Figure 5.2 (c) shows a model concept of high complexity that deals with the transition between both compositional VE states by assuming chemical equilibrium in the gas-phase plume and applying a component flux across the large-scale interface. Diffusion/dissolution over the large-scale interface can be modelled in form of a component flux that is driven by the concentration difference, or as an upscaled dissolution rate, which may be assumed to be constant. Furthermore, the presence of gas components below the gas-phase plume could also be caused by lateral transport of brine containing gas components or by a gas phase present in this region prior to reaching phase equilibrium. Assumptions have to be made about the profile of the concentration of gas components in the vertical direction below the gas-phase plume, e.g., constant concentration of gas components in brine directly below the gas-phase plume, or an averaged concentration over the entire depth below the gas-phase plume.

5.2.2 Model assumptions

In order to develop an efficient and robust model for underground energy storage, and in particular to enable reconstruction of the fine-scale solution in the vertical direc-

tion, a number of assumptions and simplifications for our compositional VE model are necessary. These assumptions and simplifications are summarized in this section.

The components of interest in underground energy storage (e.g., hydrogen, methane) do not induce a convective mixing behaviour in our simulations. This is because these components have smaller molar masses than H_2O and would decrease the density of the brine, according to simplified mixing laws that assume that one molecule of liquid component is replaced by one molecule of gas component [Class and Helmig, 2002]. Consequently, our compositional VE model neglects the dissolution of gas components below the gas-phase plume. We note that, if necessary, the model can be extended to include such a process in the same way as presented by Gasda et al. [2011a], Nilsen et al. [2016b] or Møyner et al. [2020].

Reconstruction of the fine-scale solution in the vertical direction requires assumptions about vertical profiles of phase saturations, phase pressure, mass fractions, phase density and phase viscosity. The profile of phase saturation follows from the assumption of vertical equilibrium of phases, and is similar to the saturation profile of immiscible VE models, with a brine-phase region with pure brine phase below a gas-phase plume in chemical equilibrium, where the saturation profile follows the inverse of the capillary-saturation relationship. The pressure variation along the vertical direction is hydrostatic according to vertical equilibrium of phases as well. However, the increase of pressure with depth is now dependent on density and composition, which may change along the vertical direction due to pressure changes. As a simplification, we assume a constant gas phase density and constant mass fractions of components in the gas phase, which depend on a reference gas phase pressure, defined as the gas phase pressure at the top of the aquifer. This is possible for the gas phase without introducing significant errors, since the variations of gas phase pressure along the vertical direction will be small. Further, we assume a constant brine phase density and constant mass fractions of components in the brine phase inside the gas-phase plume, and a constant (pure) brine phase density below the gas-phase plume. Phase viscosities are assumed to be constant within gas-phase plume and below, as well. The reference brine phase pressure for properties inside the gas-phase plume is defined as the brine phase pressure at the lower end of the gas-phase plume, the reference brine phase pressure for properties below the gas-phase plume is defined as the brine phase pressure at the bottom of the aquifer. Since the brine phase can be assumed to be much less compressible than the gas phase, this simplification should not introduce significant errors. Furthermore,

property variations along the vertical direction are less significant than property variations along the horizontal direction, as long as the vertical extent of the domain is much smaller than the horizontal extent [Bachu, 2002]. Reference pressures and resulting secondary variables such as phase densities inside the plume and equilibrium mass fractions, which in turn affect the height of the gas-phase plume and thus pressure profiles, are iterated to find a consistent state.

Due to dissolution of water components into pure gas that is injected, a drying front develops inside the gas-phase plume with a one-phase gas region forming, starting at the injection region and travelling farther into the gas-phase plume as injection continues. A second front (wetting front) develops after injection has stopped or when extraction has begun, with gas components from residual gas phase being dissolved in the brine phase until a one-phase state with brine phase only is reached. Depending on the process that dictates the direction in which the mobile gas phase moves, this front can travel through the plume from both sides. Both drying and wetting fronts are neglected in this model.

With the model assumptions above we can reconstruct the fine-scale solution in the vertical direction, as shown qualitatively in figure 5.3 for the brine phase saturation, phase pressures, mass fractions of the water component, and phase densities. The profile of the brine phase saturation in the gas-phase plume follows the inverse of the capillary pressure curve and is piecewise constant below the gas-phase plume. The pressure distribution is assumed to be hydrostatic, with different constant slopes in the region of the gas-phase plume and below it. Densities and mass fractions (and, analogously, viscosities, which are not pictured) inside the gas-phase plume and below are piecewise constant, due to different composition and different reference pressures in those regions.

5.2.3 Governing equations

In the following, we apply the simplifications and assumptions discussed in section 5.2.2. We neglect dissolution across the large-scale interface between gas-phase plume and pure brine phase below the plume, and assume that all gas components are located inside the gas-phase plume, which is in chemical equilibrium (VE state (b) in figure 5.2). We largely neglect the influence of pressure variations along the vertical direction

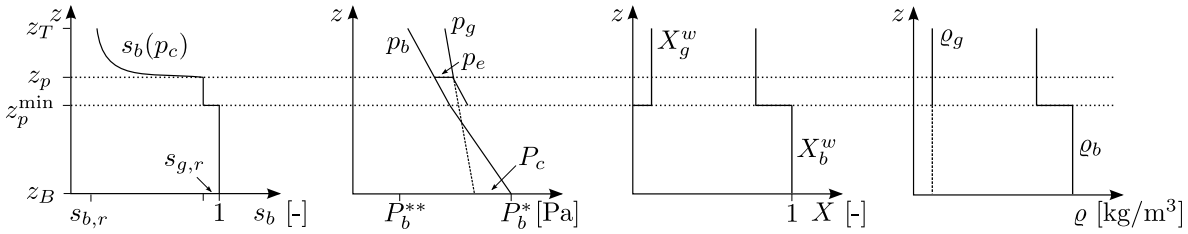

Figure 5.3: Assumed vertical profiles of brine phase saturation, phase pressures, mass fractions of the water component, and phase densities. We (optionally) include a capillary transition zone and assume no dissolution below the gas-phase plume. The profile of the brine phase saturation in the mobile gas region follows the inverse of the capillary pressure curve. Pressure distribution is assumed to be hydrostatic. Densities and mass fractions are piecewise constant inside the gas-phase plume and below.

on equilibrium mass fractions, phase densities and phase viscosities, by assuming a constant value for these properties inside the gas-phase plume and below.

The governing equations of the compositional VE model are derived by integrating the full multidimensional equations over the height of the aquifer. First we demonstrate this for the pressure equation, by integrating equation (2.22):

$$\int_{z_B}^{z_T} \frac{\partial \hat{v}}{\partial p}\frac{\partial p}{\partial t} dz - \int_{z_B}^{z_T} \sum_\kappa \frac{\partial \hat{v}}{\partial c^\kappa} \nabla \cdot \left(\sum_\alpha X_\alpha^\kappa \varrho_\alpha \boldsymbol{u}_\alpha \right) dz + \int_{z_B}^{z_T} \sum_\kappa \frac{\partial \hat{v}}{\partial c^\kappa} q^\kappa dz = \int_{z_B}^{z_T} \frac{\phi - \hat{v}}{\Delta t} dz, \quad \alpha = b,\, g. \tag{5.22}$$

Due to the assumption of hydrostatic pressure distribution, $\frac{\partial p}{\partial t}$ is constant over z and neglecting the influence of pressure, $X_\alpha^\kappa \varrho_\alpha$ is piecewise constant inside the gas-phase plume and below it, respectively. Further, we move the volume derivatives $\frac{\partial \hat{v}}{\partial p}$ and $\frac{\partial \hat{v}}{\partial c^\kappa}$ out of the integral because we obtain these terms by exploiting the entire VE reconstruction mechanism for varying pressure and total concentration as an averaged value for the entire VE cell. This leads to:

$$\begin{aligned} \left(\frac{\partial \hat{V}}{\partial P}\right)^{\mathrm{VE}} \frac{\partial P}{\partial t} - \sum_\kappa \left(\frac{\partial \hat{V}}{\partial C^\kappa}\right)^{\mathrm{VE}} \nabla_{//} \cdot \left(X_b^{\kappa,*} \varrho_b^* \boldsymbol{U}_b^* + \sum_\alpha X_\alpha^{\kappa,**} \varrho_\alpha^{**} \boldsymbol{U}_\alpha^{**} \right) \\ + \sum_\kappa \left(\frac{\partial \hat{V}}{\partial C^\kappa}\right)^{\mathrm{VE}} Q^\kappa = \frac{\Phi - \hat{V}}{\Delta t}, \quad \alpha = b,\, g, \end{aligned} \tag{5.23}$$

with $\hat{V} = \int_{z_B}^{z_T} \hat{v} dz$, $C^\kappa = \int_{z_B}^{z_T} c^\kappa dz$ and $Q^\kappa = \int_{z_B}^{z_T} q^\kappa$. The superscript VE indicates that we obtain the values in parenthesis by exploiting the VE reconstruction mechanism. Properties below the plume are denoted with superscript $(*)$, inside the plume with superscript $(**)$. The coarse scale Darcy velocities $\boldsymbol{U}_b^*$ and $\boldsymbol{U}_\alpha^{**}$ are defined as:

$$\begin{aligned}
\boldsymbol{U}_b^* &= \int_{z_B}^{z_p^{\min}} \boldsymbol{u}_{b,//} = \int_{z_B}^{z_p^{\min}} -\boldsymbol{k}_{//}\lambda_b \left(\nabla_{//} p_b + \varrho_b g \nabla_{//} z\right) dz = -\boldsymbol{K}^* \Lambda_b^* \left(\nabla_{//} P_b^* + \varrho_b^* g \nabla_{//} z_B\right), \\
\boldsymbol{U}_\alpha^{**} &= \int_{z_p^{\min}}^{z_T} \boldsymbol{u}_{\alpha,//} = \int_{z_p^{\min}}^{z_T} -\boldsymbol{k}_{//}\lambda_\alpha \left(\nabla_{//} p_\alpha + \varrho_\alpha g \nabla_{//} z\right) dz = -\boldsymbol{K}^{**} \Lambda_\alpha^{**} \left(\nabla_{//} P_\alpha^{**} + \varrho_\alpha^{**} g \nabla_{//} z_B\right), \\
&\qquad\qquad\qquad\qquad\qquad\qquad\qquad\qquad\qquad\qquad\qquad\qquad \alpha = b,\, g,
\end{aligned} \tag{5.24}$$

with P_b^* defined at the bottom of the aquifer and P_α^{**} defined at the top of the aquifer. The depth-integrated permeability and depth-averaged relative permeability below and above the plume are defined as:

$$\boldsymbol{K}^* = \int_{z_B}^{z_p^{\min}} \boldsymbol{k}_{//} dz, \tag{5.25}$$

$$\Lambda_b^* = \boldsymbol{K}^{*^{-1}} \int_{z_B}^{z_p^{\min}} \boldsymbol{k}_{//}\lambda_b dz, \tag{5.26}$$

$$\boldsymbol{K}^{**} = \int_{z_p^{\min}}^{z_T} \boldsymbol{k}_{//} dz, \tag{5.27}$$

$$\Lambda_\alpha^{**} = \boldsymbol{K}^{**^{-1}} \int_{z_p^{\min}}^{z_T} \boldsymbol{k}_{//}\lambda_\alpha dz, \quad \alpha = b,\, g. \tag{5.28}$$

The VE transport equations are determined by integrating equation (2.21), as:

$$\frac{\partial C^\kappa}{\partial t} = -\nabla_{//} \cdot \left(X_b^{\kappa,*} \varrho_b^* \boldsymbol{U}_b^* + \sum_\alpha X_\alpha^{\kappa,**} \varrho_\alpha^{**} \boldsymbol{U}_\alpha^{**} \right) + Q^\kappa, \quad \alpha = b,\, g. \tag{5.29}$$

The governing equations are solved using the same sequential solution algorithm used for the full multidimensional equations, with a transport estimate to determine volume derivatives, an implicit pressure step using coefficients based on the previous time level to compute the pressure field with equation (5.23), and an explicit transport step solving equation (5.29) followed by an update of all secondary variables. Time stepping is restricted by a CFL criterion as in the full multidimensional case (see section 5.1.1).

5.2.4 Discretization in space

As for the full multidimensional case, the transport equations (5.29) and the pressure equation (5.23) of the compositional VE model are discretized in space using a finite volume method. We follow closely the steps taken to discretize the governing equations of the full multidimensional model, since the form of the equations is very similar. Using a two-point flux approximation, the discretized transport equation of the compositional VE model follows as:

$$\frac{\Delta C_i^\kappa}{\Delta t} = \sum_\gamma \frac{A_\gamma}{V_i} \left(\boldsymbol{n}_\gamma^T \boldsymbol{K}^* \boldsymbol{d}_{ij} X_b^{\kappa,*} \varrho_b^* \Lambda_b^* \left(\frac{P_{b,j}^* - P_{b,i}^*}{\Delta x} + \varrho_b^* g \frac{z_{B,j} - z_{B,i}}{\Delta x} \right) + \right.$$
$$\left. \boldsymbol{n}_\gamma^T \boldsymbol{K}^{**} \boldsymbol{d}_{ij} \sum_\alpha X_\alpha^{\kappa,**} \varrho_\alpha^{**} \Lambda_\alpha^{**} \left(\frac{P_{\alpha,j}^{**} - P_{\alpha,i}^{**}}{\Delta x} + \varrho_\alpha^{**} g \frac{z_{B,j} - z_{B,i}}{\Delta x} \right) \right) + Q_i^\kappa, \quad \alpha = b,\, g. \tag{5.30}$$

The noteworthy difference to the discretized transport equation of the full multidimensional model (5.17), is that two flux-related terms appear within the large brackets. They appear this way as we treat fluxes from inside the plume separately from fluxes from below the plume.

The discretized pressure equation of the compositional VE model is:

$$
\begin{aligned}
&V_i \left(\frac{\partial \hat{V}_i}{\partial P_i}\right)^{\mathrm{VE}} \frac{P_i^t - P_i^{t-\Delta t}}{\Delta t} \\
&+ \sum_\gamma A_\gamma \left(\boldsymbol{n}_\gamma^T \boldsymbol{K}^* \boldsymbol{d}_{ij} \varrho_b^* \Lambda_b^* \left(\frac{P_{b,j}^{t,*} - P_{b,i}^{t,*}}{\Delta x} + \varrho_b^* g \frac{z_{B,j} - z_{B,i}}{\Delta x} \right) \sum_\kappa X_b^{\kappa,*} \left(\frac{\partial \hat{V}}{\partial C^\kappa} \right)^{\mathrm{VE}} \right. \\
&\left. + \boldsymbol{n}_\gamma^T \boldsymbol{K}^{**} \boldsymbol{d}_{ij} \sum_\alpha \varrho_\alpha^{**} \Lambda_\alpha^{**} \left(\frac{P_{\alpha,j}^{t,**} - P_{\alpha,i}^{t,**}}{\Delta x} + \varrho_\alpha^{**} g \frac{z_{B,j} - z_{B,i}}{\Delta x} \right) \sum_\kappa X_\alpha^{\kappa,**} \left(\frac{\partial \hat{V}}{\partial C^\kappa} \right)^{\mathrm{VE}} \right) \\
&- \sum_\gamma V_i \frac{A_\gamma}{U_i} \left(\boldsymbol{n}_\gamma^T \boldsymbol{K}^* \boldsymbol{d}_{ij} \varrho_b^* \Lambda_b^* \left(\frac{P_{b,j}^{t,*} - P_{b,i}^{t,*}}{\Delta x} + \varrho_b^* g \frac{z_{B,j} - z_{B,i}}{\Delta x} \right) \sum_\kappa X_b^{\kappa,*} \frac{\left(\frac{\partial \hat{V}_j}{\partial C_j^\kappa}\right)^{\mathrm{VE}} - \left(\frac{\partial \hat{V}_i}{\partial C_i^\kappa}\right)^{\mathrm{VE}}}{\Delta x} \right. \\
&\left. - \boldsymbol{n}_\gamma^T \boldsymbol{K}^{**} \boldsymbol{d}_{ij} \sum_\alpha \varrho_\alpha^{**} \Lambda_\alpha^{**} \left(\frac{P_{\alpha,j}^{t,**} - P_{\alpha,i}^{t,**}}{\Delta x} + \varrho_\alpha^{**} g \frac{z_{B,j} - z_{B,i}}{\Delta x} \right) \sum_\kappa X_\alpha^{\kappa} \frac{\left(\frac{\partial \hat{V}_j}{\partial C_j^\kappa}\right)^{\mathrm{VE}} - \left(\frac{\partial \hat{V}_i}{\partial C_i^\kappa}\right)^{\mathrm{VE}}}{\Delta x} \right) \\
&= -V_i \sum_\kappa \left(\frac{\partial \hat{V}}{\partial C^\kappa} \right)^{\mathrm{VE}} Q_i^\kappa + V_i \frac{\Phi_i - \hat{V}_i}{\Delta t}, \quad \alpha = b,\, g.
\end{aligned}
\tag{5.31}
$$

Again here we see two flux-related terms for fluxes inside and below the gas-phase plume, where, in the discretized equation for the full multidimensional model (5.20), there was only one term. All coefficients are calculated on the old time level $t-\Delta t$. The pressures P_α^{**} at the top of the aquifer are related to the pressures P_α^* at the bottom of the aquifer by exploiting the assumption of hydrostatic profiles and the minimum location of the gas plume known from the old time level. To solve the equation, one of the two remaining phase pressures at the bottom of the aquifer is then eliminated using the (pseudo) capillary pressure P_c.

5.2.5 Advective flux calculation

We use full upwinding for the flux-related properties inside the gas-phase plume and below the plume. Inside the gas-phase plume, the upstream cell is determined by the

sign of the potential gradient of each phase:

$$\Phi_{\alpha,ij} = \frac{P^{**}_{\alpha,i} - P^{**}_{\alpha,j}}{\Delta x} + \bar{\varrho}^{**}_{\alpha} g \frac{z_{B,i} - z_{B,j}}{\Delta x}, \quad \alpha = b,\, g. \tag{5.32}$$

As in the full multidimensional case, if the sign of the potential gradient inside the gas-phase plume is positive for phase α, phase density ϱ^{**}_{α}, the phase mobility Λ^{**}_{α} and mass fraction $X^{\kappa,**}_{\alpha}$ are taken from cell i, if it is negative, from the neighboring cell j.

Analogously, below the gas-phase plume, the upstream cell is determined by the sign of the potential gradient of the brine phase:

$$\Phi_{b,ij} = \frac{P^{*}_{b,i} - P^{*}_{b,j}}{\Delta x} + \bar{\varrho}^{*}_{b} g \frac{z_{B,i} - z_{B,j}}{\Delta x}. \tag{5.33}$$

If the sign of the potential gradient of the brine phase below the gas-phase plume is positive, brine density ϱ^{*}_{b}, the brine mobility Λ^{*}_{b} and mass fraction $X^{\kappa,*}_{b}$ are taken from cell i, if it is negative, from the neighboring cell j. Note that to obtain a unique definition of the potential gradient, the phase densities $\bar{\varrho}^{**}_{\alpha}$ and $\bar{\varrho}^{*}_{b}$ are centrally weighted between cells i and j. The pressures and densities are taken from the previous time step.

The permeability tensor in equations (5.30) and (5.31) is determined by calculating the harmonic mean of corresponding entries of the tensors in the cells adjacent to the interface γ. The volume derivative $\frac{\partial \hat{V}}{\partial C^{\kappa}}$ is centrally weighted between cells i and j.

5.2.6 Volume mismatch

The compositional full multidimensional model allows for a volume mismatch within cells, i.e., the volume of all phases in one cell does not necessarily correspond to the volume of void space of the cell. In terms of saturation, the volume mismatch is treated by defining saturation as the ratio of volume of one phase to the total volume of phases inside the cell, instead of relating the volume of one phase to the total volume of void space inside the cell. This can be seen as virtually increasing/decreasing the void space of the cell (i.e., higher/lower porosity or larger/smaller volume) to fit the volume of phases. The thus defined saturation, as well as the intensive state quantities mass/mole density and mass/mole fraction, are used as input to determine capillary pressure and

relative permeability, while fluxes are calculated with the real porosity and volume of the cell, creating an inconsistency that can not be resolved.

Transferring the concept of volume mismatches to the compositional VE model is challenging because the distribution of volume mismatches along the vertical direction is unknown. The VE cell itself only contains the net volume mismatch of the previous time step, which theoretically makes a mix of positive and negative volume mismatches along the vertical direction possible. In reality, the volume mismatch may be highest in the region of the plume, where volume-changing effects due to dissolution have the highest impact. However, since the concept of volume mismatches was introduced to stabilize the numerical scheme and has no physically meaningful representation, it could occur anywhere. Additionally, since the volume mismatch is only known from the previous time step, phase distribution and volume mismatch distribution have to be solved iteratively, which would further enlarge the already iterative (for capillary transition models) reconstruction mechanism. Therefore, we entirely neglect volume mismatches in the plume region and shift it to the bottom of the VE cell. During reconstruction of the vertical saturation profile, we fill up the cell from the top with the volume of both phases to determine the height of the gas-phase plume. The reconstruction mechanism hereby ensures that gas components and associated volume is consistent with the volume of the available pore space, so volume mismatches in the VE model can only be caused by water components. On the coarse scale, volume mismatches can easily be determined since the total mass of both components, densities of all phases in all regions, and the height of the gas-phase plume is known.

5.2.7 Reconstruction

At the end of each time step, known variables are one phase pressure at the bottom of the aquifer (e.g., the brine phase pressure P_b) and the total concentrations of both components. The constant equilibrium mass fractions inside the gas-phase plume, as well as phase densities inside and below the gas-phase plume, can be calculated, both depending on the reference phase pressures. Since the reference phase pressures largely depend on the location of the gas-phase plume, z_p, the reconstruction is iterated. As a first estimate for the reference phase pressures we exploit the pseudo capillary pressure from the previous time step. Further, $z_p^{\min}$, the minimum location of the gas plume, is

known from the previous time step. With these properties known, the location of the gas-phase plume, z_p, can be determined by a mass balance of gas components. For a sharp interface VE model neglecting capillary pressure on the fine scale, the procedure to determine z_p can be summarized as:

1. Check if the location of the gas-phase plume is smaller (case 1) or larger (case 2) than $z_p^{\min}$ from the previous time step.
2. If case 1, meaning no immobile gas phase below the mobile plume ($z_p = z_p^{\min}$), calculate the location of the gas-phase plume, z_p, and update $z_p^{\min}$.
3. If case 2, meaning an immobile area below the plume exists ($z_p > z_p^{\min}$), calculate z_p.

For a VE model with capillary transition zone, the gas-phase plume location can be smaller than z_B. This leads to a third case, and the procedure to determine z_p is as follows:

1. Check if the location of the gas-phase plume is smaller (case 1a/1b) or larger (case 2) than $z_p^{\min}$ from the previous time step.
2. If there is no immobile gas phase below the mobile plume ($z_p = z_p^{\min}$), check if the location of the gas-phase plume is larger than z_B (case 1a) or smaller than z_B (case 1b), and determine z_p accordingly. Update $z_p^{\min}$ if necessary.
3. If case 2, meaning an immobile area below the plume exists ($z_p > z_p^{\min}$), calculate z_p.

Once the location of the gas-phase plume, z_p, is known, the saturation distribution in the vertical direction can be reconstructed in the same way as for the non-compositional VE models, while largely neglecting the volume mismatch as discussed in section 5.2.6. Reconstruction of the pressures over the vertical direction is similar to the non-compositional VE model as well, assuming a hydrostatic profile, with the difference that the density of the brine phase changes in regions with and without dissolved gas. With the pressure distribution in the vertical direction known, the reference phase pressures can be updated, and with that updated equilibrium mass fractions inside the gas-phase plume and phase densities inside and below the gas-phase plume can be determined. The process of calculating the location of the gas-phase plume, z_p, is repeated until convergence.

In the following, the two reconstruction steps are shown in detail: first for a sharp interface VE model, then for a VE model with capillary transition zone. For simplification we assume that the porosity is constant in the VE cell and we choose the brine phase pressure P_b as our primary pressure variable.

Reconstruction for sharp interface model

Pressure reconstruction: Since there is no capillary pressure on the fine scale of the sharp interface VE model, both phase pressures are equal along the vertical direction. This leads to the following phase pressure distribution along the vertical direction:

$$p_b(z) = p_g(z) = \begin{cases} P_b - \varrho_b^* g(z_p^{\min} - z_B) - \varrho_b^{**} g(z_p - z_p^{\min}) - \varrho_g^{**} g(z - z_p), & z_p < z \leq z_T, \\ P_b - \varrho_b^* g(z_p^{\min} - z_B) - \varrho_b^{**} g(z - z_p^{\min}), & z_p^{\min} < z \leq z_p, \\ P_b - \varrho_b^* g(z - z_B), & z_B \leq z \leq z_p^{\min}. \end{cases} \tag{5.34}$$

We refer to figure 5.3 for a representation of the bottom of the aquifer z_B, the top of the aquifer z_T, the location of the gas-phase plume z_p and minimum location of the gas plume $z_p^{\min}$.

Saturation reconstruction, case 1 ($z_p = z_p^{\min}$): The brine phase saturation along the vertical direction is straightforward:

$$s_b(z) = \begin{cases} s_{b,r}, & z_p < z \leq z_T, \\ 1, & z_B \leq z \leq z_p. \end{cases} \tag{5.35}$$

The calculation of z_p is based on a balance of the total mass of gas components within the cell. Without a region of immobile gas phase below the mobile plume, the mass of gas components in the cell is:

$$C^g A = A(H + z_B - z_p)\phi(1 - s_{b,r})\varrho_g^{**} X_g^{g,**} + A(H + z_B - z_p)\phi s_{b,r}\varrho_b^{**} X_b^{g,**}, \tag{5.36}$$

where H is the vertical height of the cell [L], A is the area of the horizontal cross section of the cell [L^2], and $s_{b,r}$ is the residual saturation of the brine phase [-]. Rearranging

equation (5.36), gives the location of the gas-phase plume:

$$z_p = z_B + H - \frac{C^g}{\phi(1-s_{b,r})\varrho_g^{**}X_g^{g,**} + \phi s_{b,r}\varrho_b^{**}X_b^{g,**}}. \tag{5.37}$$

Saturation reconstruction, case 2 ($z_p > z_p^{\min}$): The brine phase saturation along the vertical direction is again straightforward:

$$s_b(z) = \begin{cases} s_{b,r}, & z_p < z \leq z_T, \\ 1 - s_{g,r}, & z_p^{\min} < z \leq z_p, \\ 1, & z_B \leq z \leq z_p^{\min}. \end{cases} \tag{5.38}$$

Here, the calculation of the mass of gas components in the cell is extended to include the immobile area of gas phase below the mobile plume:

$$\begin{aligned} C^g A = {} & A(H + z_B - z_p)\phi(1-s_{b,r})\varrho_g^{**}X_g^{g,**} + A(H + z_B - z_p)\phi s_{b,r}\varrho_b^{**}X_b^{g,**} \\ & + A(z_p - z_p^{\min})\phi s_{g,r}\varrho_g^{**}X_g^{g,**} + A(z_p - z_p^{\min})\phi(1-s_{g,r})\varrho_b^{**}X_b^{g,**}, \end{aligned} \tag{5.39}$$

where $s_{g,r}$ is the residual saturation of the gas phase. Rearranging equation (5.39), gives the location of the gas-phase plume:

$$\begin{aligned} z_p = {} & \frac{C^g + \phi\varrho_g^{**}X_g^{g,**}\left(z_p^{\min}s_{g,r} - (H + z_B)(1-s_{b,r})\right)}{\phi(1-s_{g,r}-s_{b,r})(\varrho_b^{**}X_b^{g,**} - \varrho_g^{**}X_g^{g,**})} \\ & + \frac{\phi\varrho_b^{**}X_b^{g,**}\left(z_p^{\min}(1-s_{g,r}) - (H + z_B)s_{b,r}\right)}{\phi(1-s_{g,r}-s_{b,r})(\varrho_b^{**}X_b^{g,**} - \varrho_g^{**}X_g^{g,**})}. \end{aligned} \tag{5.40}$$

Reconstruction for capillary transition model

Pressure reconstruction: Due to taking capillary pressure into account on the fine scale of the capillary transition VE model, the phase pressures differ according to the capillary pressure depending on saturation. The entry pressure, p_e, is the (constant) difference between the phase pressures at $s_w \geq 1.0 - s_{n,r}$ and has to be chosen according to the porous material. The phase pressures along the vertical direction follow as:

$$p_b(z) = \begin{cases} P_b - \varrho_b^* g(z_p^{\min} - z_B) - \varrho_b^{**} g(z - z_p^{\min}), & z_p^{\min} < z \leq z_T, \\ P_b - \varrho_b^* g(z - z_B), & z_B \leq z \leq z_p^{\min}, \end{cases} \tag{5.41}$$

$$p_g(z) = \begin{cases} P_b - \varrho_b^* g(z_p^{\min} - z_B) + p_e - \varrho_b^{**} g(z_p - z_p^{\min}) - \varrho_g^{**} g(z - z_p), & z_p < z \leq z_T, \\ P_b - \varrho_b^* g(z_p^{\min} - z_B) + p_e - \varrho_b^{**} g(z - z_p^{\min}), & z_p^{\min} < z \leq z_p, \\ P_b - \varrho_b^* g(z - z_B) + p_e, & z_B \leq z \leq z_p^{\min}. \end{cases} \tag{5.42}$$

The capillary pressure along the vertical direction can be calculated by substracting the brine phase pressure from the gas phase pressure:

$$p_c(z) = p_g(z) - p_b(z) = \begin{cases} p_e + (\varrho_b^{**} - \varrho_g^{**}) g(z - z_p), & z_p < z \leq z_T, \\ p_e, & z_B \leq z \leq z_p. \end{cases} \tag{5.43}$$

The capillary pressure is a function of saturation, e.g., the Brooks-Corey relationship as in equation (2.7). Using the Brooks-Corey relationship, the saturation can be reconstructed as follows.

Saturation reconstruction, case 1a ($z_p = z_p^{\min}$, $z_p > z_B$): Reconstruction of the brine phase saturation below the plume is straightforward:

$$s_b(z) = 1, \qquad z_B \leq z \leq z_p. \tag{5.44}$$

For the region of the plume, equation (5.43) is set equal to equation (2.7), and rearranged for s_b. This leads to an expression for the brine phase saturation inside the plume, depending on the location of the gas-phase plume:

$$s_b(z) = \left(p_e + (\varrho_b^{**} - \varrho_g^{**}) g(z - z_p)\right)^{-\lambda} p_e^{\lambda} (1 - s_{b,r} - s_{g,r}) + s_{b,r}, \qquad z_p < z \leq z_T. \tag{5.45}$$

To calculate the unknown z_p, we balance the coarse-scale and fine-scale mass of gas components:

$$\begin{aligned}\int_{z_p}^{z_T} \left(\phi s_b(z)\varrho_b^{**}X_b^{g,**} + \phi(1-s_b(z))\varrho_g^{**}X_g^{g,**}\right) dz &= C^g \\ = \phi\varrho_g^{**}X_g^{g,**}(z_T - z_p) \\ +\phi(\varrho_b^{**}X_b^{g,**} - \varrho_g^{**}X_g^{g,**})\left(\frac{1}{1-\lambda}\left(p_e + (\varrho_b^{**}-\varrho_g^{**})g(z_T-z_p)\right)^{1-\lambda}\frac{(1-s_{b,r}-s_{g,r})p_e^{\lambda}}{(\varrho_b^{**}-\varrho_g^{**})g}\right. \\ \left. +s_{b,r}(z_T-z_p) - \frac{p_e(1-s_{b,r}-s_{g,r})}{(1-\lambda)(\varrho_b^{**}-\varrho_g^{**})g}\right).\end{aligned} \tag{5.46}$$

This equation can not be easily rearranged to determine z_p, which is why a numerical method, e.g. Newton-Raphson, must be used to solve for it.

Saturation reconstruction, case 1b ($z_p = z_p^{\min}$, $z_p \leq z_B$): In this case, the entire vertical height of the cell is filled by the plume region. The distribution is the same as for case 1a:

$$s_b(z) = \left(p_e + (\varrho_b^{**}-\varrho_g^{**})g(z-z_p)\right)^{-\lambda} p_e^{\lambda}(1-s_{b,r}-s_{g,r}) + s_{b,r}, \qquad z_B \leq z \leq z_T. \tag{5.47}$$

To calculate the unknown z_p, we use again a mass balance of the gas components:

$$\begin{aligned}\int_{z_B}^{z_T} \left(\phi s_b(z)\varrho_b^{**}X_b^{g,**} + \phi(1-s_b(z))\varrho_g^{**}X_g^{g,**}\right) dz &= C^g \\ = \phi\varrho_g^{**}X_g^{g,**}H \\ +\phi(\varrho_b^{**}X_b^{g,**} - \varrho_g^{**}X_g^{g,**})\left(\frac{1}{1-\lambda}\left(p_e + (\varrho_b^{**}-\varrho_g^{**})g(z_T-z_p)\right)^{1-\lambda}\frac{(1-s_{b,r}-s_{g,r})p_e^{\lambda}}{(\varrho_b^{**}-\varrho_g^{**})g}\right. \\ \left. +s_{b,r}H - \frac{1}{1-\lambda}\left(p_e + (\varrho_b^{**}-\varrho_g^{**})g(z_B-z_p)\right)^{1-\lambda}\frac{(1-s_{b,r}-s_{g,r})p_e^{\lambda}}{(\varrho_b^{**}-\varrho_g^{**})g}\right).\end{aligned} \tag{5.48}$$

Again, this equation must be solved for z_p numerically.

Saturation reconstruction, case 2 ($z_p > z_p^{\min}$, $z_p > z_B$): The saturation distribu-

tion below the mobile plume is straightforward:

$$s_b(z) = \begin{cases} 1 - s_{g,r}, & z_p^{\min} < z \leq z_p, \\ 1, & z_B \leq z \leq z_p^{\min}. \end{cases} \tag{5.49}$$

The saturation distribution inside the mobile plume is the same as for cases 1a and 1b:

$$s_b(z) = \left(p_e + (\varrho_b^{**} - \varrho_g^{**})g(z - z_p)\right)^{-\lambda} p_e^{\lambda}(1 - s_{b,r} - s_{g,r}) + s_{b,r}, \qquad z_p < z \leq z_T. \tag{5.50}$$

To calculate the unknown z_p, we extend the mass balance by the region of the immobile plume, where gas is present in the residual gas phase and the surrounding brine phase. This leads to:

$$\begin{aligned} \int_{z_p}^{z_T} \left(\phi s_b(z)\varrho_b^{**}X_b^{g,**} + \phi(1 - s_b(z))\varrho_g^{**}X_g^{g,**}\right) dz \\ +(z_p - z_p^{\min})\phi s_{g,r}\varrho_g^{**}X_g^{g,**} + (z_p - z_p^{\min})\phi(1 - s_{g,r})\varrho_b^{**}X_b^{g,**} = C^g \\ = \phi\varrho_g^{**}X_g^{g,**}(z_T - z_p) \\ +\phi(\varrho_b^{**}X_b^{g,**} - \varrho_g^{**}X_g^{g,**}) \left(\frac{1}{1-\lambda} \left(p_e + (\varrho_b^{**} - \varrho_g^{**})g(z_T - z_p)\right)^{1-\lambda} \frac{(1 - s_{b,r} - s_{g,r})p_e^{\lambda}}{(\varrho_b^{**} - \varrho_g^{**})g} \right. \\ \left. +s_{b,r}(z_T - z_p) - \frac{p_e(1 - s_{b,r} - s_{g,r})}{(1-\lambda)(\varrho_b^{**} - \varrho_g^{**})g} \right) + (z_p - z_p^{\min})\phi \left(s_{g,r}\varrho_g^{**}X_g^{g,**} + (1 - s_{g,r})\varrho_b^{**}X_b^{g,**}\right). \end{aligned} \tag{5.51}$$

As for the other cases when taking a capillary transitioning zone into account, this equation must be solved for z_p numerically.

5.3 Coupling strategy

As with the case of immiscible two-phase flow, the compositional VE assumption may not be valid everywhere in the domain, mainly due to the phases not having reached equilibrium yet. This especially concerns the injection areas, where injected gas forms a gas phase that moves upward, and the tip of the advancing/retreating gas-phase plume, where brine drains out of or imbibes the gas region. In extraction areas, the detailed location and composition of the gas phase is of high importance, which is

why a full multidimensional model may be desired here, too. Therefore, we couple the compositional full multidimensional model and the compositional VE model in one domain. In the following, we first explain the coupling by formulating the volume change due to fluxes across the subdomain boundaries in section 5.3.1, and present the computational algorithm to solve the governing equations in section 5.3.2.

5.3.1 Volume change due to fluxes across subdomain boundaries

We exploit the similarity between the pressure equation (2.22), including (2.10), of the compositional full multidimensional model and the pressure equation (5.23), including (5.24), of the compositional VE model to couple both models in one domain. Both equations balance a storage term describing the change of total specific volume of all phases due to pressure changing over time, with volume changes due to fluxes, a source/sink term and a residual describing discrepancies in total specific volume and porosity. The two compositional models are coupled together by formulating the change of total specific volume of phases due to fluxes across the subdomain boundaries (second term in equations (2.22) and (5.23)) and requiring continuity. For that purpose, we refine the VE cell on one side of the subdomain boundary into full multidimensional subcells in the vertical direction. Each subcell shares an interface with a neighboring cell in the full multidimensional subdomain. The discretized form of the volume change due to fluxes from the full multidimensional cell i to a VE subcell $j^{'}$ on the other side of the boundary between subdomains is:

$$
\begin{aligned}
&A_{\gamma}^{'}\boldsymbol{n}_{\gamma}^{T}\boldsymbol{k}^{'}\boldsymbol{d}_{ij^{'}}\sum_{\alpha}\varrho_{\alpha}^{'}\lambda_{\alpha}^{'}\left(\frac{p_{\alpha,j}^{t,'}-p_{\alpha,i}^{t}}{\Delta x}+\varrho_{\alpha}^{'}g\frac{z_{j'}-z_{i}}{\Delta x}\right)\sum_{\kappa}X_{\alpha}^{\kappa,'}\left(\frac{\partial\hat{v}}{\partial c^{\kappa}}\right)^{'}\\
&-V_{i}\frac{A_{\gamma}}{U_{i}}\boldsymbol{n}_{\gamma}^{T}\boldsymbol{k}^{'}\boldsymbol{d}_{ij}\sum_{\alpha}\varrho_{\alpha}^{'}\lambda_{\alpha}^{'}\left(\frac{p_{\alpha,j}^{t,'}-p_{\alpha,i}^{t}}{\Delta x}+\varrho_{\alpha}^{'}g\frac{z_{j'}-z_{i}}{\Delta x}\right)\sum_{\kappa}X_{\alpha}^{\kappa,'}\frac{\left(\frac{\partial\hat{v}_{j}}{\partial c_{j}^{\kappa}}\right)^{'}-\frac{\partial\hat{v}_{i}}{\partial c_{i}^{\kappa}}}{\Delta x},\\
&\qquad\qquad\qquad\qquad\qquad\qquad\qquad\qquad\qquad\qquad\qquad\qquad\alpha=b,\,g,
\end{aligned}
\tag{5.52}
$$

where all coefficients are calculated from the previous time step. $A_{\gamma}^{'}$ is the face area shared by the full multidimensional cell and the VE subcell, and $\boldsymbol{k}^{'}$ is determined by calculating the harmonic mean of corresponding entries of the tensors in the full multidimensional cell and the VE subcell. One phase pressure $p_{\alpha,j}^{'}$ is replaced by $p_{c}(\bar{s}_{b,j}^{'})$,

where $\bar{s}_{b,j}^{'}$ is the brine phase saturation in the VE subcell that would form under conditions of chemical equilibrium within the subcell, using averaged total concentrations and reconstructed pressures of the subcell from the previous time step to establish the state of chemical equilibrium. The remaining phase pressure $p_{\alpha,j}^{'}$ is the reconstructed pressure at the calculation point of the VE subcell and is expressed using the phase pressure at the bottom of the VE cell, P_α. For details on pressure reconstruction we refer to equations (5.34) for a sharp interface VE model, and equations (5.41) and (5.42) for a VE model with capillary transitioning zone. We use full upwinding for the reconstructed flux-related properties phase density $\varrho_\alpha^{'}$, phase mobility $\lambda_\alpha^{'}$ and mass fraction $X_\alpha^{\kappa,'}$, depending on the phase potential as described before. The phase potential is:

$$\Phi_{\alpha,ij'} = \frac{p_{\alpha,i} - p_{\alpha,j}^{'}}{\Delta x} + \bar{\varrho}_\alpha^{'} \frac{z_{i'} - z_j}{\Delta x}, \quad \alpha = b,\, g, \tag{5.53}$$

where $\bar{\varrho}_\alpha^{'}$ is centrally averaged between cell i and $j^{'}$, and pressures and densities are taken from the previous time step. If the sign of the potential is positive, the flux-related properties for phase α are taken from cell i; if it is negative, from the VE subcell $j^{'}$. All flux-related properties in the VE subcell $j^{'}$ are calculated assuming chemical equilibrium within the subcell, using averaged total concentrations and reconstructed pressures of the subcell from the previous time step. Futhermore, the volume derivative $\left(\frac{\partial \hat{v}}{\partial c^\kappa}\right)^{'}$ is centrally weighted between cells i and $j^{'}$, while $\left(\frac{\partial \hat{v}_j}{\partial c_j^\kappa}\right)^{'}$ is determined specifically for the subcell itself, using averaged properties inside the subcell and a fraction of the transport estimate according to the volume ratio between subcell and VE cell. For each full multidimensional cell there is only one adjacent VE subcell contributing to volume change due to fluxes from the VE subdomain. The volume change caused by fluxes over the subdomain boundary to the VE cell is computed as the sum of the volume changes due to fluxes from all neighboring full multidimensional cells.

5.3.2 Computational algorithm

We solve the pressure and transport equations of the two compositional models sequentially as described in chapter 5.1.1. In a pre-computational step, we calculate a transport estimate on the pressure field of the previous time step to determine the volume derivatives. Then, we first solve the pressure equation in an implicit manner, where the primary unknown variable is one phase pressure for each computational cell,

and all coefficients are calculated based on the previous time level. We use a single computational matrix for the entire domain, combining full multidimensional subdomains (pressure equation (2.22), including (2.10)) and VE subdomains (pressure equation (5.23), including (5.24)) without iterating between subdomains, and consequently solve for all phase pressures simultaneously. The volume change due to mass fluxes at the interface is calculated as shown above, with all adjacent full multidimensional cells taken into account for a VE cell at the subdomain boundary.

Once the pressure has been updated, the full multidimensional transport equations (5.29) and VE transport equations (2.21) are solved explicitly to update total concentrations in each cell. The component fluxes across subdomain boundaries are calculated as the fluxes calculated in the pressure step to determine the volume change due to fluxes. The component flux across the subdomain to a VE cell is calculated as the sum of the component fluxes from full multidimensional cells to subcells of the VE cell, while for a full multidimensional cell only the contribution of the adjacent subcell is taken into account. The scheme is mass conservative since all mass leaving one cell enters the neighboring cell. Once the total concentrations are known, all secondary variables are updated.

5.4 Adaptivity

Applicability of a compositional VE model depends not only on space but also on time. Vertical equilibrium of phases develops with time due to the density difference between the developing gas phase and the resident brine. Furthermore, areas in the domain that are not in equilibrium may change in size and position, depending on local processes like advancing gas-phase plume or geological heterogeneity. Inside the gas-phase plume, chemical equilibrium can be considered to be valid almost instantaneously, whereas chemical equilibrium along the entire depth of the aquifer is reached only after much larger time scales. Therefore, a model that adaptively matches model complexity to system complexity during runtime is needed. To this end, our model identifies during simulation the parts of the domain that are not in equilibrium, and adaptively assigns the compositional full multidimensional model in those parts. Everywhere else, the compositional VE model is used. For that purpose, we develop *a posteriori* criteria for local vertical equilibrium in the context of compositional models in section 5.4.1, and

analyze the behavior of these criteria using a test case of gas storage in section 5.4.2. Lastly, section 5.4.3 presents the adaptive algorithm that assigns subdomains to the compositional VE and full multidimensional model.

5.4.1 Local VE criteria

We develop local *a posteriori* criteria for vertical equilibrium in the context of compositional models. The criteria are based on profiles of saturation and relative-permeability in the vertical direction of each grid column, similar as for the immiscible models. The difference between the simulated profile in a full multidimensional column to a hypothetical VE profile is calculated as the area between the profiles, and normalized with the thickness of the mobile gas-phase plume in the hypothetical VE profile. The equations for the criteria thus have the same form as for the immiscible models:

$$c_{\text{sat}} = \frac{\int_{z_B}^{z_T} \| s_b - s_b^{'} \| dz}{h} \tag{5.54}$$

$$c_{\text{relPerm}} = \frac{\int_{z_B}^{z_T} \| k_{r,b} - k_{r,b}^{'} \| dz}{h}, \tag{5.55}$$

where $s_b^{'}$ and $k_{r,b}^{'}$ are reconstructed values, and h is the thickness of the mobile gas-phase plume in the hypothetical VE profile. The hypothetical VE profiles of saturation are reconstructed as described in chapter 5.2.7, assuming that all gas components inside the full multidimensional grid columns are located in the two-phase region of the gas-phase plume and that the phases in this region are in chemical equilibrium. The hypothetical VE profile of relative permeability is determined based on the hypothetical saturation profile, applying a relationship like, e.g., Brooks-Corey, see equation 2.7. Phase densities and mass fractions are estimated according to the phase pressures in the full multidimensional column at the locations where the reference pressures are evaluated. As a result, the developed criteria are directly associated with phase equilibrium, while chemical equilibrium within the gas-phase plume is indirectly included through the reconstruction, to the degree that chemical equilibrium is relevant for the overall flow behavior. Thus, the criteria can detect if the assumption of chemical equilibrium in the gas-phase plume is violated, e.g., by a large amount of gas components dissolved below the gas-phase plume.

We extend the local criteria to take gas extraction, as well as injection, into account, as required for gas storage scenarios. As the gas-phase plume retreats during gas extraction, it leaves residual gas phase, which is in chemical equilibrium with the surrounding brine, or, in case of zero residual gas saturation, a region of brine with dissolved gas at equilibrium conditions. The minimum location of the gas plume, $z_p^{\min}$, is a parameter that depends on the system's history, which can be viewed as a hysteretic behavior on the coarse scale [Juanes et al., 2010, Doster et al., 2013b,a]. The mobile gas phase above the immobile region may be in equilibrium, which should be reflected by the VE criteria. For this purpose, we store $z_p^{\min}$ for each full multidimensional grid column, as calculated during the reconstruction of the hypothetical VE saturation profile. When extraction happens, the hypothetical VE saturation profile takes the stored $z_p^{\min}$ into account, assigning residual saturation and chemical equilibrium below the mobile gas region. Figure 5.4 shows an example of simulated and hypothetical VE saturation profiles in a full multidimensional column during extraction, as well as the simulated and hypothetical relative permeability profiles.

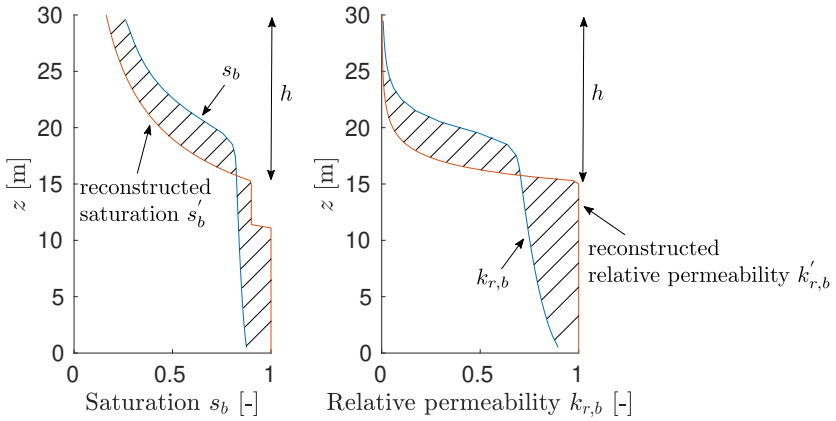

Figure 5.4: Vertical profiles in one column. Left: brine phase saturation with residual phase saturations of $s_{l,r} = 0.0$, $s_{g,r} = 0.1$, right: brine phase relative permeability using a Brooks-Corey relationship with pore size distribution index $\lambda = 2.0$ and entry pressure $p_e = 10^5$ Pa. The blue curve is the result of the full multidimensional solution, and the orange curve is the reconstructed profile that would develop if the fluids were in vertical equilibrium. The difference between profiles is depicted using the striped areas.

5.4.2 Criteria analysis

We analyze the behavior of the two VE criteria over space and time for an injection scenario with CH_4. Gas is injected from the left hand side over the entire thickness (30 m) of an initially brine saturated domain. The conditions are typical for gas storage in 1000 m depth. The temperature is assumed to be constant at 52 °C. Bottom and top of the domain are closed to flow, and Dirichlet conditions are prescribed on the right-hand side with only water components present and a hydrostatic distribution of the brine phase pressure p_b, starting with 1.0×10^7 Pa at the top and assuming a constant brine phase density of 991 kg/m^3 at the boundary. The domain is long enough such that the gas components will not reach the right-hand side boundary during the simulation. We uniformly inject 0.0175 kg/sm CH_4 for the duration of the simulation (240 h). The permeability is assumed to be 2000 mD and the porosity 0.2. We use Brooks-Corey curves for relative permeability and capillary pressure with pore size distribution index $\lambda = 2$ and entry pressure $p_e = 1.0 \times 10^5$ Pa. The residual saturation of the brine phase is zero while the residual saturation of the gas phase is assumed to be 0.1. We use a grid resolution of 1.0 m in horizontal and 1.0 m in vertical direction, and estimate the segregation time as $t_{seg} = 48$ h.

In all subsequent simulations with compositional flow, unless stated otherwise, we use the following equations of state to determine properties like phase density and phase viscosity, and parameters like the Henry coefficient or vapor pressure for the phase equilibrium. We assume local chemical equilibrium in the computational cells of the full multidimensional model and apply a fugacity-based approach as illustrated in section 5.1.3, assuming the ideal mixtures and an ideal gas phase with regard to mixing. Gas and brine phase densities are calculated depending on pressure, temperature and phase composition. Density of the pure gas phase is calculated assuming ideal gas law, density of the pure brine phase is calculated according to the IAPWS formulations [IAPWS, 1997]. The density of the gaseous mixture is calculated assuming an ideal mixture, while the density of the liquid mixture is calculated assuming that one molecule of water component is replaced by one molecule of gas component [Class and Helmig, 2002]. The Henry coefficient for the gas component in brine is calculated depending on temperature according to the IAPWS formulations with coefficients published in Watanabe and Dooley [2004]. The vapor pressure of pure brine is calculated according to the IAPWS formulations as well, depending on temperature. Phase viscosities

depend on temperature and pressure, as well as on composition for the gas phase. Viscosity of the pure gas phase is calculated according to the formulation by Reid et al. [1987], using coefficients published by Poling et al. [2001]. The viscosity of the gaseous mixture is calculated using the Wilke method from Reid et al. [1987]. Viscosity of the brine phase is calculated according to the IAPWS formulation for water [Cooper and Dooley, 2008].

Figure 5.5 shows snapshots of criterion values in the whole domain for three times, and the behavior of criterion values over dimensionless time for two different locations along the horizontal axis. Similar as for our previous injection case with two incompressible,

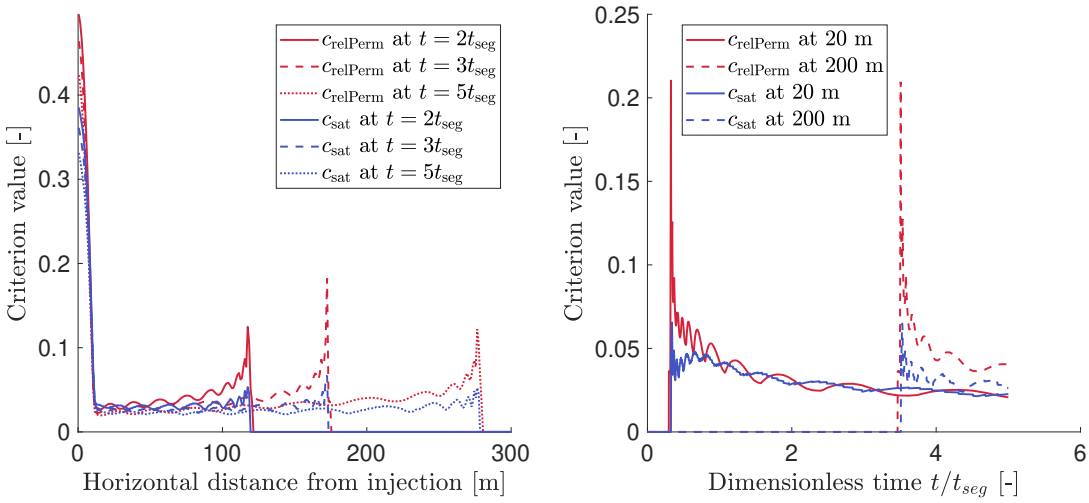

Figure 5.5: Criterion values for the VE criteria based on saturation and relative permeability, respectively. (a) Over the entire length of domain for three times: $2t_{\text{seg}}$, $3t_{\text{seg}}$, and $5t_{\text{seg}}$. (b) Over dimensionless time for a grid column with 20 m distance from the injection location and a grid column with 200 m distance from the injection location. We simulate constant gas injection from the beginning until the end of the simulation.

immiscible phases, the criterion based on relative permeability gives higher values over the length of the domain. Again, this is due to the nonlinearity of the relative permeability function, which results in small saturations of gas phase below the gas-phase plume having a large impact on the criterion based on relative permeability, as opposed to the criterion based on saturation. This is especially the case when the gas-phase plume in equilibrium is small compared to the vertical height of the grid cells. Around the injection region, the criterion values show a high peak, indicating that the phases here are not in equilibrium due to injected gas phase moving continuously upward.

Toward the tip of the gas-phase plume, the criterion values increase, with a much more pronounced peak for the criterion based on relative permeability. This is due to the decreasing height of the gas-phase plume in equilibrium toward the tip, which results in gas phase being located below the gas-phase plume in equilibrium that is being penalized more by the criterion based on relative permeability. Over dimensionless time the criteron values show similar nonmonotone behavior as for the case with two incompressible, immiscible phases. Again, this is due to the finite size of of the cells in the full multidimensional model and loses impact with time and a growing thickness of the gas-phase plume as a result. In a direct comparison of both criteria for our injection case, the criteria based on relative permeability has a clear advantage in that it shows a much more distinct peak at the tip of the gas-phase plume. This makes setting a threshold value ϵ_{crit} easier because the division in subdomains is less dependent on the exact threshold value.

To analyze the behavior of the criteria during extraction, we repeat the same simulation as above, this time including an extraction phase that follows the initial injection phase. After injecting methane for 96 h ($2t_{\text{seg}}$), we uniformly extract methane at the left hand side of the domain over a vertical section of 5 m below the top of the aquifer. We use a constant extraction rate of 0.003 kg/sm CH_4. Figure 5.6 shows that over the length of the domain, extraction leads to a slight increase of criterion values in a region around the tip of the gas-phase plume. This is due to the thickness of the gas-phase plume decreasing, especially toward the tip, causing the criteria to become more sensitive, as they are normalized by the thickness. This effect is more pronounced for the relative permeability criterion, because small gas-phase saturations below the hypothetical gas-phase plume, which are not equal to residual gas phase saturation, have a higher impact on the criterion value than for the saturation criterion. At a fixed location inside the gas-phase plume, the criterion values stay constant over time as soon as extraction starts. This is oppposed to the time prior to extraction and the case without extraction, where the criterion values decrease with time. During extraction, the effect of decreasing thickness of mobile gas-phase plume and the system striving toward vertical equilibrium cancel each other out. For the relative permeability criterion close to the injection/extraction area, where most of the gas is extracted, the criterion value even increases at later times, indicating that here the influence of small gas-phase saturations below the gas-phase plume is dominating.

We note that our compositional VE criteria may show a decrease over time for the

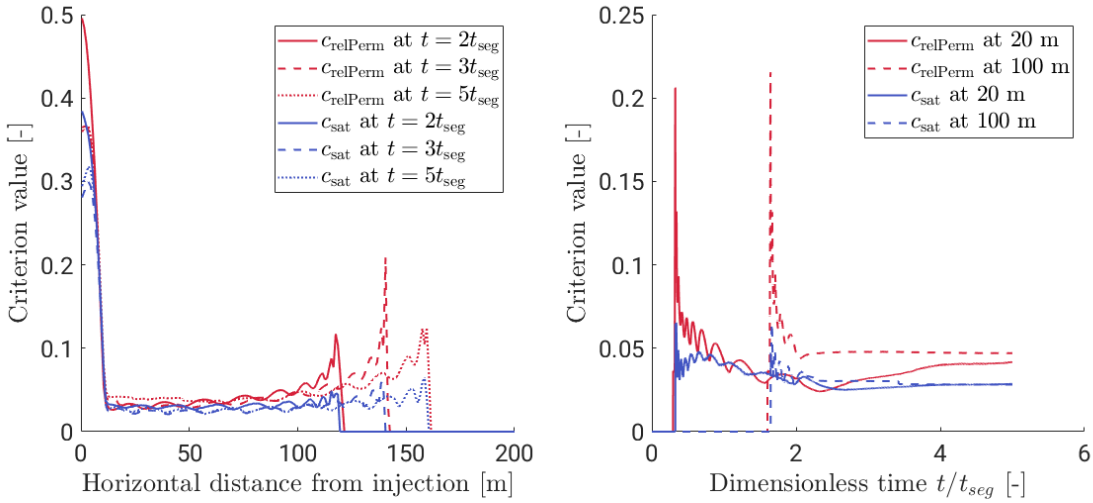

Figure 5.6: Criterion values for the VE criteria based on saturation and relative permeability, respectively. (a) Over the entire length of domain for three times: $2t_{\text{seg}}$, $3t_{\text{seg}}$, and $5t_{\text{seg}}$. (b) Over dimensionless time for a grid column with 20 m distance from the injection/extraction location and a grid column with 100 m distance from the injection/extraction location. We simulate constant gas injection from the beginning of the simulation, and switch to constant gas extraction after $2t_{\text{seg}}$.

injection case, indicating that vertical equilibrium is approached, but we expect the criteria values to increase again after very long time scales. This is the time scale after which the system moves toward chemical equilibrium along the vertical height of the aquifer, and a compositional VE model assuming chemical equilibrium only in the gas-phase plume becomes unsuitable. In this case, gas components dissolving across the large-scale interface between gas-phase plume and brine phase below should be included in the model. This did not become critical in our simulations, mostly because the process of dissolution across this large-scale interface is not accelerated by convective mixing in our full multidimensional model and the effect on the VE criterion is counteracted by the phases striving toward phase equilibrium. Thus, the assumption of chemical equilibrium in the gas-phase plume remains sufficiently valid throughout our simulation times.

5.4.3 Adaptive algorithm

The decision as to which parts of the domain are in vertical equilibrium is made based on the VE criterion chosen, and is evaluated after each time step for all full multidi-

mensional grid columns. A full multidimensional grid column where the VE criterion value is smaller than a threshold ϵ_{crit} is considered to be in vertical equilibrium. As for the immiscible models, the following decision is made for each grid column:

1. A full multidimensional grid column stays full multidimensional if the VE criterion is not met ($c_{\text{crit}} \geq \epsilon_{\text{crit}}$).
2. A full multidimensional grid column is turned into a VE column if the VE criterion is met ($c_{\text{crit}} < \epsilon_{\text{crit}}$), and the column is not a direct neighbor to a column where the criterion is not met.
3. A VE cell is turned into a full multidimensional grid column if it is a direct neighbor to a (full multidimensional) column where the criterion is not met.

The second and third requirement lead to a buffer zone around regions that are not in vertical equilibrium. The buffer cells serve as indicators to turn VE cells back into full multidimensional grid columns, as done by the third requirement. As for the immiscible multiphysics model, the buffer zone can be extended to have more than one layer for stability reasons. As before, we recommend that information that is known beforehand, e.g., injection at a later point in time in another region of the domain, or a fault zone where vertical movement of brine is of interest, be implemented by requiring full multidimensional cells in this region.

5.5 Results and discussion

We test the applicability of the compositional VE model and the compositional multiphysics model using two test cases: gas injection into a horizontal layer, and gas storage in an idealized dome-shape aquifer. While the first test case focuses on primary injection of gas into a previously brine-saturated aquifer, the second test case is concerned with injection and extraction cycles in an initially filled gas storage. We use homogeneous domains and focus on the influence of compositional processes. The compositional multiphysics model, the compositional VE model and the compositional full multidimensional model are all implemented in DuMu$^{\text{x}}$ [Flemisch et al., 2011, Koch

et al., 2020], allowing for a comparison of the different methods within the same software framework. The code to produce the results presented here can be obtained from https://git.iws.uni-stuttgart.de/dumux-pub/Becker2021a.git.

5.5.1 Gas injection into a horizontal layer

We use the same gas injection scenario (CH_4, no extraction) that was used for the criteria analysis to compare results from the adaptive multiphysics model with a threshold value of 0.03, a compositional VE model, and a compositional full multidimensional model. We uniformly inject 0.0175 kg/sm CH_4 over the left boundary of the domain for the duration of the simulation (180 h) and assume the residual saturations of both phases to be zero. We use a grid resolution of 1.0 m in horizontal and (in the full multidimensional model and full multidimensional subdomain) 0.23 m in vertical direction. The segregation time is again $t_{seg} = 48$ h.

The gas phase distribution after 180 h in figure 5.7 shows that the VE model overestimates the length of the plume, while the adaptive multiphysics model shows a much better comparison to the full multidimensional model. In particular the injection re-

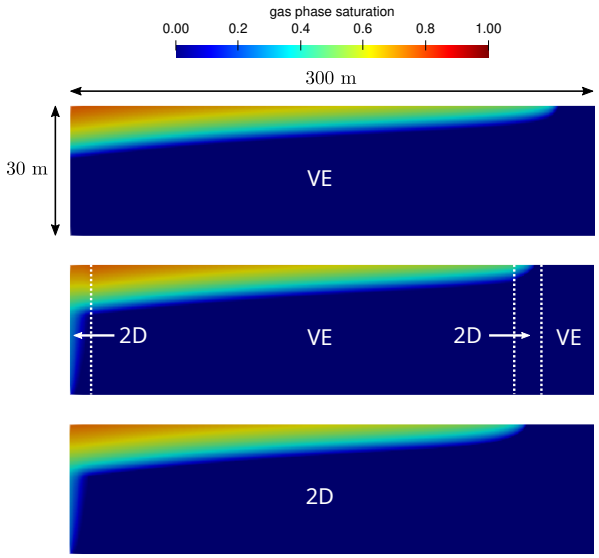

Figure 5.7: Gas phase distribution for the full VE model (top), the adaptive multiphysics model with a threshold value of 0.03 (middle), and full multidimensional model (bottom). Subdomain boundaries are marked by dotted lines, indicating full multidimensional subdomains around the injection area and the tip of the gas-phase plume, and VE subdomains everywhere else. The simulation time is $t = 180$ h.

gion cannot be represented accurately by the VE model, because gas is continuously injected over the vertical length of the aquifer and the phases thus are not in vertical equilibrium. This causes also a discrepancy between models when comparing the total mass of dissolved gas components in the domain, as in figure 5.8. The full multidimen-

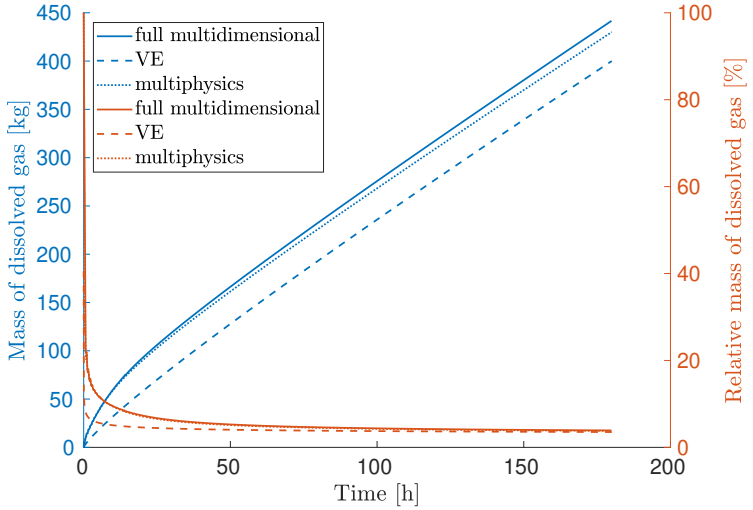

Figure 5.8: Absolute and relative (to total mass of gas components) mass of dissolved gas components in entire domain over simulated time for full multidimensional model (solid line), full VE model (dashed line), and adaptive multiphysics model with a threshold value of 0.03 (dotted line)

sional model and the adaptive multiphysics model show a strong increase of dissolved gas components in the beginning of the simulation. When gas is injected into a fully brine-saturated aquifer, it first dissolves into brine until equilibrium concentration is reached. Since we inject over the entire vertical direction of the aquifer, this effect is rather strong. Only then a separate gas phase forms, and moves upward due to buoancy. This process is not captured by the VE model, which assumes from the beginning that most gas has formed a separate phase and moved to pool below the top of the aquifer. In later times, the total mass of dissolved gas components mostly increases linearly in all models due to the advancing plume, which increases the gas-phase plume where both phases are in chemical equilibrium. All dissolved gas components in the VE model are located inside this two-phase region, while the full multidimensional model can also account for gas components dissolving below the gas-phase plume, i.e., due to dissolution across the large-scale interface. This explains the slight discrepancy that develops between a full multidimensional and an adaptive multiphysics model in later times. In terms of computational time, the VE model is the fastest model, using only

0.6 % of the CPU time of the full multidimensional model. The adaptive multiphysics model, being much more accurate than the VE model, is still fast, with 15 % relative CPU time.

5.5.2 Gas storage in an idealized underground aquifer

We simulate hydrogen storage in a radial symmetric anticline structure in 1700 m depth. The temperature is assumed to be a constant 52 °C. We simulate sandstone with a permeability of 22 mD and a porosity of 0.13. The aquifer is discretized into a radially symmetric grid with horizontal resolution of 5 m and vertical resolution of 0.94 m (for full multidimensional and multiphysics model). Initially, the aquifer is filled with hydrogen under hydrostatic conditions, as shown in figure 5.9.

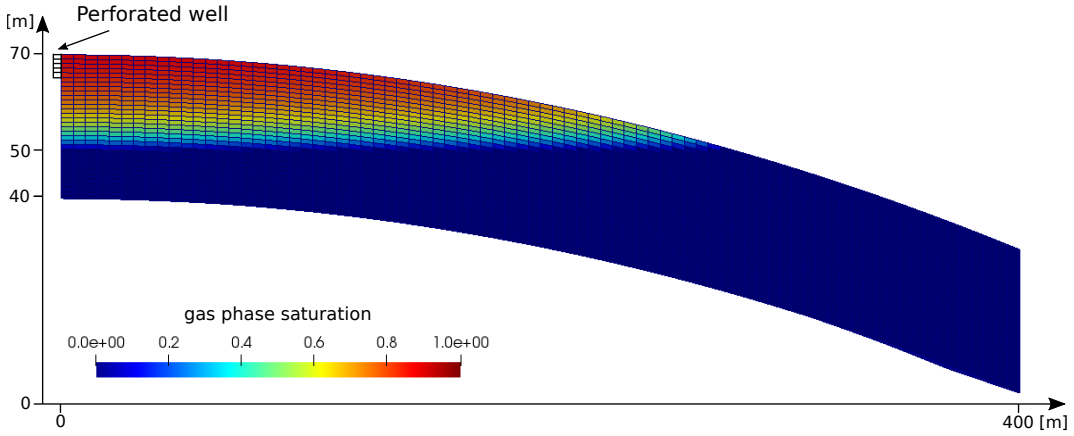

Figure 5.9: Initial gas phase distribution in an idealized underground aquifer. The aquifer is filled under hydrostatic conditions, with the capillary transition zone starting at 50 m height. The perforation of the injection/extraction well in the top 5 m of the aquifer is marked.

Hydrogen is injected and extracted through a large-diameter well (0.53 m), which is perforated in the top 5 m of the aquifer. The top and the bottom of the aquifer are closed to flow, and on the far side of the well we prescribe a Dirichlet boundary condition with only water components present and a hydrostatic distribution of the brine phase pressure p_b, starting with 1.7×10^7 Pa at the top and assuming a constant brine phase density of 994 kg/m^3 at the boundary. We use Brooks-Corey curves for relative permeability and capillary pressure with pore size distribution index $\lambda = 2$ and entry

pressure $p_e = 1 \times 10^5$ Pa. The residual saturation of the brine is zero while the residual saturation of the gas phase is assumed to be 0.1.

Instead of largely assuming hydrogen to act as an ideal gas, we use thermodynamic properties for hydrogen that are based on the Perturbed-Chain Statistical Associating Fluid Theory (PC-SAFT) [Gross and Sadowski, 2002]. The PC-SAFT equation of state was correlated to experimental data and can be used to calculate density, phase equilibrium and entropy. The latter served as input to an entropy scaling approach, resulting in transport properties like, e.g., viscosity. Sauerborn [2021] showed that correct treatment of density and viscosity of hydrogen has an influence on pressure development close to the injection point of a hydrogen storage aquifer. Therefore, in the following, density and viscosity of hydrogen, as well as phase equilibrium, are calculated based on the PC-SAFT equation of state. For water, the highly specialized and verified IAPWS formulations [IAPWS, 1997] are used as illustrated before.

The operation of the subsurface storage is split in two parts. During a 12-month injection-only period, we inject 0.134 kg/s H_2 for one month, followed by three idle months, repeated three times. During the operation period, 0.083 kg/s H_2 are injected for three months, followed by extration of 0.083 kg/s H_2 for three months, for a total of three years. Figure 5.10 shows the injection rate, the total mass of injected gas since the start of the simulation, and the bottom hole pressure, for the full multidimensional simulation. The pressure response during the injection-only phase shows that because of the open boundary on the far side of the well, the pressure buildup due to injection is lost within approximately one month of idle time.

We compare results to a full VE model and the multiphysics model with a threshold value for the relative permeability criterion of 0.09. Figure 5.11 shows total concentration of gas components for all three models after the last injection during injection-only phase and after the last extraction during operation phase. All three models are in very good agreement considering plume length and shape farther away from the well. The full VE model predicts a different plume shape in the vicinity of the well than the other two models, with a larger plume height after injection and a smaller plume height after extraction directly at the well. Figure 5.12 compares pressures in the computational cell directly at the bottom of the well, composition and saturation of gas phase in the computational cell directly at the bottom of the well, and total mass of dissolved gas components in the domain for all three models. In terms of pressure and composition,

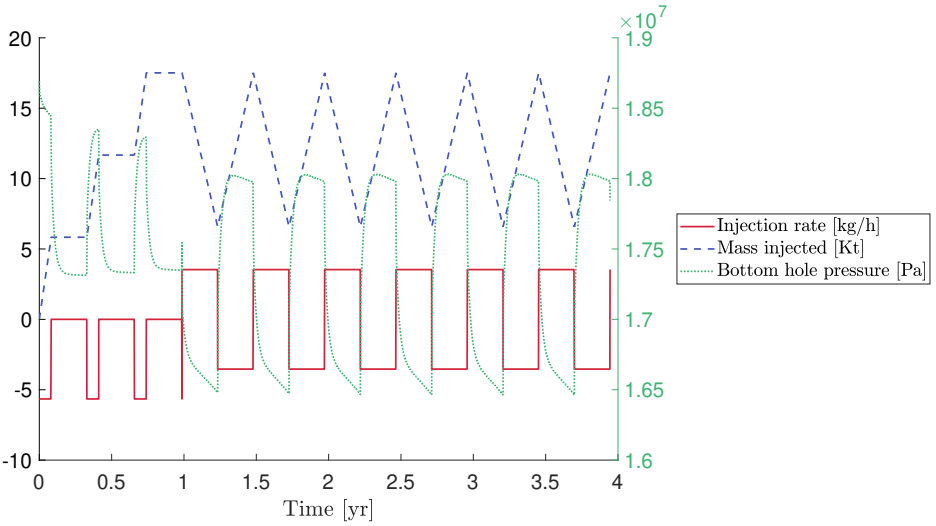

Figure 5.10: Injection rate, total mass of injected gas and bottom hole pressure for a full multidimensional simulation. We inject hydrogen into a radial symmetric anticline structure, previously filled with hydrogen and brine at equilibrium.

the multiphysics model compares very well to the full multidimensional model close to the well. The VE model slightly underestimates the pressure increase in the domain close to the well, due to assuming hydrostatic pressure distribution in the vertical direction, which is violated in the area close to the well. As a direct effect of the pressure deviating at that location, the VE model slightly overestimates the mass fraction of water components in the gas phase during injection. The gas phase saturation close to the well is captured equally well by the full multidimensional and the multiphysics model, while the VE model shows strong deviations because the gas and brine phase are not in equilibrium near the well. We note that hybrid numerical-analytical models exist, which use a VE model on the coarse scale coupled to a local analytical well model in the vicinity of the well [Nordbotten and Celia, 2006b, Gasda et al., 2009]. These coupled models include local corrections for both the pressure field and the location of the sharp interface in the overall coarse-scale model, which results in a high accuracy close to the well compared to full multidimensional models [Class et al., 2009]. However, the models currently rely on several simplifications allowing for the application of analytical solutions near the well, including, e.g., a sharp interface assumption, locally homogeneous and horizontal formation, and locally incompressible, immiscible phases.

Both the VE model and the multiphysics model underestimate the total mass of dissolved gas components predicted by the full multidimensional model. In general, this

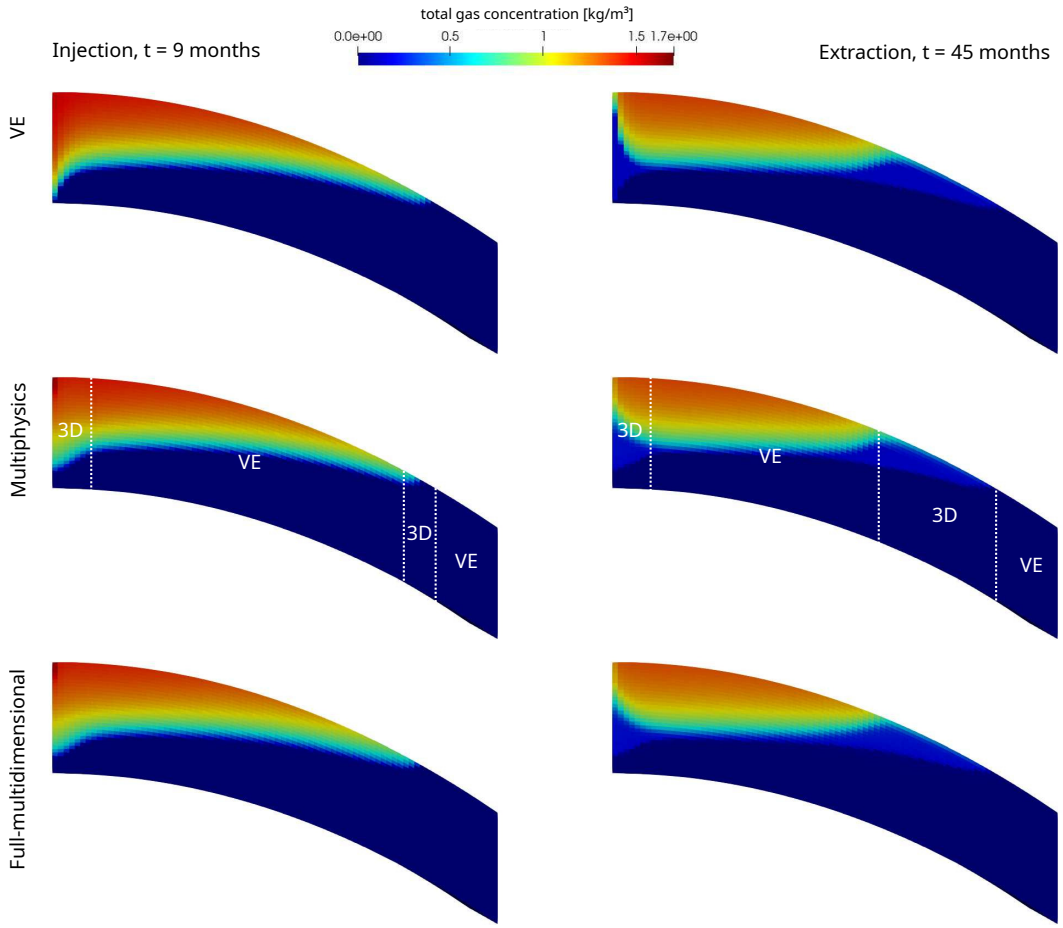

Figure 5.11: Total concentration of gas components after the last injection during injection-only phase (after 9 simulated months) and after the last extraction during operation phase (after 45 simulated months). Shown are results from full VE model (top), adaptive multiphysics model with a threshold value of 0.09 (middle), and full multidimensional model (bottom). Subdomain boundaries are marked by dotted lines, indicating full multidimensional subdomains around the injection/extraction area and the tip of the gas-phase plume, and VE subdomains everywhere else.

may be due to assuming one reference pressure in the gas-phase plume to approximate equilibrium conditions. This reference pressure is chosen as the gas phase pressure at the top of the aquifer, i.e., the smallest gas phase pressure along the vertical direction. It may also be due to a very small smearing of the gas phase along the vertical direction in the full multidimensional model, which leads to more gas components dissolving into brine. Both arguments explain the differences that can be observed already during the initial state at $t = 0$. However, the overall trend of the full multidimensional model

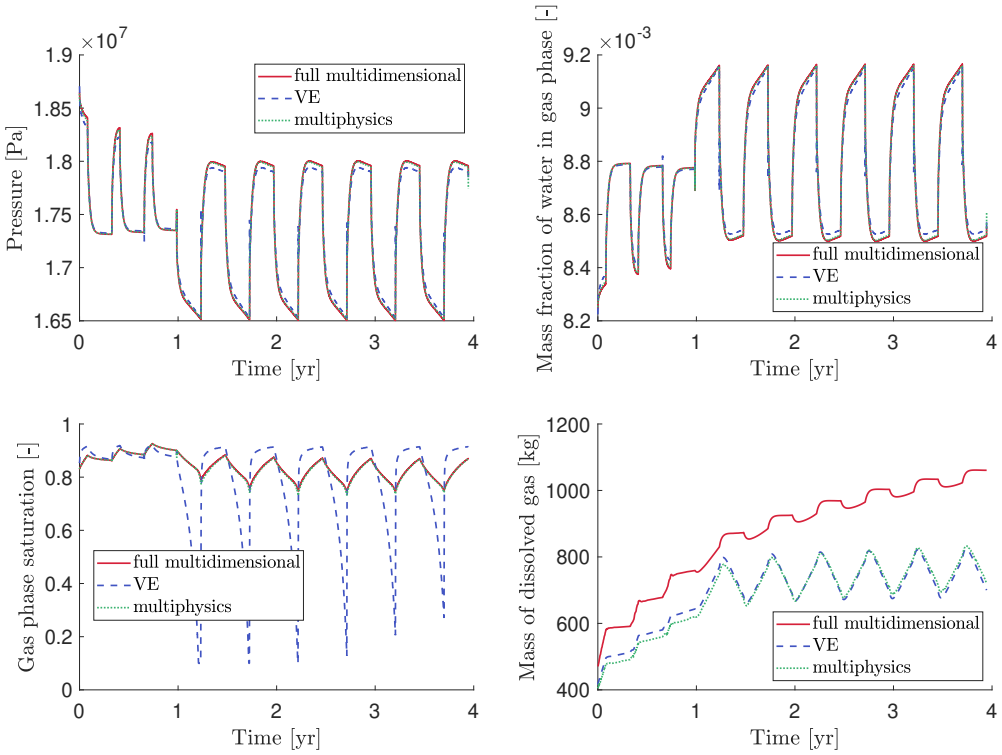

Figure 5.12: Gas phase pressure in the computational cell directly at the bottom of the well (top left), mass fraction of water components in the gas phase in the computational cell directly at the bottom of the well (top right), gas phase saturation in the computational cell directly at the bottom of the well (bottom left), and total mass of dissolved gas components in the domain (bottom right) for full multidimensional model (solid line), full VE model (dashed line), and adaptive multiphysics model with a threshold value of 0.09 (dotted line).

shows an increase of the mass of total dissolved gas components over time, while the multiphysics model and the VE model predict no overall increase. A closer inspection of the location of gas phase and the distribution of gas components in the domain of the full multidimensional model show that the gas plume (i.e., total concentration of gas components larger than zero) extends much beyond the gas phase itself, already after the first injection. Moreover, during idle and extraction phases, the gas components dissolved in brine do not retreat as quickly toward the upper boundary or the extraction well as the much lighter and more mobile gas phase, which results in an overall growing gas plume with time. We note that the transport of gas components away from the gas-phase plume can be observed even though our full multidimensional model neglects diffusion, and there is no convective mixing due to gas components

dissolving into brine, which would further accelerate the process. Since our VE model assumes gas to be present only in the gas-phase plume, the full VE model and the VE subdomains fail to reproduce this behavior. However, since H_2 has a comparably low miscibility, the difference in total mass of dissolved gas components computed by the full multidimensional model and the multiphysics model at the end of the simulation only makes up 0.8% of the total mass of gas components in the aquifer.

The threshold value of 0.09 for the relative permeability VE criterion was chosen as explained previously in chapter 4 by starting with a higher value which is reduced until a stable solution is reached. Since the domain is homogeneous and the aquifer already filled at the beginning, this requires only a few steps and short simulation times. In average during the simulation, 26% of the domain are assigned as full multidimensional subdomains. As a result of the relatively high ratio between VE and full multidimensional subdomains, and due to the lower resolution in the vertical direction in full multidimensional subdomains compared to the horizontal injection case, the multiphysics model uses 21% of the CPU time compared to the full multidimensional model. The full VE model uses 1.9%. Since the efficiency of the multiphysics model is directly related to the ratio of VE subdomain area to full multidimensional subdomain area, we expect the multiphysics model to become even more favorable in the case of real scenarios, where large parts of the domain are either one-phase regions or occupied by the gas-phase plume in vertical equilibrium.

5.6 Conclusion

In this chapter we have developed a compositional VE model by vertically integrating the transport equation and volume balance equation of the compositional full multidimensional model. Our rigorously derived compositional VE model includes compressibility, assuming constant pressure-dependent parameters in the vertical direction within the plume and below, as well as lateral transport due to density differences, and can apply a sharp interface or a capillary transition zone. We have extended the definition of vertical equilibrium beyond equilibrium of phases to include compositional processes as well, and use a compositional VE assumption in our model that assumes phase equilibrium along the vertical direction and chemical equilibrium within the gas-phase plume only. Further, we have developed an adaptive multiphysics model that

couples a compositional full multidimensional model to a compositional VE model. The coupling is realized in a monolithic framework. We couple the models across the subdomain boundaries by using variables in the full multidimensional boundary cells and reconstructed fine-scale variables in the VE boundary subcells to compute the flux-induced volume change in the boundary cells. The unknown variables in the VE subcells are expressed as fine-scale reconstructions of the VE cell variables using the compositional VE assumption. The volume balance and transport equations are solved sequentially with an IMPET algorithm, where we solve the pressure implicitly for the entire domain. The subdomains are assigned adaptively during simulation, and models are chosen based on a local *a posteriori* criterion for compositional vertical equilibrium. This criterion compares computed and reconstructed vertical profiles of saturation or relative permeability in the grid columns, and stores the minimum location of the gas plume of the aquifer to account for the residual part of the gas-phase plume which develops during re-imbibition.

The compositional multiphysics model showed excellent accuracy in predicting the overall gas distribution, composition and pressure development especially near the well with a lower number of computational cells and consequently lower computational cost compared to a full multidimensional model. The compositional VE model showed good accuracy in predicting the overall gas-plume development compared to a full multidimensional model. If highly miscible gases are of interest, dissolution below the gas-phase plume could be included in the VE model and VE subdomains. However, our results show that assuming chemical equilibrium within the gas-phase plume and neglecting dissolution below the gas-phase plume is a reasonable choice for our targeted gases CH_4 and H_2. As a result, the multiphysics model is an efficient tool for modeling underground energy storage with a localized focus on gas phase saturation and composition.

6 Summary and Outlook

6.1 Summary

This thesis presents a set of computational models that focus on the application of large-scale energy storage in form of gas injection and storage in the subsurface. Three models of different complexity are developed, as summarized in the following.

Chapter 3 introduces a group of simplified models which exploit the VE assumption to reduce model complexity by vertical integration of the governing equations. The chapter is concerned with slow gravity drainage due to nonlinear relative permeability relationships, which would render classical VE models unsuitable even after long time scales. A modified VE model is presented that assumes a pseudo-segregated state with a pseudo-residual brine phase saturation higher than the ultimate brine phase saturation inside the plume, and continuously updates the pseudo-residual saturation during the simulation. The pseudo-residual brine phase saturation can be a single variable which is updated for the entire plume, or it can be spatially dependent and updated individually for each VE cell, solving simple explicit equations. This results in two pseudo-VE models that preserve much of the computational advantage of classical VE models. We show that the pseudo-VE models are applicable for a wide range of injection scenarios, including situations involving slow drainage dynamics, and that they can provide accurate results early on. This makes the pseudo-VE models very attractive in the context of energy storage, when large domains and long time scales are involved, or many computational runs are necessary due to a high degree of parameter uncertainty.

Chapter 4 combines the individual benefits of VE models and full multidimensional models by developing a framework to couple both models in one domain. The subdomains are adaptively identified by a local VE criterion during the simulation, matching

model complexity to process complexity. The optimal threshold parameter defining the sensitivity of subdomain selection can be found by following a procedure similar to finding the optimal grid size, starting from a very high ratio of VE subdomain to full multidimensional subdomain and decreasing the ratio until a stable solution is reached. We show the multiphysics model to be much more computationally efficient than using the full multidimensional model in the entire domain, while maintaining much of the accuracy. The multiphysics model is very favorable especially on large domains involving local heterogeneities or areas of interest, e.g., the injection/extraction well or a fault zone, where the accurate description of vertical dynamics is of high importance.

While the previous chapters deal with immiscible two-phase flow, chapter 5 takes the VE concept and the multiphysics framework and applies it to compositional processes. A novel compositional VE model is developed by vertically integrating the full multidimensional compositional governing equations. The compositional VE model is then adapatively coupled to the compositional full multidimensional model. Subdomains are assigned during simulation according to a local criterion that decides if the assumption of compositional vertical equilibrium is valid. We show that the compositional multiphysics model is computationally efficient and very accurately reproduces the results of the full multidimensional model. Consequently, the compositional multiphysics model is very convenient to model cases of energy storage on large domains with a specific local interest in both vertical dynamics and gas composition, e.g., in the vicinity of the well.

The three presented models can be used to address a wide range of questions arising from an increased demand for energy storage, such as gas storage in the underground. The models efficiently handle large domains with high data uncertainty, as associated with the screening of potential storage sites and risk assessment, and cover (locally) complex flow behavior and advanced physics for planning, development and operation of storage sites. As a result, the developed models make an important contribution to help integrate renewable energy into the electricity system, scale up the share of synthetic gases, and decarbonize our society.

6.2 Outlook

We can combine the three models developed and analyzed in this thesis to further increase applicability. The pseudo-VE model can be combined with the multiphysics model by assuming a pseudo-segregated state within VE subdomains. In the case of nonlinear relative permeability relationships, this would allow full multidimensional subdomains to switch to VE subdomains earlier. In addition, the full multidimensional subdomain can be used to determine pseudo-residual brine phase saturation for the pseudo-VE subdomains, e.g., to approximate initial values for the local pseudo-VE model, which could further increase accuracy. The local VE criteria need to be adapted accordingly, assuming a pseudo-segregated state which is updated during simulation.

For more miscible gases than the ones investigated in this thesis, e.g., CO_2 as cushion gas, dissolution below the gas-phase plume can be added to the compositional VE model and included in the VE subdomains of the compositional multiphysics model. In this context, the compositional multiphysics model can be extended in a similar way as the immiscible multiphysics model, by retreiving information from the full multidimensional subdomains and using it in the VE subdomains. The amount of gas dissolved in the brine phase below the gas-phase plume could be determined from the full multidimensional subdomains of the multiphysics model, once the fluid phases are segregated. From then on, a VE model with improved initial conditions could be used farther away from the injection area. This would be particularly beneficial in situations with convective mixing, to better determine the onset time of convection.

Furthermore, the immiscible and compositional multiphysics models can be combined to form a model hierarchy consisting of four models: two immiscible models, and two compositional models, with a full multidimensional and a VE version, respectively. The compositional multiphase model could be used in a subdomain in the vicinity of the well, while farther away from the well the compositional VE model, or immiscible VE model could be used, depending on, e.g., miscibility of the gas. In areas where the vertical movement of brine may be of interest, e.g., at a fault zone, the immiscible full multidimensional model could be used. This would further increase efficiency of the model by better matching model complexity to process complexity. An algorithm for model selection and suitable criteria need to be developed for this multiphysics model.

In this thesis we assume the upper boundary of the aquifer to be impermeable. However,

for a comprehensive risk assessment of underground energy storage the domain can be extended to include the geological layers above the storage aquifer, and determine leakage of gas to higher layers which may be used, e.g., as drinking water reservoirs. This would necessitate the coupling of VE models and full multidimensional models in the vertical direction in addition to the horizontal direction, as demonstrated by Guo et al. [2016a] and Møyner and Nilsen [2019]. Since gas which continuously leaks into upper geological layers with a low permeability may not be in vertical equilibrium for a very long time, an additional model could be included in the hierarchy, which acts as an intermediate between VE and full multidimensional models. A suitable option could be the dynamic reconstruction model developed by Guo et al. [2014], which updates vertical saturation profiles by computing fine-scale one-dimensional solutions inside each column after solving the coarse-scale equations.

We show accuracy and practical applicability of the multiphysics models on suitable gas injection and storage scenarios, targeting real applications. A rigorous mathematical analysis of the multiphysics and VE models was not within the scope of this thesis. However, it could lead to new insights on coupling error and yield *a posteriori* error estimators, which could be used for model selection in addition to the model-based estimators presented and analyzed in this thesis. Similarly, data-based criteria could be developed, utilizing observational data to decide if vertical equilibrium has been reached at a specific location and a specific time. Together with the model-based or mathematically derived criteria they could help define an optimal model selection for predictive simulations of real gas storage scenarios. The mathematical analysis and the data-driven approach are currently under investigation in the tandem project *Data-driven optimisation algorithms for local dynamic model adaptivity* supported by the Cluster of Excellence SimTech EXC 2075.

A Appendix

A.1 Determination of fugacity coefficients

The following section is based on Atkins and de Paula [2010] and Gmehling et al. [2019].

If two phases are in equilibrium, their chemical potentials are equal. This implies that the fugacities f_α^κ of a component κ in each of those phases are the same:

$$f_\alpha^\kappa = f_\beta^\kappa. \tag{A.1}$$

Based on this, one can derive the following equilibrium equation for one liquid and one gas phase:

$$x_l^\kappa \gamma^\kappa \varphi_{vap}^\kappa p_{vap}^\kappa \exp(...) = \varphi_g^\kappa x_g^\kappa p_g, \tag{A.2}$$

where γ^κ is the activity coefficient of component κ, φ_{vap}^κ is the fugacity coefficient of the pure component κ, p_{vap}^κ is the vapor pressure of the pure component κ and exp(...) is an exponential term called the Poynting Factor. For low pressures $\frac{\varphi_{vap}^\kappa}{\varphi_g^\kappa} = 1$, and for ideal mixtures the activity coefficient and Poynting Factor equal 1. This leads to the simplification:

$$x_l^\kappa p_{vap}^\kappa = x_g^\kappa p_g, \tag{A.3}$$

which is valid for the main component of the liquid phase (Raoult's law: $p_g^\kappa = p_{vap}^\kappa x_l^\kappa$). Another simplification uses Henry's law ($H^\kappa = \frac{p_g^\kappa}{x_l^\kappa}$) and is valid for the main component of the gas phase:

$$x_l^\kappa H^\kappa = x_g^\kappa p_g. \tag{A.4}$$

Defining fugacities as $f_\alpha^\kappa = x_\alpha^\kappa \varphi_\alpha^\kappa p_\alpha$, the fugacity coefficients leading to the simplifica-

tions above are:

$$\varphi_g^{\kappa} = 1, \tag{A.5}$$

$$\varphi_l^{\mathrm{mainL}} = \frac{p_{vap}^{\mathrm{mainL}}}{p_l}, \tag{A.6}$$

$$\varphi_l^{\mathrm{mainG}} = \frac{H^{\mathrm{mainG}}}{p_l}. \tag{A.7}$$

A.2 Derivation of Rachford-Rice equation

Following the derivation in Fritz [2010], we can write per definition of mass equilibrium ratios for a reference phase r:

$$X_{\alpha}^{\kappa} = K_{\alpha}^{\kappa} X_r^{\kappa}. \tag{A.8}$$

The feed mass fraction z^{κ} can be written in terms of a reference phase r, and using the definition of mass equilibrium ratios, as:

$$z^{\kappa} = \sum_{\alpha} \nu_{\alpha} X_{\alpha}^{\kappa} = \nu_r X_r^{\kappa} + \sum_{\alpha \neq r} \nu_{\alpha} K_{\alpha}^{\kappa} X_r^{\kappa} = X_r^{\kappa} \left(\nu_r + \sum_{\alpha \neq r} \nu_{\alpha} K_{\alpha}^{\kappa} \right). \tag{A.9}$$

Rearranging for X_r^{κ} gives:

$$X_r^{\kappa} = \frac{z^{\kappa}}{\nu_r + \sum_{\alpha \neq r} \nu_{\alpha} K_{\alpha}^{\kappa}}. \tag{A.10}$$

Inserting equation (A.10) into equation (A.8) leads to:

$$X_{\alpha}^{\kappa} = K_{\alpha}^{\kappa} \frac{z^{\kappa}}{\nu_r + \sum_{\alpha \neq r} \nu_{\alpha} K_{\alpha}^{\kappa}}. \tag{A.11}$$

The mass fractions in each phase sum up to unity. Therefore, we can write:

$$\sum_{\kappa} X_{\alpha}^{\kappa} - \sum_{\kappa} X_r^{\kappa} = 0, \tag{A.12}$$

and inserting equations (A.10) and (A.11) leads to:

$$\sum_{\kappa} \frac{(K_{\alpha}^{\kappa} - 1) z^{\kappa}}{\nu_r + \sum_{\alpha \neq r} \nu_{\alpha} K_{\alpha}^{\kappa}} = 0. \tag{A.13}$$

The phase mass fractions sum up to unity:

$$\sum_{\alpha} \nu_\alpha = \nu_r + \sum_{\alpha \neq r} \nu_\alpha = 1. \tag{A.14}$$

Rearranging for ν_r and inserting into equation (A.13) finally gives the Rachford-Rice equation:

$$\sum_{\kappa} \frac{(K_\alpha^\kappa - 1) z^\kappa}{1 + \sum_{\alpha \neq r} \nu_\alpha (K_\alpha^\kappa - 1)} = 0 \tag{A.15}$$

Bibliography

G. Acs, S. Doleschall, and E. Farkas. General purpose compositional model. *Society of Petroleum Engineers Journal*, 25(04):543–553, 1985. doi: 10.2118/10515-PA.

A. Armiti-Juber and C. Rohde. On Darcy-and Brinkman-type models for two-phase flow in asymptotically flat domains. *Computational Geosciences*, 23(2):285–303, 2019. doi: 10.1007/s10596-018-9756-2.

P. Atkins and J. de Paula. *Atkins' Physical Chemistry*. Oxford University Press, 2010. ISBN 9780199543373.

S. Bachu. Sequestration of CO_2 in geological media in response to climate change: road map for site selection using the transform of the geological space into the CO_2 phase space. *Energy Conversion and Management*, 43(1):87–102, 2002. doi: 10.1016/S0196-8904(01)00009-7.

K. W. Bandilla and M. A. Celia. Active pressure management through brine production for basin-wide deployment of geologic carbon sequestration. *International Journal of Greenhouse Gas Control*, 61:155 – 167, 2017. doi: 10.1016/j.ijggc.2017.03.030.

K. W. Bandilla, M. A. Celia, T. R. Elliot, M. Person, K. M. Ellett, J. A. Rupp, C. Gable, and Y. Zhang. Modeling carbon sequestration in the Illinois basin using a vertically-integrated approach. *Computing and Visualization in Science*, 15(1):39–51, 2012. doi: 10.1007/s00791-013-0195-2.

K. W. Bandilla, M. A. Celia, and E. Leister. Impact of model complexity on CO_2 plume modeling at Sleipner. *Energy Procedia*, 63:3405–3415, 2014. doi: 10.1016/j.egypro.2014.11.369.

E. Barbour, D. Mignard, Y. Ding, and Y. Li. Adiabatic compressed air energy storage with packed bed thermal energy storage. *Applied Energy*, 155:804–815, 2015. doi: 10.1016/j.apenergy.2015.06.019.

S. Bauer, C. Beyer, F. Dethlefsen, P. Dietrich, R. Duttmann, M. Ebert, V. Feeser, U. Görke, R. Köber, O. Kolditz, W. Rabbel, T. Schanz, D. Schäfer, H. Würdemann, and A. Dahmke. Impacts of the use of the geological subsurface for energy storage: an investigation concept. *Environmental Earth Sciences*, 70:3935–3943, 2013. doi: 10.1007/s12665-013-2883-0.

J. Bear. *Dynamics of fluids in porous media*. Dover Civil and Mechanical Engineering Series, 1972. ISBN 780486656755.

B. Becker, B. Guo, K. Bandilla, M. A. Celia, B. Flemisch, and R. Helmig. A pseudo-vertical equilibrium model for slow gravity drainage dynamics. *Water Resources Research*, 53(12):10491–10507, 2017. doi: 10.1002/2017WR021644.

B. Becker, B. Guo, K. Bandilla, M. A. Celia, B. Flemisch, and R. Helmig. An adaptive multiphysics model coupling vertical equilibrium and full multidimensions for multiphase flow in porous media. *Water Resources Research*, 54(7):4347–4360, 2018. doi: 10.1029/2017WR022303.

F. B. Belgacem. The mortar finite element method with Lagrange multipliers. *Numerische Mathematik*, 84(2):173–197, 1999. doi: 10.1007/s002110050468.

K. Benisch and S. Bauer. Short-and long-term regional pressure build-up during CO_2 injection and its applicability for site monitoring. *International Journal of Greenhouse Gas Control*, 19:220–233, 2013. doi: 10.1016/j.ijggc.2013.09.002.

C. Bernardi, Y. Maday, and A. T. Patera. A new nonconforming approach to domain decomposition: The mortar element method. In *Nonlinear Partial Differential Equations and Their Applications, Collège de France Seminar*. Pitman, 1994.

J. T. Birkholzer, Q. Zhou, and C.-F. Tsang. Large-scale impact of CO_2 storage in deep saline aquifers: A sensitivity study on pressure response in stratified systems. *International Journal of Greenhouse Gas Control*, 3(2):181–194, 2009. doi: 10.1016/j.ijggc.2008.08.002.

M. Bonte, P. J. Stuyfzand, A. Hulsmann, and P. Van Beelen. Underground thermal energy storage: environmental risks and policy developments in the Netherlands and European Union. *Ecology and Society*, 16(1), 2011. doi: 10.5751/ES-03762-160122.

M. Bonte, B. M. Van Breukelen, and P. J. Stuyfzand. Environmental impacts of aquifer thermal energy storage investigated by field and laboratory experiments. *Journal of water and climate change*, 4(2):77–89, 2013. doi: 10.2166/wcc.2013.061.

R. Brooks and A. Corey. Hydraulic properties of porous media. *Hydrology Papers, Colorado State University*, 1964.

M. Celia, S. Bachu, J. Nordbotten, and K. Bandilla. Status of CO_2 storage in deep saline aquifers with emphasis on modeling approaches and practical simulations. *Water Resources Research*, 51(9):6846–6892, 2015. doi: 10.1002/2015WR017609.

H. Class and R. Helmig. Numerical simulation of nonisothermal multiphase multicomponent processes in porous media – 2. Applications for the injection of steam and air. *Advances in Water Resources*, 25:551–564, 2002. doi: 10.1016/S0309-1708(02)00015-5.

H. Class, A. Ebigbo, R. Helmig, H. K. Dahle, J. M. Nordbotten, M. A. Celia, P. Audigane, M. Darcis, J. Ennis-King, Y. Fan, et al. A benchmark study on problems related to CO_2 storage in geologic formations. *Computational Geosciences*, 13(4):409, 2009. doi: 10.1007/s10596-009-9146-x.

K. Coats. A note on IMPES and some IMPES-based simulation models. *SPE Journal - SPE J*, 5:245–251, 09 2000. doi: 10.2118/65092-PA.

J. R. Cooper and R. B. Dooley. Release of the IAPWS formulation 2008 for the viscosity of ordinary water substance, 2008. URL http://www.iapws.org/relguide/visc.pdf.

R. Courant, K. Friedrichs, and H. Lewy. Über die partiellen Differenzengleichungen der mathematischen Physik. *Mathematische Annalen*, 100:32–74, 1928. doi: 10.1007/BF01448839.

B. Court, K. W. Bandilla, M. A. Celia, A. J. Janzen, M. Dobossy, and J. M. Nordbotten. Applicability of vertical-equilibrium and sharp-interface assumptions in CO_2 sequestration modeling. *International Journal of Greenhouse Gas Control*, 10:134–147, 2012. doi: 10.1016/j.ijggc.2012.04.015.

H. Darcy. *Les fontaines publiques de la ville de Dijon: exposition et application...* Victor Dalmont, 1856.

P. Denholm, E. Ela, B. Kirby, and M. Milligan. Role of energy storage with renewable electricity generation. Technical report, National Renewable Energy Laboratory (NREL), Golden, CO (United States), 2010.

M. Dentz and D. M. Tartakovsky. Abrupt-interface solution for carbon dioxide injection into porous media. *Transport in Porous Media*, 79(1):15, 2009. doi: 10.1007/s11242-008-9268-y.

F. Doster, J. Nordbotten, and M. Celia. Impact of capillary hysteresis and trapping on vertically integrated models for CO_2 storage. *Advances in Water Resources*, 62: 465–474, 2013a. doi: 10.1016/j.advwatres.2013.09.005.

F. Doster, J. Nordbotten, and M. Celia. Hysteretic upscaled constitutive relationships for vertically integrated porous media flow. *Computing and Visualization in Science*, 15, 08 2013b. doi: 10.1007/s00791-013-0206-3.

J. Ennis-King and L. Paterson. Role of convective mixing in the long-term storage of carbon dioxide in deep saline formations. *Society of Petroleum Engineers Journal*, 10:349–356, 2005. doi: 10.2118/84344-PA.

D. Evans. An appraisal of underground gas storage technologies and incidents, for the development of risk assessment methodology. Technical report, British Geological Survey, 2007.

R. P. Ewing, B. Ghanbarian, and A. G. Hunt. Gradients and assumptions affect interpretation of laboratory-measured gas-phase transport. *Soil Science Society of America Journal*, 79(4):1018–1029, 2015. doi: 10.2136/sssaj2014.09.0391.

B. Faigle, M. A. Elfeel, R. Helmig, B. Becker, B. Flemisch, and S. Geiger. Multi-physics modeling of non-isothermal compositional flow on adaptive grids. *Computer Methods in Applied Mechanics and Engineering*, 292:16–34, 2015. doi: 10.1016/j.cma.2014.11.030.

R. Farajzadeh, H. Salimi, P. L. Zitha, and H. Bruining. Numerical simulation of density-driven natural convection in porous media with application for CO_2 injection projects.

International Journal of Heat and Mass Transfer, 50(25):5054–5064, 2007. doi: 10.1016/j.ijheatmasstransfer.2007.08.019.

B. Flemisch, M. Darcis, K. Erbertseder, B. Faigle, A. Lauser, K. Mosthaf, S. Müthing, P. Nuske, A. Tatomir, M. Wolff, and R. Helmig. DuMu^x: DUNE for multi-{phase, component, scale, physics, . . .} flow and transport in porous media. *Advances in Water Resources*, 34(9):1102–1112, 2011. doi: 10.1016/j.advwatres.2011.03.007.

J. Fritz. *A decoupled model for compositional non-isothermal multiphase flow in porous media and multiphysics approaches for two-phase flow.* Phd thesis, University of Stuttgart, 2010.

J. Fritz, B. Flemisch, and R. Helmig. Decoupled and multiphysics models for non-isothermal compositional two-phase flow in porous media. *International Journal of Numerical Analysis & Modeling*, 9(1), 2012.

S. Gasda, J. Nordbotten, and M. Celia. Vertically averaged approaches for CO_2 migration with solubility trapping. *Water Resources Research*, 47(5), 2011a. doi: 10.1029/2010WR009075.

S. E. Gasda, J. M. Nordbotten, and M. A. Celia. Vertical equilibrium with sub-scale analytical methods for geological CO_2 sequestration. *Computational Geosciences*, 13 (4):469, 2009. doi: 10.1007/s10596-009-9138-x.

S. E. Gasda, J. M. Nordbotten, and M. A. Celia. The impact of local-scale processes on large-scale CO_2 migration and immobilization. *Energy Procedia*, 4:3896–3903, 2011b. doi: 10.1016/j.egypro.2011.02.327.

S. E. Gasda, J. M. Nordbotten, and M. A. Celia. Application of simplified models to CO_2 migration and immobilization in large-scale geological systems. *International Journal of Greenhouse Gas Control*, 9:72–84, 2012. doi: 10.1016/j.ijggc.2012.03.001.

J. Gmehling, M. Kleiber, B. Kolbe, and J. Rarey. *Chemical thermodynamics for process simulation.* John Wiley & Sons, 2019. ISBN 978-3-527-34325-6.

M. J. Golding, J. A. Neufeld, M. A. Hesse, and H. E. Huppert. Two-phase gravity currents in porous media. *Journal of Fluid Mechanics*, 678:248–270, 2011. doi: 10.1017/jfm.2011.110.

J. Gross and G. Sadowski. Application of the perturbed-chain saft equation of state to associating systems. *Industrial & engineering chemistry research*, 41(22):5510–5515, 2002. doi: 10.1021/ie010954d.

B. Guo, K. W. Bandilla, F. Doster, E. Keilegavlen, and M. A. Celia. A vertically integrated model with vertical dynamics for CO_2 storage. *Water Resources Research*, 50(8):6269–6284, 2014. doi: 10.1002/2013WR015215.

B. Guo, K. W. Bandilla, J. M. Nordbotten, M. A. Celia, E. Keilegavlen, and F. Doster. A multiscale multilayer vertically integrated model with vertical dynamics for CO_2 sequestration in layered geological formations. *Water Resources Research*, 52(8): 6490–6505, 2016a. doi: 10.1002/2016WR018714.

B. Guo, Z. Zheng, M. A. Celia, and H. A. Stone. Axisymmetric flows from fluid injection into a confined porous medium. *Physics of Fluids*, 28(2):022107, 2016b. doi: 10.1063/1.4941400.

H. Hajibeygi, M. B. Olivares, M. HosseiniMehr, S. Pop, and M. Wheeler. A benchmark study of the multiscale and homogenization methods for fully implicit multiphase flow simulations. *Advances in Water Resources*, 143:103674, 2020. doi: 10.1016/j.advwatres.2020.103674.

R. Helmig. *Multiphase flow and transport processes in the subsurface: a contribution to the modeling of hydrosystems.* Springer-Verlag, 1997. ISBN 978-3-642-64545-7.

R. Helmig, J. Niessner, B. Flemisch, M. Wolff, and J. Fritz. Efficient modeling of flow and transport in porous media using multiphysics and multiscale approaches. In W. Freeden, M. Z. Nashed, and T. Sonar, editors, *Handbook of Geomathematics*, pages 417–457. Springer Berlin Heidelberg, Berlin, Heidelberg, 2010. ISBN 978-3-642-01546-5. doi: 10.1007/978-3-642-01546-5_15.

R. Helmig, B. Flemisch, M. Wolff, A. Ebigbo, and H. Class. Model coupling for multiphase flow in porous media. *Advances in Water Resources*, 51:52–66, 2013. doi: 10.1016/j.advwatres.2012.07.003.

M. Hesse, H. Tchelepi, B. Cantwel, and F. Orr. Gravity currents in horizontal porous layers: transition from early to late self-similarity. *Journal of Fluid Mechanics*, 577: 363–383, 2007. doi: 10.1017/S0022112007004685.

A. Hunt, R. Ewing, and B. Ghanbarian-Alavijeh. *Percolation theory for flow in porous media*, volume 880 of *Lecture Notes in Physics*. Springer, 2013. ISBN 978-3-540-32405-8.

H. E. Huppert and A. W. Woods. Gravity-driven flows in porous layers. *Journal of Fluid Mechanics*, 292(1):55, 1995. doi: 10.1017/S0022112095001431.

IAPWS. Revised release on the IAPWS industrial formulation 1997 for the thermodynamic properties of water and steam, 1997. URL http://www.iapws.org/relguide/IF97-Rev.pdf.

IEA. *The role of CCUS in low-carbon power systems*. IEA, 2020a.

IEA. *Renewable Power*. IEA, 2020b.

IPCC. *Climate Change 2014: Synthesis Report. Contribution of Working Groups I, II and III to the Fifth Assessment Report of the Intergovernmental Panel on Climate Change*. IPCC, 2014. Core Writing Team, R.K. Pachauri and L.A. Meyer (eds.).

R. Juanes, C. W. MacMinn, and M. L. Szulczewski. The footprint of the CO_2 plume during carbon dioxide storage in saline aquifers: Storage efficiency for capillary trapping at the basin scale. *Transport in Porous Media*, 82(1):19–30, 2010. doi: 10.1007/s11242-009-9420-3.

P. Kanakasabapathy. Economic impact of pumped storage power plant on social welfare of electricity market. *International Journal of Electrical Power & Energy Systems*, 45(1):187–193, 2013. doi: 10.1016/j.ijepes.2012.08.056.

V. Kippe, J. E. Aarnes, and K.-A. Lie. A comparison of multiscale methods for elliptic problems in porous media flow. *Computational Geosciences*, 12(3):377–398, 2008. doi: 10.1007/s10596-007-9074-6.

T. Koch, D. Gläser, K. Weishaupt, S. Ackermann, M. Beck, B. Becker, S. Burbulla, H. Class, E. Coltman, S. Emmert, T. Fetzer, C. Grüninger, K. Heck, J. Hommel, T. Kurz, M. Lipp, F. Mohammadi, S. Scherrer, M. Schneider, G. Seitz, L. Stadler, M. Utz, F. Weinhardt, and B. Flemisch. DuMu^x 3 – an open-source simulator for solving flow and transport problems in porous media with a focus on model coupling. *Computers & Mathematics with Applications*, 2020. doi: 10.1016/j.camwa.2020.02.012.

L. W. Lake. *Enhanced oil recovery*. Prentice Hall Englewood Cliffs, 1989. ISBN 9780132816014.

P. S. Laplace. Supplément au dixième livre du traité de mécanique céleste. *Traité de Mécanique Céleste*, 4:1–79, 1806.

I. Ligaarden and H. Nilsen. Numerical aspects of using vertical equilibrium models for simulating CO_2 sequestration. In *ECMOR XII-12th European Conference on the Mathematics of Oil Recovery*, 2010. doi: 10.3997/2214-4609.20145011.

E. Lindeberg and P. Bergmo. The long-term fate of CO_2 injected into an aquifer. In J. Gale and Y. Kaya, editors, *Greenhouse Gas Control Technologies - 6th International Conference*, pages 489–494. Pergamon, Oxford, 2003. ISBN 978-0-08-044276-1. doi: 10.1016/B978-008044276-1/50078-7.

S. Lyle, H. E. Huppert, M. Hallworth, M. Bickle, and A. Chadwick. Axisymmetric gravity currents in a porous medium. *Journal of Fluid Mechanics*, 543:293–302, 2005. doi: 10.1017/S0022112005006713.

C. R. Matos, J. F. Carneiro, and P. P. Silva. Overview of large-scale underground energy storage technologies for integration of renewable energies and criteria for reservoir identification. *Journal of Energy Storage*, 21:241–258, 2019. doi: 10.1016/j.est.2018.11.023.

O. Møyner and H. M. Nilsen. Multiresolution coupled vertical equilibrium model for fast flexible simulation of CO_2 storage. *Computational Geosciences*, 23(1):1–20, 2019. doi: 10.1007/s10596-018-9775-z.

O. Møyner, O. Andersen, and H. M. Nilsen. Multi-model hybrid compositional simulator with application to segregated flow. *Computational Geosciences*, pages 1–13, 2020. doi: 10.1007/s10596-019-09910-y.

H. M. Nilsen, P. A. Herrera, M. Ashraf, I. Ligaarden, M. Iding, C. Hermanrud, K.-A. Lie, J. M. Nordbotten, H. K. Dahle, and E. Keilegavlen. Field-case simulation of CO_2-plume migration using vertical-equilibrium models. *Energy Procedia*, 4:3801–3808, 2011. doi: 10.1016/j.egypro.2011.02.315.

H. M. Nilsen, K.-A. Lie, and O. Andersen. Fully-implicit simulation of vertical-equilibrium models with hysteresis and capillary fringe. *Computational Geosciences*, 20(1):49–67, 2016a. doi: 10.1007/s10596-015-9547-y.

H. M. Nilsen, K.-A. Lie, and O. Andersen. Robust simulation of sharp-interface models for fast estimation of CO_2 trapping capacity in large-scale aquifer systems. *Computational Geosciences*, 20(1):93–113, 2016b. doi: 10.1007/s10596-015-9549-9.

J. Nordbotten, B. Flemisch, S. Gasda, H. Nilsen, Y. Fan, G. Pickup, B. Wiese, M. Celia, H. Dahle, G. Eigestad, and K. Pruess. Uncertainties in practical simulation of CO_2 storage. *International Journal of Greenhouse Gas Control*, 9:234 – 242, 2012. ISSN 1750-5836. doi: 10.1016/j.ijggc.2012.03.007.

J. M. Nordbotten and M. A. Celia. Similarity solutions for fluid injection into confined aquifers. *Journal of Fluid Mechanics*, 561:307–327, 2006a. doi: 10.1017/S0022112006000802.

J. M. Nordbotten and M. A. Celia. An improved analytical solution for interface upconing around a well. *Water Resources Research*, 42(8), 2006b. doi: 10.1029/2005WR004738.

J. M. Nordbotten and M. A. Celia. *Geological storage of CO_2: modeling approaches for large-scale simulation*. John Wiley & Sons, 2011. ISBN 978-0-470-88946-6.

J. M. Nordbotten and H. K. Dahle. Impact of the capillary fringe in vertically integrated models for CO_2 storage. *Water Resources Research*, 47(2), 2011. doi: 10.1029/2009WR008958.

G. S. Pau, J. B. Bell, K. Pruess, A. S. Almgren, M. J. Lijewski, and K. Zhang. High-resolution simulation and characterization of density-driven flow in CO_2 storage in saline aquifers. *Advances in Water Resources*, 33(4):443 – 455, 2010. doi: 10.1016/j.advwatres.2010.01.009.

G. S. H. Pau, J. B. Bell, A. S. Almgren, K. M. Fagnan, and M. J. Lijewski. An adaptive mesh refinement algorithm for compressible two-phase flow in porous media. *Computational Geosciences*, 16(3):577–592, 2012. doi: 10.1007/s10596-011-9270-2.

S. S. Pegler, H. E. Huppert, and J. A. Neufeld. Fluid injection into a confined porous layer. *Journal of Fluid Mechanics*, 745:592–620, 2014. doi: 10.1017/jfm.2014.76.

M. Person, A. Banerjee, J. Rupp, C. Medina, P. Lichtner, C. Gable, R. Pawar, M. Celia, J. McIntosh, and V. Bense. Assessment of basin-scale hydrologic impacts of CO_2 sequestration, Illinois basin. *International Journal of Greenhouse Gas Control*, 4(5): 840–854, 2010. doi: 10.1016/j.ijggc.2010.04.004.

M. Peszyńska, Q. Lu, and M. F. Wheeler. Multiphysics coupling of codes. In *Computational Methods in Water Resources*, pages 175–182. A. A. Balkema, 2000.

B. E. Poling, J. M. Prausnitz, and J. P. O'Connell. *The properties of gases and liquids*, volume 5. McGraw-Hill, 2001. ISBN 9780071189712.

K. Pruess and K. Zhang. Numerical modeling studies of the dissolution-diffusion-convection process during CO_2 storage in saline aquifers. Technical report, Lawrence Berkeley National Laboratory (LBNL), Berkeley, CA, USA, 2008.

H. H. Rachford Jr. and J. D. Rice. Procedure for use of electronic digital computers in calculating flash vaporization hydrocarbon equilibrium. *Journal of Petroleum Technology*, 4(10):19–3, 1952. doi: 10.2118/952327-G.

R. C. Reid, J. Prausnitz, and B. E. Poling. *The Properties of Gases and Liquids*, volume 4. McGraw-Hill, 1987. ISBN 0070517991.

A. Riaz and M. Hesse. Onset of convection in a gravitationally unstable diffusive boundary layer in porous media. *Journal of Fluid Mechanics*, 548:87–111, 2006. doi: 10.1017/S0022112005007494.

M. Sahimi. *Flow and transport in porous media and fractured rock: from classical methods to modern approaches*. John Wiley & Sons, 2011. ISBN 978-3-527-40485-8.

T. Sauerborn. Transport properties from entropy scaling using PC-SAFT equation of state for the modelling of subsurface hydrogen storage. Master's thesis, University of Stuttgart, 2021.

G. Singh, W. Leung, and M. F. Wheeler. Multiscale methods for model order reduction of non-linear multiphase flow problems. *Computational Geosciences*, 23(2):305–323, 2019. doi: 10.1007/s10596-018-9798-5.

B. B. S. Singhal and R. P. Gupta. *Applied hydrogeology of fractured rocks*, volume 2. Springer Science & Business Media, 2010. ISBN 978-90-481-8798-0.

M. J. Swickrath, S. Mishra, and P. Ravi Ganesh. An evaluation of sharp interface models for CO_2-brine displacement in aquifers. *Groundwater*, 54(3):336–344, 2016. doi: 10.1111/gwat.12366.

P. Tomin and I. Lunati. Hybrid multiscale finite volume method for two-phase flow in porous media. *Journal of Computational Physics*, 250:293–307, 2013. doi: 10.1016/j.jcp.2013.05.019.

J. A. Trangenstein and J. B. Bell. Mathematical structure of compositional reservoir simulation. *SIAM journal on scientific and statistical computing*, 10(5):817–845, 1989. doi: 10.1137/0910049.

UNFCCC. *Report of the Conference of the Parties on its sixteenth session, held in Cancun from 29 November to 10 December 2010. Part Two: Action taken by the Conference of the Parties at its sixteenth session.* UNFCCC, 2010.

D. E. Van Odyck, J. B. Bell, F. Monmont, and N. Nikiforakis. The mathematical structure of multiphase thermal models of flow in porous media. *Proceedings of the Royal Society A: Mathematical, Physical and Engineering Sciences*, 465(2102): 523–549, 2009. doi: 10.1098/rspa.2008.0268.

K. Watanabe and R. B. Dooley. Guideline on the Henry's Constant and Vapor-Liquid Distribution Constant for Gases in H_2O and D_2O at High Temperatures, 2004. URL http://www.iapws.org/relguide/HenGuide.pdf.

J. Watts. A compositional formulation of the pressure and saturation equations. *Society of Petroleum Engineers Reservoir Engineering*, 1(03):243–252, 1986. doi: 10.2118/12244-PA.

M. F. Wheeler and M. Peszyńska. Computational engineering and science methodologies for modeling and simulation of subsurface applications. *Advances in Water Resources*, 25(8-12):1147–1173, 2002. doi: 10.1016/S0309-1708(02)00105-7.

J. A. White, N. Castelletto, and H. A. Tchelepi. Block-partitioned solvers for coupled poromechanics: A unified framework. *Computer Methods in Applied Mechanics and Engineering*, 303:55–74, 2016. doi: 10.1016/j.cma.2016.01.008.

Y. Yortsos. A theoretical analysis of vertical flow equilibrium. *Transport in Porous Media*, 18(2):107–129, 1995. doi: 10.1007/BF01064674.

T. Young. III. An essay on the cohesion of fluids. *Philosophical Transactions of the Royal Society of London*, 95:65–87, 1805.

M. Yousefzadeh and I. Battiato. Physics-based hybrid method for multiscale transport in porous media. *Journal of Computational Physics*, 344:320 – 338, 2017. doi: 10.1016/j.jcp.2017.04.055.

Z. Zheng, B. Guo, I. C. Christov, M. A. Celia, and H. A. Stone. Flow regimes for fluid injection into a confined porous medium. *Journal of Fluid Mechanics*, 767:881–909, 2015. doi: 10.1017/jfm.2015.68.

Q. Zhou and J. T. Birkholzer. On scale and magnitude of pressure build-up induced by large-scale geologic storage of CO_2. *Greenhouse Gases: Science and Technology*, 1(1):11–20, 2011. doi: 10.1002/ghg3.1.

Institut für Wasser- und Umweltsystemmodellierung
Universität Stuttgart

Pfaffenwaldring 61
70569 Stuttgart (Vaihingen)
Telefon (0711) 685 - 60156
Telefax (0711) 685 - 51073
E-Mail: iws@iws.uni-stuttgart.de
http://www.iws.uni-stuttgart.de

Direktoren
Prof. Dr. rer. nat. Dr.-Ing. András Bárdossy
Prof. Dr.-Ing. Rainer Helmig
Prof. Dr.-Ing. Wolfgang Nowak
Prof. Dr.-Ing. Silke Wieprecht

Vorstand *(Stand 21.05.2021)*
Prof. Dr. rer. nat. Dr.-Ing. A. Bárdossy
Prof. Dr.-Ing. R. Helmig
Prof. Dr.-Ing. W. Nowak
Prof. Dr.-Ing. S. Wieprecht
Prof. Dr. J.A. Sander Huisman
Jürgen Braun, PhD
apl. Prof. Dr.-Ing. H. Class
PD Dr.-Ing. Claus Haslauer
Stefan Haun, PhD
apl. Prof. Dr.-Ing. Sergey Oladyshkin
Dr. rer. nat. J. Seidel
Dr.-Ing. K. Terheiden

Emeriti
Prof. Dr.-Ing. habil. Dr.-Ing. E.h. Jürgen Giesecke
Prof. Dr.h.c. Dr.-Ing. E.h. Helmut Kobus, PhD

Lehrstuhl für Wasserbau und Wassermengenwirtschaft
Leiterin: Prof. Dr.-Ing. Silke Wieprecht
Stellv.: Dr.-Ing. Kristina Terheiden
Versuchsanstalt für Wasserbau
Leiter: Stefan Haun, PhD

Lehrstuhl für Hydromechanik und Hydrosystemmodellierung
Leiter: Prof. Dr.-Ing. Rainer Helmig
Stellv.: apl. Prof. Dr.-Ing. Holger Class

Lehrstuhl für Hydrologie und Geohydrologie
Leiter: Prof. Dr. rer. nat. Dr.-Ing. András Bárdossy
Stellv.: Dr. rer. nat. Jochen Seidel
Hydrogeophysik der Vadosen Zone
(mit Forschungszentrum Jülich)
Leiter: Prof. Dr. J.A. Sander Huisman

Lehrstuhl für Stochastische Simulation und Sicherheitsforschung für Hydrosysteme
Leiter: Prof. Dr.-Ing. Wolfgang Nowak
Stellv.: apl. Prof. Dr.-Ing. Sergey Oladyshkin

***VEGAS,* Versuchseinrichtung zur Grundwasser- und Altlastensanierung**
Leiter: Jürgen Braun, PhD
PD Dr.-Ing. Claus Haslauer

Verzeichnis der Mitteilungshefte

1 Röhnisch, Arthur: *Die Bemühungen um eine Wasserbauliche Versuchsanstalt an der Technischen Hochschule Stuttgart*, und
Fattah Abouleid, Abdel: *Beitrag zur Berechnung einer in lockeren Sand gerammten, zweifach verankerten Spundwand*, 1963

2 Marotz, Günter: *Beitrag zur Frage der Standfestigkeit von dichten Asphaltbelägen im Großwasserbau*, 1964

3 Gurr, Siegfried: *Beitrag zur Berechnung zusammengesetzter ebener Flächentrag-werke unter besonderer Berücksichtigung ebener Stauwände, mit Hilfe von Rand-wert- und Lastwertmatrizen*, 1965

4 Plica, Peter: *Ein Beitrag zur Anwendung von Schalenkonstruktionen im Stahlwasserbau*, und
Petrikat, Kurt: *Möglichkeiten und Grenzen des wasserbaulichen Versuchswesens*, 1966

5 Plate, Erich: *Beitrag zur Bestimmung der Windgeschwindigkeitsverteilung in der durch eine Wand gestörten bodennahen Luftschicht*, und
Röhnisch, Arthur; Marotz, Günter: *Neue Baustoffe und Bauausführungen für den Schutz der Böschungen und der Sohle von Kanälen, Flüssen und Häfen; Gestehungskosten und jeweilige Vorteile*, sowie
Unny, T.E.: *Schwingungsuntersuchungen am Kegelstrahlschieber*, 1967

6 Seiler, Erich: *Die Ermittlung des Anlagenwertes der bundeseigenen Binnenschiffahrtsstraßen und Talsperren und des Anteils der Binnenschiffahrt an diesem Wert*, 1967

7 *Sonderheft anläßlich des 65. Geburtstages von Prof. Arthur Röhnisch mit Beiträgen von* Benk, Dieter; Breitling, J.; Gurr, Siegfried; Haberhauer, Robert; Honekamp, Hermann; Kuz, Klaus Dieter; Marotz, Günter; Mayer-Vorfelder, Hans-Jörg; Miller, Rudolf; Plate, Erich J.; Radomski, Helge; Schwarz, Helmut; Vollmer, Ernst; Wildenhahn, Eberhard; 1967

8 Jumikis, Alfred: *Beitrag zur experimentellen Untersuchung des Wassernachschubs in einem gefrierenden Boden und die Beurteilung der Ergebnisse*, 1968

9 Marotz, Günter: *Technische Grundlagen einer Wasserspeicherung im natürlichen Untergrund*, 1968

10 Radomski, Helge: *Untersuchungen über den Einfluß der Querschnittsform wellenförmiger Spundwände auf die statischen und rammtechnischen Eigenschaften*, 1968

11 Schwarz, Helmut: *Die Grenztragfähigkeit des Baugrundes bei Einwirkung vertikal gezogener Ankerplatten als zweidimensionales Bruchproblem*, 1969

12 Erbel, Klaus: *Ein Beitrag zur Untersuchung der Metamorphose von Mittelgebirgsschneedecken unter besonderer Berücksichtigung eines Verfahrens zur Bestimmung der thermischen Schneequalität*, 1969

13 Westhaus, Karl-Heinz: *Der Strukturwandel in der Binnenschiffahrt und sein Einfluß auf den Ausbau der Binnenschiffskanäle*, 1969

14 Mayer-Vorfelder, Hans-Jörg: *Ein Beitrag zur Berechnung des Erdwiderstandes unter Ansatz der logarithmischen Spirale als Gleitflächenfunktion*, 1970

15 Schulz, Manfred: *Berechnung des räumlichen Erddruckes auf die Wandung kreiszylindrischer Körper*, 1970

16 Mobasseri, Manoutschehr: *Die Rippenstützmauer. Konstruktion und Grenzen ihrer Standsicherheit*, 1970

17 Benk, Dieter: *Ein Beitrag zum Betrieb und zur Bemessung von Hochwasserrückhaltebecken*, 1970

18 Gàl, Attila: *Bestimmung der mitschwingenden Wassermasse bei überströmten Fischbauchklappen mit kreiszylindrischem Staublech*, 1971, vergriffen

19 Kuz, Klaus Dieter: *Ein Beitrag zur Frage des Einsetzens von Kavitationserscheinungen in einer Düsenströmung bei Berücksichtigung der im Wasser gelösten Gase*, 1971, vergriffen

20 Schaak, Hartmut: *Verteilleitungen von Wasserkraftanlagen*, 1971

21 *Sonderheft zur Eröffnung der neuen Versuchsanstalt des Instituts für Wasserbau der Universität Stuttgart mit Beiträgen von* Brombach, Hansjörg; Dirksen, Wolfram; Gàl, Attila; Gerlach, Reinhard; Giesecke, Jürgen; Holthoff, Franz-Josef; Kuz, Klaus Dieter; Marotz, Günter; Minor, Hans-Erwin; Petrikat, Kurt; Röhnisch, Arthur; Rueff, Helge; Schwarz, Helmut; Vollmer, Ernst; Wildenhahn, Eberhard; 1972

22 Wang, Chung-su: *Ein Beitrag zur Berechnung der Schwingungen an Kegelstrahlschiebern*, 1972

23 Mayer-Vorfelder, Hans-Jörg: *Erdwiderstandsbeiwerte nach dem Ohde-Variationsverfahren*, 1972

24 Minor, Hans-Erwin: *Beitrag zur Bestimmung der Schwingungsanfachungsfunktionen überströmter Stauklappen*, 1972, vergriffen

25 Brombach, Hansjörg: *Untersuchung strömungsmechanischer Elemente (Fluidik) und die Möglichkeit der Anwendung von Wirbelkammerelementen im Wasserbau*, 1972, vergriffen

26 Wildenhahn, Eberhard: *Beitrag zur Berechnung von Horizontalfilterbrunnen*, 1972

27 Steinlein, Helmut: *Die Eliminierung der Schwebstoffe aus Flußwasser zum Zweck der unterirdischen Wasserspeicherung, gezeigt am Beispiel der Iller*, 1972

28 Holthoff, Franz Josef: *Die Überwindung großer Hubhöhen in der Binnenschiffahrt durch Schwimmerhebewerke*, 1973

29 Röder, Karl: *Einwirkungen aus Baugrundbewegungen auf trog- und kastenförmige Konstruktionen des Wasser- und Tunnelbaues*, 1973

30 Kretschmer, Heinz: *Die Bemessung von Bogenstaumauern in Abhängigkeit von der Talform*, 1973

31 Honekamp, Hermann: *Beitrag zur Berechnung der Montage von Unterwasserpipelines*, 1973

32 Giesecke, Jürgen: *Die Wirbelkammertriode als neuartiges Steuerorgan im Wasserbau*, und Brombach, Hansjörg: *Entwicklung, Bauformen, Wirkungsweise und Steuereigenschaften von Wirbelkammerverstärkern*, 1974

33 Rueff, Helge: *Untersuchung der schwingungserregenden Kräfte an zwei hintereinander angeordneten Tiefschützen unter besonderer Berücksichtigung von Kavitation*, 1974

34 Röhnisch, Arthur: *Einpreßversuche mit Zementmörtel für Spannbeton - Vergleich der Ergebnisse von Modellversuchen mit Ausführungen in Hüllwellrohren*, 1975

35 *Sonderheft anläßlich des 65. Geburtstages von Prof. Dr.-Ing. Kurt Petrikat mit Beiträgen von*: Brombach, Hansjörg; Erbel, Klaus; Flinspach, Dieter; Fischer jr., Richard; Gàl, Attila; Gerlach, Reinhard; Giesecke, Jürgen; Haberhauer, Robert; Hafner Edzard; Hausenblas, Bernhard; Horlacher, Hans-Burkhard; Hutarew, Andreas; Knoll, Manfred; Krummet, Ralph; Marotz, Günter; Merkle, Theodor; Miller, Christoph; Minor, Hans-Erwin; Neumayer, Hans; Rao, Syamala; Rath, Paul; Rueff, Helge; Ruppert, Jürgen; Schwarz, Wolfgang; Topal-Gökceli, Mehmet; Vollmer, Ernst; Wang, Chung-su; Weber, Hans-Georg; 1975

36 Berger, Jochum: *Beitrag zur Berechnung des Spannungszustandes in rotationssymmetrisch belasteten Kugelschalen veränderlicher Wandstärke unter Gas- und Flüssigkeitsdruck durch Integration schwach singulärer Differentialgleichungen*, 1975

37 Dirksen, Wolfram: *Berechnung instationärer Abflußvorgänge in gestauten Gerinnen mittels Differenzenverfahren und die Anwendung auf Hochwasserrückhaltebecken*, 1976

38 Horlacher, Hans-Burkhard: *Berechnung instationärer Temperatur- und Wärmespannungsfelder in langen mehrschichtigen Hohlzylindern*, 1976

39 Hafner, Edzard: *Untersuchung der hydrodynamischen Kräfte auf Baukörper im Tiefwasserbereich des Meeres*, 1977, ISBN 3-921694-39-6

40 Ruppert, Jürgen: *Über den Axialwirbelkammerverstärker für den Einsatz im Wasserbau*, 1977, ISBN 3-921694-40-X

41 Hutarew, Andreas: *Beitrag zur Beeinflußbarkeit des Sauerstoffgehalts in Fließgewässern an Abstürzen und Wehren*, 1977, ISBN 3-921694-41-8, *vergriffen*

42 Miller, Christoph: *Ein Beitrag zur Bestimmung der schwingungserregenden Kräfte an unterströmten Wehren*, 1977, ISBN 3-921694-42-6

43 Schwarz, Wolfgang: *Druckstoßberechnung unter Berücksichtigung der Radial- und Längsverschiebungen der Rohrwandung*, 1978, ISBN 3-921694-43-4

44 Kinzelbach, Wolfgang: *Numerische Untersuchungen über den optimalen Einsatz variabler Kühlsysteme einer Kraftwerkskette am Beispiel Oberrhein*, 1978, ISBN 3-921694-44-2

45 Barczewski, Baldur: *Neue Meßmethoden für Wasser-Luftgemische und deren Anwendung auf zweiphasige Auftriebsstrahlen*, 1979, ISBN 3-921694-45-0

46 Neumayer, Hans: *Untersuchung der Strömungsvorgänge in radialen Wirbelkammerverstärkern*, 1979, ISBN 3-921694-46-9

47 Elalfy, Youssef-Elhassan: *Untersuchung der Strömungsvorgänge in Wirbelkammerdioden und -drosseln*, 1979, ISBN 3-921694-47-7

48 Brombach, Hansjörg: *Automatisierung der Bewirtschaftung von Wasserspeichern*, 1981, ISBN 3-921694-48-5

49 Geldner, Peter: *Deterministische und stochastische Methoden zur Bestimmung der Selbstdichtung von Gewässern*, 1981, ISBN 3-921694-49-3, *vergriffen*

50 Mehlhorn, Hans: *Temperaturveränderungen im Grundwasser durch Brauchwassereinleitungen*, 1982, ISBN 3-921694-50-7, *vergriffen*

51 Hafner, Edzard: *Rohrleitungen und Behälter im Meer*, 1983, ISBN 3-921694-51-5

52 Rinnert, Bernd: *Hydrodynamische Dispersion in porösen Medien: Einfluß von Dichteunterschieden auf die Vertikalvermischung in horizontaler Strömung*, 1983, ISBN 3-921694-52-3, *vergriffen*

53 Lindner, Wulf: *Steuerung von Grundwasserentnahmen unter Einhaltung ökologischer Kriterien*, 1983, ISBN 3-921694-53-1, *vergriffen*

54 Herr, Michael; Herzer, Jörg; Kinzelbach, Wolfgang; Kobus, Helmut; Rinnert, Bernd: *Methoden zur rechnerischen Erfassung und hydraulischen Sanierung von Grundwasserkontaminationen*, 1983, ISBN 3-921694-54-X

55 Schmitt, Paul: *Wege zur Automatisierung der Niederschlagsermittlung*, 1984, ISBN 3-921694-55-8, *vergriffen*

56 Müller, Peter: *Transport und selektive Sedimentation von Schwebstoffen bei gestautem Abfluß*, 1985, ISBN 3-921694-56-6

57 El-Qawasmeh, Fuad: *Möglichkeiten und Grenzen der Tropfbewässerung unter besonderer Berücksichtigung der Verstopfungsanfälligkeit der Tropfelemente*, 1985, ISBN 3-921694-57-4, *vergriffen*

58 Kirchenbaur, Klaus: *Mikroprozessorgesteuerte Erfassung instationärer Druckfelder am Beispiel seegangsbelasteter Baukörper*, 1985, ISBN 3-921694-58-2

59 Kobus, Helmut (Hrsg.): *Modellierung des großräumigen Wärme- und Schadstofftransports im Grundwasser*, Tätigkeitsbericht 1984/85 (DFG-Forschergruppe an den Universitäten Hohenheim, Karlsruhe und Stuttgart), 1985, ISBN 3-921694-59-0, *vergriffen*

60 Spitz, Karlheinz: *Dispersion in porösen Medien: Einfluß von Inhomogenitäten und Dichteunterschieden*, 1985, ISBN 3-921694-60-4, *vergriffen*

61 Kobus, Helmut: *An Introduction to Air-Water Flows in Hydraulics*, 1985, ISBN 3-921694-61-2

62 Kaleris, Vassilios: *Erfassung des Austausches von Oberflächen- und Grundwasser in horizontalebenen Grundwassermodellen*, 1986, ISBN 3-921694-62-0

63 Herr, Michael: *Grundlagen der hydraulischen Sanierung verunreinigter Porengrundwasserleiter*, 1987, ISBN 3-921694-63-9

64 Marx, Walter: *Berechnung von Temperatur und Spannung in Massenbeton infolge Hydratation*, 1987, ISBN 3-921694-64-7

65 Koschitzky, Hans-Peter: *Dimensionierungskonzept für Sohlbelüfter in Schußrinnen zur Vermeidung von Kavitationsschäden*, 1987, ISBN 3-921694-65-5

66 Kobus, Helmut (Hrsg.): *Modellierung des großräumigen Wärme- und Schadstofftransports im Grundwasser*, Tätigkeitsbericht 1986/87 (DFG-Forschergruppe an den Universitäten Hohenheim, Karlsruhe und Stuttgart) 1987, ISBN 3-921694-66-3

67 Söll, Thomas: *Berechnungsverfahren zur Abschätzung anthropogener Temperaturanomalien im Grundwasser*, 1988, ISBN 3-921694-67-1

68 Dittrich, Andreas; Westrich, Bernd: *Bodenseeufererosion, Bestandsaufnahme und Bewertung*, 1988, ISBN 3-921694-68-X, *vergriffen*

69 Huwe, Bernd; van der Ploeg, Rienk R.: *Modelle zur Simulation des Stickstoffhaushaltes von Standorten mit unterschiedlicher landwirtschaftlicher Nutzung*, 1988, ISBN 3-921694-69-8, *vergriffen*

70 Stephan, Karl: *Integration elliptischer Funktionen*, 1988, ISBN 3-921694-70-1

71 Kobus, Helmut; Zilliox, Lothaire (Hrsg.): *Nitratbelastung des Grundwassers, Auswirkungen der Landwirtschaft auf die Grundwasser- und Rohwasserbeschaffenheit und Maßnahmen zum Schutz des Grundwassers*. Vorträge des deutsch-französischen Kolloquiums am 6. Oktober 1988, Universitäten Stuttgart und Louis Pasteur Strasbourg (Vorträge in deutsch oder französisch, Kurzfassungen zweisprachig), 1988, ISBN 3-921694-71-X

72 Soyeaux, Renald: *Unterströmung von Stauanlagen auf klüftigem Untergrund unter Berücksichtigung laminarer und turbulenter Fließzustände*,1991, ISBN 3-921694-72-8

73 Kohane, Roberto: *Berechnungsmethoden für Hochwasserabfluß in Fließgewässern mit überströmten Vorländern*, 1991, ISBN 3-921694-73-6

74 Hassinger, Reinhard: *Beitrag zur Hydraulik und Bemessung von Blocksteinrampen in flexibler Bauweise*, 1991, ISBN 3-921694-74-4, vergriffen

75 Schäfer, Gerhard: *Einfluß von Schichtenstrukturen und lokalen Einlagerungen auf die Längsdispersion in Porengrundwasserleitern*, 1991, ISBN 3-921694-75-2

76 Giesecke, Jürgen: *Vorträge, Wasserwirtschaft in stark besiedelten Regionen; Umweltforschung mit Schwerpunkt Wasserwirtschaft*, 1991, ISBN 3-921694-76-0

77 Huwe, Bernd: *Deterministische und stochastische Ansätze zur Modellierung des Stickstoffhaushalts landwirtschaftlich genutzter Flächen auf unterschiedlichem Skalenniveau*, 1992, ISBN 3-921694-77-9, vergriffen

78 Rommel, Michael: *Verwendung von Kluftdaten zur realitätsnahen Generierung von Kluftnetzen mit anschließender laminar-turbulenter Strömungsberechnung*, 1993, ISBN 3-92 1694-78-7

79 Marschall, Paul: *Die Ermittlung lokaler Stofffrachten im Grundwasser mit Hilfe von Einbohrloch-Meßverfahren*, 1993, ISBN 3-921694-79-5, vergriffen

80 Ptak, Thomas: *Stofftransport in heterogenen Porenaquiferen: Felduntersuchungen und stochastische Modellierung*, 1993, ISBN 3-921694-80-9, vergriffen

81 Haakh, Frieder: *Transientes Strömungsverhalten in Wirbelkammern,* 1993, ISBN 3-921694-81-7

82 Kobus, Helmut; Cirpka, Olaf; Barczewski, Baldur; Koschitzky, Hans-Peter: *Versuchseinrichtung zur Grundwasser- und Altlastensanierung VEGAS, Konzeption und Programmrahmen*, 1993, ISBN 3-921694-82-5

83 Zang, Weidong: *Optimaler Echtzeit-Betrieb eines Speichers mit aktueller Abflußregenerierung*, 1994, ISBN 3-921694-83-3, vergriffen

84 Franke, Hans-Jörg: *Stochastische Modellierung eines flächenhaften Stoffeintrages und Transports in Grundwasser am Beispiel der Pflanzenschutzmittelproblematik*, 1995, ISBN 3-921694-84-1

85 Lang, Ulrich: *Simulation regionaler Strömungs- und Transportvorgänge in Karstaquiferen mit Hilfe des Doppelkontinuum-Ansatzes: Methodenentwicklung und Parameteridentifikation*, 1995, ISBN 3-921694-85-X, vergriffen

86 Helmig, Rainer: *Einführung in die Numerischen Methoden der Hydromechanik*, 1996, ISBN 3-921694-86-8, vergriffen

87 Cirpka, Olaf: *CONTRACT: A Numerical Tool for Contaminant Transport and Chemical Transformations - Theory and Program Documentation -*, 1996, ISBN 3-921694-87-6

88 Haberlandt, Uwe: *Stochastische Synthese und Regionalisierung des Niederschlages für Schmutzfrachtberechnungen*, 1996, ISBN 3-921694-88-4

89 Croisé, Jean: *Extraktion von flüchtigen Chemikalien aus natürlichen Lockergesteinen mittels erzwungener Luftströmung*, 1996, ISBN 3-921694-89-2, vergriffen

90 Jorde, Klaus: *Ökologisch begründete, dynamische Mindestwasserregelungen bei Ausleitungskraftwerken*, 1997, ISBN 3-921694-90-6, vergriffen

91 Helmig, Rainer: *Gekoppelte Strömungs- und Transportprozesse im Untergrund - Ein Beitrag zur Hydrosystemmodellierung-*, 1998, ISBN 3-921694-91-4, vergriffen

92 Emmert, Martin: *Numerische Modellierung nichtisothermer Gas-Wasser Systeme in porösen Medien,* 1997, ISBN 3-921694-92-2

93 Kern, Ulrich: *Transport von Schweb- und Schadstoffen in staugeregelten Fließgewässern am Beispiel des Neckars*, 1997, ISBN 3-921694-93-0, vergriffen

94 Förster, Georg: *Druckstoßdämpfung durch große Luftblasen in Hochpunkten von Rohrleitungen 1997*, ISBN 3-921694-94-9

95 Cirpka, Olaf: *Numerische Methoden zur Simulation des reaktiven Mehrkomponententransports im Grundwasser*, 1997, ISBN 3-921694-95-7, *vergriffen*

96 Färber, Arne: *Wärmetransport in der ungesättigten Bodenzone: Entwicklung einer thermischen In-situ-Sanierungstechnologie*, 1997, ISBN 3-921694-96-5

97 Betz, Christoph: *Wasserdampfdestillation von Schadstoffen im porösen Medium: Entwicklung einer thermischen In-situ-Sanierungstechnologie*, 1998, SBN 3-921694-97-3

98 Xu, Yichun: *Numerical Modeling of Suspended Sediment Transport in Rivers*, 1998, ISBN 3-921694-98-1, *vergriffen*

99 Wüst, Wolfgang: *Geochemische Untersuchungen zur Sanierung CKW-kontaminierter Aquifere mit Fe(0)-Reaktionswänden,* 2000, ISBN 3-933761-02-2

100 Sheta, Hussam: *Simulation von Mehrphasenvorgängen in porösen Medien unter Einbeziehung von Hysterese-Effekten*, 2000, ISBN 3-933761-03-4

101 Ayros, Edwin: *Regionalisierung extremer Abflüsse auf der Grundlage statistischer Verfahren*, 2000, ISBN 3-933761-04-2, *vergriffen*

102 Huber, Ralf: *Compositional Multiphase Flow and Transport in Heterogeneous Porous Media*, 2000, ISBN 3-933761-05-0

103 Braun, Christopherus: *Ein Upscaling-Verfahren für Mehrphasenströmungen in porösen Medien*, 2000, ISBN 3-933761-06-9

104 Hofmann, Bernd: *Entwicklung eines rechnergestützten Managementsystems zur Beurteilung von Grundwasserschadensfällen*, 2000, ISBN 3-933761-07-7

105 Class, Holger: *Theorie und numerische Modellierung nichtisothermer Mehrphasenprozesse in NAPL-kontaminierten porösen Medien,* 2001, ISBN 3-933761-08-5

106 Schmidt, Reinhard: *Wasserdampf- und Heißluftinjektion zur thermischen Sanierung kontaminierter Standorte*, 2001, ISBN 3-933761-09-3

107 Josef, Reinhold: *Schadstoffextraktion mit hydraulischen Sanierungsverfahren unter Anwendung von grenzflächenaktiven Stoffen*, 2001, ISBN 3-933761-10-7

108 Schneider, Matthias: *Habitat- und Abflussmodellierung für Fließgewässer mit unscharfen Berechnungsansätzen*, 2001, ISBN 3-933761-11-5

109 Rathgeb, Andreas: *Hydrodynamische Bemessungsgrundlagen für Lockerdeckwerke an überströmbaren Erddämmen*, 2001, ISBN 3-933761-12-3

110 Lang, Stefan: *Parallele numerische Simulation instätionärer Probleme mit adaptiven Methoden auf unstrukturierten Gittern*, 2001, ISBN 3-933761-13-1

111 Appt, Jochen; Stumpp Simone: *Die Bodensee-Messkampagne 2001, IWS/CWR Lake Constance Measurement Program 2001*, 2002, ISBN 3-933761-14-X

112 Heimerl, Stephan: *Systematische Beurteilung von Wasserkraftprojekten,* 2002, ISBN 3-933761-15-8, *vergriffen*

113 Iqbal, Amin: *On the Management and Salinity Control of Drip Irrigation,* 2002, ISBN 3-933761-16-6

114 Silberhorn-Hemminger, Annette: *Modellierung von Kluftaquifersystemen: Geostatistische Analyse und deterministisch-stochastische Kluftgenerierung,* 2002, ISBN 3-933761-17-4

115 Winkler, Angela: *Prozesse des Wärme- und Stofftransports bei der In-situ-Sanierung mit festen Wärmequellen,* 2003, ISBN 3-933761-18-2

116 Marx, Walter: *Wasserkraft, Bewässerung, Umwelt - Planungs- und Bewertungsschwerpunkte der Wasserbewirtschaftung,* 2003, ISBN 3-933761-19-0

117 Hinkelmann, Reinhard: *Efficient Numerical Methods and Information-Processing Techniques in Environment Water,* 2003, ISBN 3-933761-20-4

118 Samaniego-Eguiguren, Luis Eduardo: *Hydrological Consequences of Land Use / Land Cover and Climatic Changes in Mesoscale Catchments*, 2003, ISBN 3-933761-21-2

119 Neunhäuserer, Lina: *Diskretisierungsansätze zur Modellierung von Strömungs- und Transportprozessen in geklüftet-porösen Medien*, 2003, ISBN 3-933761-22-0

120 Paul, Maren: *Simulation of Two-Phase Flow in Heterogeneous Poros Media with Adaptive Methods*, 2003, ISBN 3-933761-23-9

121 Ehret, Uwe: *Rainfall and Flood Nowcasting in Small Catchments using Weather Radar*, 2003, ISBN 3-933761-24-7

122 Haag, Ingo: *Der Sauerstoffhaushalt staugeregelter Flüsse am Beispiel des Neckars - Analysen, Experimente, Simulationen -,* 2003, ISBN 3-933761-25-5

123 Appt, Jochen: *Analysis of Basin-Scale Internal Waves in Upper Lake Constance,* 2003, ISBN 3-933761-26-3

124 Hrsg.: Schrenk, Volker; Batereau, Katrin; Barczewski, Baldur; Weber, Karolin und Koschitzky, Hans-Peter: *Symposium Ressource Fläche und VEGAS - Statuskolloquium 2003, 30. September und 1. Oktober 2003,* 2003, ISBN 3-933761-27-1

125 Omar Khalil Ouda: *Optimisation of Agricultural Water Use: A Decision Support System for the Gaza Strip,* 2003, ISBN 3-933761-28-0

126 Batereau, Katrin: *Sensorbasierte Bodenluftmessung zur Vor-Ort-Erkundung von Schadensherden im Untergrund*, 2004, ISBN 3-933761-29-8

127 Witt, Oliver: *Erosionsstabilität von Gewässersedimenten mit Auswirkung auf den Stofftransport bei Hochwasser am Beispiel ausgewählter Stauhaltungen des Oberrheins*, 2004, ISBN 3-933761-30-1

128 Jakobs, Hartmut: *Simulation nicht-isothermer Gas-Wasser-Prozesse in komplexen Kluft-Matrix-Systemen*, 2004, ISBN 3-933761-31-X

129 Li, Chen-Chien: *Deterministisch-stochastisches Berechnungskonzept zur Beurteilung der Auswirkungen erosiver Hochwasserereignisse in Flussstauhaltungen,* 2004, ISBN 3-933761-32-8

130 Reichenberger, Volker; Helmig, Rainer; Jakobs, Hartmut; Bastian, Peter; Niessner, Jennifer: *Complex Gas-Water Processes in Discrete Fracture-Matrix Systems: Up-scaling, Mass-Conservative Discretization and Efficient Multilevel Solution,* 2004, ISBN 3-933761-33-6

131 Hrsg.: Barczewski, Baldur; Koschitzky, Hans-Peter; Weber, Karolin; Wege, Ralf: *VEGAS - Statuskolloquium 2004,* Tagungsband zur Veranstaltung am 05. Oktober 2004 an der Universität Stuttgart, Campus Stuttgart-Vaihingen, 2004, ISBN 3-933761-34-4

132 Asie, Kemal Jabir: *Finite Volume Models for Multiphase Multicomponent Flow through Porous Media*. 2005, ISBN 3-933761-35-2

133 Jacoub, George: *Development of a 2-D Numerical Module for Particulate Contaminant Transport in Flood Retention Reservoirs and Impounded Rivers,* 2004, ISBN 3-933761-36-0

134 Nowak, Wolfgang: *Geostatistical Methods for the Identification of Flow and Transport Parameters in the Subsurface,* 2005, ISBN 3-933761-37-9

135 Süß, Mia: *Analysis of the influence of structures and boundaries on flow and transport processes in fractured porous media*, 2005, ISBN 3-933761-38-7

136 Jose, Surabhin Chackiath: *Experimental Investigations on Longitudinal Dispersive Mixing in Heterogeneous Aquifers,* 2005, ISBN: 3-933761-39-5

137 Filiz, Fulya: *Linking Large-Scale Meteorological Conditions to Floods in Mesoscale Catchments,* 2005, ISBN 3-933761-40-9

138 Qin, Minghao: *Wirklichkeitsnahe und recheneffiziente Ermittlung von Temperatur und Spannungen bei großen RCC-Staumauern*, 2005, ISBN 3-933761-41-7

139 Kobayashi, Kenichiro: *Optimization Methods for Multiphase Systems in the Subsurface - Application to Methane Migration in Coal Mining Areas*, 2005, ISBN 3-933761-42-5

140 Rahman, Md. Arifur: *Experimental Investigations on Transverse Dispersive Mixing in Heterogeneous Porous Media,* 2005, ISBN 3-933761-43-3

141 Schrenk, Volker: *Ökobilanzen zur Bewertung von Altlastensanierungsmaßnahmen,* 2005, ISBN 3-933761-44-1

142 Hundecha, Hirpa Yeshewatesfa: *Regionalization of Parameters of a Conceptual Rainfall-Runoff Model*, 2005, ISBN: 3-933761-45-X

143 Wege, Ralf: *Untersuchungs- und Überwachungsmethoden für die Beurteilung natürlicher Selbstreinigungsprozesse im Grundwasser,* 2005, ISBN 3-933761-46-8

144 Breiting, Thomas: *Techniken und Methoden der Hydroinformatik - Modellierung von komplexen Hydrosystemen im Untergrund*, 2006, ISBN 3-933761-47-6

145 Hrsg.: Braun, Jürgen; Koschitzky, Hans-Peter; Müller, Martin: *Ressource Untergrund: 10 Jahre VEGAS: Forschung und Technologieentwicklung zum Schutz von Grundwasser und Boden,* Tagungsband zur Veranstaltung am 28. und 29. September 2005 an der Universität Stuttgart, Campus Stuttgart-Vaihingen, 2005, ISBN 3-933761-48-4

146 Rojanschi, Vlad: *Abflusskonzentration in mesoskaligen Einzugsgebieten unter Berücksichtigung des Sickerraumes,* 2006, ISBN 3-933761-49-2

147 Winkler, Nina Simone: *Optimierung der Steuerung von Hochwasserrückhaltebeckensystemen,* 2006, ISBN 3-933761-50-6

148 Wolf, Jens: *Räumlich differenzierte Modellierung der Grundwasserströmung alluvialer Aquifere für mesoskalige Einzugsgebiete*, 2006, ISBN: 3-933761-51-4

149 Kohler, Beate: *Externe Effekte der Laufwasserkraftnutzung*, 2006, ISBN 3-933761-52-2

150 Hrsg.: Braun, Jürgen; Koschitzky, Hans-Peter; Stuhrmann, Matthias: *VEGAS-Statuskolloquium 2006,* Tagungsband zur Veranstaltung am 28. September 2006 an der Universität Stuttgart, Campus Stuttgart-Vaihingen, 2006, ISBN 3-933761-53-0

151 Niessner, Jennifer: *Multi-Scale Modeling of Multi-Phase - Multi-Component Processes in Heterogeneous Porous Media*, 2006, ISBN 3-933761-54-9

152 Fischer, Markus: *Beanspruchung eingeerdeter Rohrleitungen infolge Austrocknung bindiger Böden,* 2006, ISBN 3-933761-55-7

153 Schneck, Alexander: *Optimierung der Grundwasserbewirtschaftung unter Berücksichtigung der Belange der Wasserversorgung, der Landwirtschaft und des Naturschutzes*, 2006, ISBN 3-933761-56-5

154 Das, Tapash: *The Impact of Spatial Variability of Precipitation on the Predictive Uncertainty of Hydrological Models,* 2006, ISBN 3-33761-57-3

155 Bielinski, Andreas: *Numerical Simulation of CO_2 sequestration in geological formations*, 2007, ISBN 3-933761-58-1

156 Mödinger, Jens: *Entwicklung eines Bewertungs- und Entscheidungsunterstützungssystems für eine nachhaltige regionale Grundwasserbewirtschaftung*, 2006, ISBN 3-933761-60-3

157 Manthey, Sabine: *Two-phase flow processes with dynamic effects in porous media - parameter estimation and simulation,* 2007, ISBN 3-933761-61-1

158 Pozos Estrada, Oscar: *Investigation on the Effects of Entrained Air in Pipelines,* 2007, ISBN 3-933761-62-X

159 Ochs, Steffen Oliver: *Steam injection into saturated porous media – process analysis including experimental and numerical investigations*, 2007, ISBN 3-933761-63-8

160 Marx, Andreas: *Einsatz gekoppelter Modelle und Wetterradar zur Abschätzung von Niederschlagsintensitäten und zur Abflussvorhersage, 2007,* ISBN 3-933761-64-6

161 Hartmann, Gabriele Maria: *Investigation of Evapotranspiration Concepts in Hydrological Modelling for Climate Change Impact Assessment*, 2007, ISBN 3-933761-65-4

162 Kebede Gurmessa, Tesfaye: *Numerical Investigation on Flow and Transport Characteristics to Improve Long-Term Simulation of Reservoir Sedimentation*, 2007, ISBN 3-933761-66-2

163 Trifković, Aleksandar: *Multi-objective and Risk-based Modelling Methodology for Planning, Design and Operation of Water Supply Systems*, 2007, ISBN 3-933761-67-0

164 Götzinger, Jens: *Distributed Conceptual Hydrological Modelling - Simulation of Climate, Land Use Change Impact and Uncertainty Analysis*, 2007, ISBN 3-933761-68-9

165 Hrsg.: Braun, Jürgen; Koschitzky, Hans-Peter; Stuhrmann, Matthias: *VEGAS – Kolloquium 2007,* Tagungsband zur Veranstaltung am 26. September 2007 an der Universität Stuttgart, Campus Stuttgart-Vaihingen, 2007, ISBN 3-933761-69-7

166 Freeman, Beau: *Modernization Criteria Assessment for Water Resources Planning; Klamath Irrigation Project, U.S.*, 2008, ISBN 3-933761-70-0

167 Dreher, Thomas: *Selektive Sedimentation von Feinstschwebstoffen in Wechselwirkung mit wandnahen turbulenten Strömungsbedingungen*, 2008, ISBN 3-933761-71-9

168 Yang, Wei: *Discrete-Continuous Downscaling Model for Generating Daily Precipitation Time Series*, 2008, ISBN 3-933761-72-7

169 Kopecki, Ianina: *Calculational Approach to FST-Hemispheres for Multiparametrical Benthos Habitat Modelling,* 2008*,* ISBN 3-933761-73-5

170 Brommundt, Jürgen: *Stochastische Generierung räumlich zusammenhängender Niederschlagszeitreihen*, 2008, ISBN 3-933761-74-3

171 Papafotiou, *Alexandros: Numerical Investigations of the Role of Hysteresis in Heterogeneous Two-Phase Flow Systems*, 2008, ISBN 3-933761-75-1

172 He, Yi: *Application of a Non-Parametric Classification Scheme to Catchment Hydrology*, 2008, ISBN 978-3-933761-76-7

173 Wagner, Sven: *Water Balance in a Poorly Gauged Basin in West Africa Using Atmospheric Modelling and Remote Sensing Information*, 2008, ISBN 978-3-933761-77-4

174 Hrsg.: Braun, Jürgen; Koschitzky, Hans-Peter; Stuhrmann, Matthias; Schrenk, Volker: *VEGAS-Kolloquium 2008 Ressource Fläche III*, Tagungsband zur Veranstaltung am 01. Oktober 2008 an der Universität Stuttgart, Campus Stuttgart-Vaihingen, 2008, ISBN 978-3-933761-78-1

175 Patil, Sachin: *Regionalization of an Event Based Nash Cascade Model for Flood Predictions in Ungauged Basins*, 2008, ISBN 978-3-933761-79-8

176 Assteerawatt, Anongnart: *Flow and Transport Modelling of Fractured Aquifers based on a Geostatistical Approach,* 2008, ISBN 978-3-933761-80-4

177 Karnahl, Joachim Alexander: *2D numerische Modellierung von multifraktionalem Schwebstoff- und Schadstofftransport in Flüssen*, 2008, ISBN 978-3-933761-81-1

178 Hiester, Uwe: *Technologieentwicklung zur In-situ-Sanierung der ungesättigten Bodenzone mit festen Wärmequellen,* 2009, ISBN 978-3-933761-82-8

179 Laux, Patrick: *Statistical Modeling of Precipitation for Agricultural Planning in the Volta Basin of West Africa,* 2009, ISBN 978-3-933761-83-5

180 Ehsan, Saqib: *Evaluation of Life Safety Risks Related to Severe Flooding,* 2009, ISBN 978-3-933761-84-2

181 Prohaska, Sandra: *Development and Application of a 1D Multi-Strip Fine Sediment Transport Model for Regulated Rivers,* 2009, ISBN 978-3-933761-85-9

182 Kopp, Andreas: *Evaluation of CO_2 Injection Processes in Geological Formations for Site Screening,* 2009, ISBN 978-3-933761-86-6

183 Ebigbo, Anozie: *Modelling of biofilm growth and its influence on CO_2 and water (two-phase) flow in porous media,* 2009, ISBN 978-3-933761-87-3

184 Freiboth, Sandra: *A phenomenological model for the numerical simulation of multiphase multicomponent processes considering structural alterations of porous media*, 2009, ISBN 978-3-933761-88-0

185 Zöllner, Frank: *Implementierung und Anwendung netzfreier Methoden im Konstruktiven Wasserbau und in der Hydromechanik*, 2009, ISBN 978-3-933761-89-7

186 Vasin, Milos: *Influence of the soil structure and property contrast on flow and transport in the unsaturated zone*, 2010, ISBN 978-3-933761-90-3

187 Li, Jing: *Application of Copulas as a New Geostatistical Tool*, 2010, ISBN 978-3-933761-91-0

188 AghaKouchak, Amir: *Simulation of Remotely Sensed Rainfall Fields Using Copulas*, 2010, ISBN 978-3-933761-92-7

189 Thapa, Pawan Kumar: *Physically-based spatially distributed rainfall runoff modelling for soil erosion estimation*, 2010, ISBN 978-3-933761-93-4

190 Wurms, Sven: *Numerische Modellierung der Sedimentationsprozesse in Retentionsanlagen zur Steuerung von Stoffströmen bei extremen Hochwasserabflussereignissen*, 2011, ISBN 978-3-933761-94-1

191 Merkel, Uwe: *Unsicherheitsanalyse hydraulischer Einwirkungen auf Hochwasserschutzdeiche und Steigerung der Leistungsfähigkeit durch adaptive Strömungsmodellierung*, 2011, ISBN 978-3-933761-95-8

192 Fritz, Jochen: *A Decoupled Model for Compositional Non-Isothermal Multiphase Flow in Porous Media and Multiphysics Approaches for Two-Phase Flow*, 2010, ISBN 978-3-933761-96-5

193 Weber, Karolin (Hrsg.): *12. Treffen junger WissenschaftlerInnen an Wasserbauinstituten*, 2010, ISBN 978-3-933761-97-2

194 Bliefernicht, Jan-Geert: *Probability Forecasts of Daily Areal Precipitation for Small River Basins,* 2011, ISBN 978-3-933761-98-9

195 Hrsg.: Koschitzky, Hans-Peter; Braun, Jürgen: *VEGAS-Kolloquium 2010 In-situ-Sanierung - Stand und Entwicklung Nano und ISCO -,* Tagungsband zur Veranstaltung am 07. Oktober 2010 an der Universität Stuttgart, Campus Stuttgart-Vaihingen*,* 2010*,* ISBN 978-3-933761-99-6

196 Gafurov, Abror: *Water Balance Modeling Using Remote Sensing Information - Focus on Central Asia,* 2010, ISBN 978-3-942036-00-9

197 Mackenberg, Sylvia: *Die Quellstärke in der Sickerwasserprognose: Möglichkeiten und Grenzen von Labor- und Freilanduntersuchungen,* 2010, ISBN 978-3-942036-01-6

198 Singh, Shailesh Kumar: *Robust Parameter Estimation in Gauged and Ungauged Basins,* 2010, ISBN 978-3-942036-02-3

199 Doğan, Mehmet Onur: *Coupling of porous media flow with pipe flow,* 2011, ISBN 978-3-942036-03-0

200 Liu, Min: *Study of Topographic Effects on Hydrological Patterns and the Implication on Hydrological Modeling and Data Interpolation,* 2011, ISBN 978-3-942036-04-7

201 Geleta, Habtamu Itefa: *Watershed Sediment Yield Modeling for Data Scarce Areas,* 2011, ISBN 978-3-942036-05-4

202 Franke, Jörg: *Einfluss der Überwachung auf die Versagenswahrscheinlichkeit von Staustufen,* 2011, ISBN 978-3-942036-06-1

203 Bakimchandra, Oinam: *Integrated Fuzzy-GIS approach for assessing regional soil erosion risks,* 2011, ISBN 978-3-942036-07-8

204 Alam, Muhammad Mahboob: *Statistical Downscaling of Extremes of Precipitation in Mesoscale Catchments from Different RCMs and Their Effects on Local Hydrology,* 2011, ISBN 978-3-942036-08-5

205 Hrsg.: Koschitzky, Hans-Peter; Braun, Jürgen: *VEGAS-Kolloquium 2011 Flache Geothermie - Perspektiven und Risiken,* Tagungsband zur Veranstaltung am 06. Oktober 2011 an der Universität Stuttgart, Campus Stuttgart-Vaihingen*,* 2011*,* ISBN 978-3-933761-09-2

206 Haslauer, Claus: *Analysis of Real-World Spatial Dependence of Subsurface Hydraulic Properties Using Copulas with a Focus on Solute Transport Behaviour,* 2011, ISBN 978-3-942036-10-8

207 Dung, Nguyen Viet: *Multi-objective automatic calibration of hydrodynamic models – development of the concept and an application in the Mekong Delta,* 2011, ISBN 978-3-942036-11-5

208 Hung, Nguyen Nghia: *Sediment dynamics in the floodplain of the Mekong Delta, Vietnam,* 2011, ISBN 978-3-942036-12-2

209 Kuhlmann, Anna: *Influence of soil structure and root water uptake on flow in the unsaturated zone,* 2012, ISBN 978-3-942036-13-9

210 Tuhtan, Jeffrey Andrew: *Including the Second Law Inequality in Aquatic Ecodynamics: A Modeling Approach for Alpine Rivers Impacted by Hydropeaking,* 2012, ISBN 978-3-942036-14-6

211 Tolossa, Habtamu: *Sediment Transport Computation Using a Data-Driven Adaptive Neuro-Fuzzy Modelling Approach,* 2012, ISBN 978-3-942036-15-3

212 Tatomir, Alexandru-Bodgan: *From Discrete to Continuum Concepts of Flow in Fractured Porous Media,* 2012, ISBN 978-3-942036-16-0

213 Erbertseder, Karin: *A Multi-Scale Model for Describing Cancer-Therapeutic Transport in the Human Lung,* 2012, ISBN 978-3-942036-17-7

214 Noack, Markus: *Modelling Approach for Interstitial Sediment Dynamics and Reproduction of Gravel Spawning Fish,* 2012, ISBN 978-3-942036-18-4

215 De Boer, Cjestmir Volkert: *Transport of Nano Sized Zero Valent Iron Colloids during Injection into the Subsurface*, 2012, ISBN 978-3-942036-19-1

216 Pfaff, Thomas: *Processing and Analysis of Weather Radar Data for Use in Hydrology*, 2013, ISBN 978-3-942036-20-7

217 Lebrenz, Hans-Henning: *Addressing the Input Uncertainty for Hydrological Modeling by a New Geostatistical Method*, 2013, ISBN 978-3-942036-21-4

218 Darcis, Melanie Yvonne: *Coupling Models of Different Complexity for the Simulation of CO_2 Storage in Deep Saline Aquifers*, 2013, ISBN 978-3-942036-22-1

219 Beck, Ferdinand: *Generation of Spatially Correlated Synthetic Rainfall Time Series in High Temporal Resolution - A Data Driven Approach*, 2013, ISBN 978-3-942036-23-8

220 Guthke, Philipp: *Non-multi-Gaussian spatial structures: Process-driven natural genesis, manifestation, modeling approaches, and influences on dependent processes*, 2013, ISBN 978-3-942036-24-5

221 Walter, Lena: *Uncertainty studies and risk assessment for CO_2 storage in geological formations*, 2013, ISBN 978-3-942036-25-2

222 Wolff, Markus: *Multi-scale modeling of two-phase flow in porous media including capillary pressure effects,* 2013, ISBN 978-3-942036-26-9

223 Mosthaf, Klaus Roland: *Modeling and analysis of coupled porous-medium and free flow with application to evaporation processes,* 2014, ISBN 978-3-942036-27-6

224 Leube, Philipp Christoph: *Methods for Physically-Based Model Reduction in Time: Analysis, Comparison of Methods and Application*, 2013, ISBN 978-3-942036-28-3

225 Rodríguez Fernández, Jhan Ignacio: *High Order Interactions among environmental variables: Diagnostics and initial steps towards modeling*, 2013, ISBN 978-3-942036-29-0

226 Eder, Maria Magdalena: *Climate Sensitivity of a Large Lake*, 2013, ISBN 978-3-942036-30-6

227 Greiner, Philipp: *Alkoholinjektion zur In-situ-Sanierung von CKW Schadensherden in Grundwasserleitern: Charakterisierung der relevanten Prozesse auf unterschiedlichen Skalen*, 2014, ISBN 978-3-942036-31-3

228 Lauser, Andreas: *Theory and Numerical Applications of Compositional Multi-Phase Flow in Porous Media*, 2014, ISBN 978-3-942036-32-0

229 Enzenhöfer, Rainer: *Risk Quantification and Management in Water Production and Supply Systems*, 2014, ISBN 978-3-942036-33-7

230 Faigle, Benjamin: *Adaptive modelling of compositional multi-phase flow with capillary pressure*, 2014, ISBN 978-3-942036-34-4

231 Oladyshkin, Sergey: *Efficient modeling of environmental systems in the face of complexity and uncertainty*, 2014, ISBN 978-3-942036-35-1

232 Sugimoto, Takayuki: *Copula based Stochastic Analysis of Discharge Time Series*, 2014, ISBN 978-3-942036-36-8

233 Koch, Jonas: *Simulation, Identification and Characterization of Contaminant Source Architectures in the Subsurface*, 2014, ISBN 978-3-942036-37-5

234 Zhang, Jin: *Investigations on Urban River Regulation and Ecological Rehabilitation Measures, Case of Shenzhen in China*, 2014, ISBN 978-3-942036-38-2

235 Siebel, Rüdiger: *Experimentelle Untersuchungen zur hydrodynamischen Belastung und Standsicherheit von Deckwerken an überströmbaren Erddämmen,* 2014, ISBN 978-3-942036-39-9

236 Baber, Katherina: *Coupling free flow and flow in porous media in biological and technical applications: From a simple to a complex interface description,* 2014, ISBN 978-3-942036-40-5

237 Nuske, Klaus Philipp: *Beyond Local Equilibrium — Relaxing local equilibrium assumptions in multiphase flow in porous media,* 2014, ISBN 978-3-942036-41-2

238 Geiges, Andreas: *Efficient concepts for optimal experimental design in nonlinear environmental systems*, 2014, ISBN 978-3-942036-42-9

239 Schwenck, Nicolas: *An XFEM-Based Model for Fluid Flow in Fractured Porous Media*, 2014, ISBN 978-3-942036-43-6

240 Chamorro Chávez, Alejandro: *Stochastic and hydrological modelling for climate change prediction in the Lima region, Peru*, 2015, ISBN 978-3-942036-44-3

241 Yulizar: *Investigation of Changes in Hydro-Meteorological Time Series Using a Depth-Based Approach*, 2015, ISBN 978-3-942036-45-0

242 Kretschmer, Nicole: *Impacts of the existing water allocation scheme on the Limarí watershed – Chile, an integrative approach*, 2015, ISBN 978-3-942036-46-7

243 Kramer, Matthias: *Luftbedarf von Freistrahlturbinen im Gegendruckbetrieb*, 2015, ISBN 978-3-942036-47-4

244 Hommel, Johannes: *Modeling biogeochemical and mass transport processes in the subsurface: Investigation of microbially induced calcite precipitation*, 2016, ISBN 978-3-942036-48-1

245 Germer, Kai: *Wasserinfiltration in die ungesättigte Zone eines makroporösen Hanges und deren Einfluss auf die Hangstabilität*, 2016, ISBN 978-3-942036-49-8

246 Hörning, Sebastian: *Process-oriented modeling of spatial random fields using copulas*, 2016, ISBN 978-3-942036-50-4

247 Jambhekar, Vishal: *Numerical modeling and analysis of evaporative salinization in a coupled free-flow porous-media system,* 2016, ISBN 978-3-942036-51-1

248 Huang, Yingchun: *Study on the spatial and temporal transferability of conceptual hydrological models*, 2016, ISBN 978-3-942036-52-8

249 Kleinknecht, Simon Matthias: *Migration and retention of a heavy NAPL vapor and remediation of the unsaturated zone*, 2016, ISBN 978-3-942036-53-5

250 Kwakye, Stephen Oppong: *Study on the effects of climate change on the hydrology of the West African sub-region*, 2016, ISBN 978-3-942036-54-2

251 Kissinger, Alexander: *Basin-Scale Site Screening and Investigation of Possible Impacts of CO_2 Storage on Subsurface Hydrosystems*, 2016, ISBN 978-3-942036-55-9

252 Müller, Thomas: *Generation of a Realistic Temporal Structure of Synthetic Precipitation Time Series for Sewer Applications*, 2017, ISBN 978-3-942036-56-6

253 Grüninger, Christoph: *Numerical Coupling of Navier-Stokes and Darcy Flow for Soil-Water Evaporation*, 2017, ISBN 978-3-942036-57-3

254 Suroso: *Asymmetric Dependence Based Spatial Copula Models: Empirical Investigations and Consequences on Precipitation Fields*, 2017, ISBN 978-3-942036-58-0

255 Müller, Thomas; Mosthaf, Tobias; Gunzenhauser, Sarah; Seidel, Jochen; Bárdossy, András: *Grundlagenbericht Niederschlags-Simulator (NiedSim3)*, 2017, ISBN 978-3-942036-59-7

256 Mosthaf, Tobias: *New Concepts for Regionalizing Temporal Distributions of Precipitation and for its Application in Spatial Rainfall Simulation,* 2017, ISBN 978-3-942036-60-3

257 Fenrich, Eva Katrin: *Entwicklung eines ökologisch-ökonomischen Vernetzungsmodells für Wasserkraftanlagen und Mehrzweckspeicher,* 2018, ISBN 978-3-942036-61-0

258 Schmidt, Holger: *Microbial stabilization of lotic fine sediments*, 2018, ISBN 978-3-942036-62-7

259 Fetzer, Thomas: *Coupled Free and Porous-Medium Flow Processes Affected by Turbulence and Roughness – Models, Concepts and Analysis*, 2018, ISBN 978-3-942036-63-4

260 Schröder, Hans Christoph: *Large-scale High Head Pico Hydropower Potential Assessment*, 2018, ISBN 978-3-942036-64-1

261 Bode, Felix: *Early-Warning Monitoring Systems for Improved Drinking Water Resource Protection*, 2018, ISBN 978-3-942036-65-8

262 Gebler, Tobias: *Statistische Auswertung von simulierten Talsperrenüberwachungsdaten zur Identifikation von Schadensprozessen an Gewichtsstaumauern*, 2018, ISBN 978-3-942036-66-5

263 Harten, Matthias von: *Analyse des Zuppinger-Wasserrades – Hydraulische Optimierungen unter Berücksichtigung ökologischer Aspekte*, 2018, ISBN 978-3-942036-67-2

264 Yan, Jieru: *Nonlinear estimation of short time precipitation using weather radar and surface observations*, 2018, ISBN 978-3-942036-68-9

265 Beck, Martin: *Conceptual approaches for the analysis of coupled hydraulic and geomechanical processes*, 2019, ISBN 978-3-942036-69-6

266 Haas, Jannik: *Optimal planning of hydropower and energy storage technologies for fully renewable power systems*, 2019, ISBN 978-3-942036-70-2

267 Schneider, Martin: *Nonlinear Finite Volume Schemes for Complex Flow Processes and Challenging Grids*, 2019, ISBN 978-3-942036-71-9

268 Most, Sebastian Christopher: *Analysis and Simulation of Anomalous Transport in Porous Media*, 2019, ISBN 978-3-942036-72-6

269 Buchta, Rocco: *Entwicklung eines Ziel- und Bewertungssystems zur Schaffung nachhaltiger naturnaher Strukturen in großen sandgeprägten Flüssen des norddeutschen Tieflandes*, 2019, ISBN 978-3-942036-73-3

270 Thom, Moritz: *Towards a Better Understanding of the Biostabilization Mechanisms of Sediment Beds*, 2019, ISBN 978-3-942036-74-0

271 Stolz, Daniel: *Die Nullspannungstemperatur in Gewichtsstaumauern unter Berücksichtigung der Festigkeitsentwicklung des Betons*, 2019, ISBN 978-3-942036-75-7

272 Rodriguez Pretelin, Abelardo: *Integrating transient flow conditions into groundwater well protection*, 2020, ISBN: 978-3-942036-76-4

273 Weishaupt, Kilian: *Model Concepts for Coupling Free Flow with Porous Medium Flow at the Pore-Network Scale: From Single-Phase Flow to Compositional Non-Isothermal Two-Phase Flow*, 2020, ISBN: 978-3-942036-77-1

274 Koch, Timo: *Mixed-dimension models for flow and transport processes in porous media with embedded tubular network systems*, 2020, ISBN: 978-3-942036-78-8

275 Gläser, Dennis: *Discrete fracture modeling of multi-phase flow and deformation in fractured poroelastic media*, 2020, ISBN: 978-3-942036-79-5

276 Seitz, Lydia: *Development of new methods to apply a multi-parameter approach – A first step towards the determination of colmation*, 2020, ISBN: 978-3-942036-80-1

277 Ebrahim Bakhshipour, Amin: *Optimizing hybrid decentralized systems for sustainable urban drainage infrastructures planning*, 2021, ISBN: 978-3-942036-81-8

278 Seitz, Gabriele: *Modeling Fixed-Bed Reactors for Thermochemical Heat Storage with the Reaction System $CaO/Ca(OH)_2$*, 2021, ISBN: 978-3-942036-82-5

279 Emmert, Simon: *Developing and Calibrating a Numerical Model for Microbially Enhanced Coal-Bed Methane Production*, 2021, ISBN: 978-3-942036-83-2

280 Heck, Katharina Klara: *Modelling and analysis of multicomponent transport at the interface between free- and porous-medium flow - influenced by radiation and roughness*, 2021, ISBN: 978-3-942036-84-9

281 Ackermann, Sina: *A multi-scale approach for drop/porous-medium interaction*, 2021, ISBN: 978-3-942036-85-6

282 Beckers, Felix: *Investigations on Functional Relationships between Cohesive Sediment Erosion and Sediment Characteristics*, 2021, ISBN: 978-3-942036-86-3

283 Schlabing, Dirk: *Generating Weather for Climate Impact Assessment on Lakes*, 2021, ISBN: 978-3-942036-87-0

284 Becker, Beatrix: *Efficient multiscale multiphysics models accounting for reversible flow at various subsurface energy storage sites*, 2021, ISBN: 978-3-942036-88-7

Die Mitteilungshefte ab der Nr. 134 (Jg. 2005) stehen als pdf-Datei über die Homepage des Instituts: www.iws.uni-stuttgart.de zur Verfügung.